Study of Jet Quenching Using γ-jet Events in Heavy Ion Collisions at 2.76TeV

by

Yongsun Kim

B.S. Physics
University of Illinois at Urbana Champaign, 2007

Submitted to the Department of Physics
in partial fulfillment of the requirements for the degree of

Doctor of Philosophy

at the

MASSACHUSETTS INSTITUTE OF TECHNOLOGY

April 2013

Author . . . . . .
Department of Physics
April 30th, 2013

Certified by . . . . . .
Wit Busza
Francis Friedman Professor of Physics
Thesis Supervisor

Accepted by . . . . . .
Prof. Dr. John Belcher
Associate Department Head

Study of Jet Quenching Using γ-jet Events in Heavy Ion Collisions at 2.76TeV

by

Yongsun Kim

Submitted to the Department of Physics
on April 30th, 2013, in partial fulfillment of the
requirements for the degree of
Doctor of Philosophy

Abstract

The kinematic correlations of isolated-γ+jet scatterings in proton-proton and lead-lead collisions at centre-of-mass energy of 2.76TeV per nucleon pair are studied for the investigation of the jet quenching phenomena in hot and dense QCD medium. The analysis uses collision data delivered by the LHC and recorded by CMS detector at CERN. The angular correlation, the transverse momentum ratio and the rate of mono-photon events are measured and their dependence on the collisional impact parameter is examined in lead-lead collision. The results of proton-proton collisions are used as the reference to which the lead-lead results are compared. Significant energy loss of jets induced by the hot and dense medium, and its gradual rise in correlation to the size of the medium are observed in lead-lead collisions, while a modification of the direction of jet axis is not detected.

Thesis Supervisor: Wit Busza

Title: Francis Friedman Professor of Physics

This dissertation is dedicated to my beloved parents, Kapseok Kim and Sungim Kim.

Contents

Glossary

η Pseudo-rapidity, defined as $-\ln(\tan(\frac{\theta}{2}))$. 28

γ Greek Symbol of photon. 36

ϕ Azimuthal angle in the cylindrical coordinate of the reference fame of detector.. 28

θ Polar angle in the cylindrical coordinate of the reference fame of detector.. 31

$\mathbf{E_T}$ Transverse energy. A photon's E_T is same to its $p_T$because it is massless. 37

$\mathbf{N_{coll}}$ Number of binary sub-collisions (nucleon+nucleon) in a nucleus+nucleus event. (Sec. 5.1.1). 72

$\mathbf{N_{part}}$ Number of constituent nucleons in colliding nuclei, which participate in nucleon+nucleon sub-collisions. (Sec. 5.1.1). 72

$\mathbf{k}_\perp$ Transverse momentum defined when a particle radiates another one. For example, when a quark radiates a gluon, k_T of the gluon is the transverse momentum perpendicularly measured from the quark's momentum vector. 30

p_T Momentum projected on the transverse plane.. 27

BSC Acronym of Beam Scintillator Counters. One of sub-detectors of CMS. Used for event selection.. 52

CMS Acronym of Compact Muon Solenoid. One of particle detectors of LHC experiment. Also the name of the collaboration of this detector. 17, 47

gluons See Sec. 2.1.1. 15

HF Acronym of Hadronic Forward Calorimeter. One of sub-detectors of CMS. Used for event selection and centrality determination.. 52

HLT Acronym of the High Level Trigger.. 52, 54, 56, 74

HYDJET MC simulation software developed to produce high energy heavy ion collsions. It was used to simulate the hadronic (inelastic) collisions at various impact parameters. More detailes are described in Sec. 4.3. 61, 68, 91, 123, 124, 126, 129

LHC Acronym of the Large Hadron Collider. The world largest and highest energy particle accelerator.. 17, 22, 23, 47, 48

MC Acronym of Monte Carlo (simulation). 45, 46, 73, 78, 80, 88, 94, 123, 124, 127, 144

nucleons protons and neutrons. Particularly in this thesis, nucleons usually refer the constituents of nucleus.. 15

partons Sub-atomic particles that compose nucleons. In this thesis, it means quarks and gluons.. 16

PbPb Collision of two fully stripped lead ions (^{208}Pb).. 36, 38, 39, 57, 74, 91, 123, 130, 132

pp Collision of two protons. 36, 57, 91, 123

PYTHIA MC simulation software developed to produce hard scatterings, for example the $\gamma-$jetchannels. More detailes are described in Sec. 4.1. 61, 66, 68, 91, 123, 124, 126, 129

QCD Acronym of the Quantum Chromodynamics.. 15, 17, 18, 20, 22, 28, 30, 34, 36

QGP Acronym of the Quark Gluon Plasma.. 15, 16, 18, 23, 30, 123, 144

quarks See Sec. 2.1.1. 15

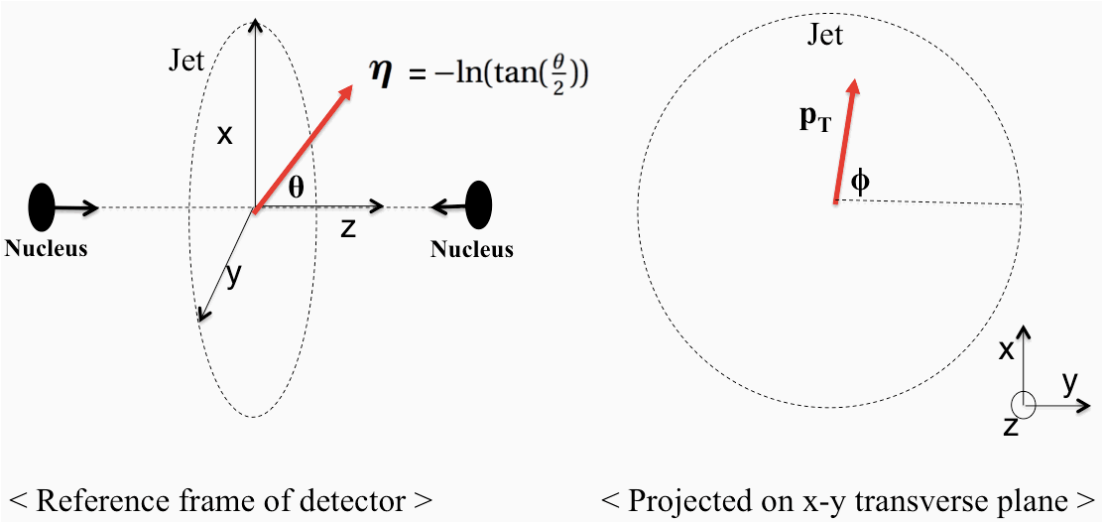

Figure 0.1: Kinematic variables in the laboratory reference frame (Left) and in the transverse plane (Right).

1 Introduction

1.1 Overview of this thesis

The motivation of this thesis is curiosity about the **Strong Nuclear Force**. It is one of the fundamental interactions in nature with the others being the gravity, the electromagnetic force and the weak nuclear force. The magnitude of the strong force is much bigger than the others by far as its name indicates. However, it took long time to be identified by physicists, because it exerts only when particles are at very close distance about 10^{-15}m, which is the typical size of a nucleus. Due to the dilute environment of matter, it is not easy to discern the strong force dynamics in our daily life. It is encapsulated inside nucleons and does not easily reveal to outside unless the nucleons are broken. For this reason, the exploration of strong force has been in close relationship with the development of particle accelerators. When two particles, i.e. protons, collide at near-light speed, high energy is released and immediately converted into production of particles. These high energy environment made by colliding experiments give the strong interaction a chance to be exhibited in a laboratory.

Quantum Chromodynamics, or **QCD**, is widely accepted theory as it successfully describes the strong force phenomena discovered so far. One example is the **confinement** feature. Nucleons are composed of smaller constituents called **quarks**. They attract each other by exchanging **gluons**. This is analogous to that charged particles electromagnetically interact by exchanging photons. However, one critical feature of the strong interaction different from electromagnetic interaction is that the force fastening quarks gets stronger as they are farther from each other. It needs infinite amount of energy to completely take these apart. Consequently, quarks and gluons are confined in the volume of a nucleon and this explains why the nucleons are not spontaneously divided into isolated quarks.

A very interesting prediction of QCD is the existence of **Quark Gluon Plasma**, or QGP [1]. This is a new phase of matter under extremely high temperature - about $1,000,000,000,000^{\circ}$C. In this regime, the coupling among quarks and gluons becomes

smaller and liberates partons out of the volume of nucleon, which is called **deconfinement**. It is widely believed that the structure of the universe about 10 micro seconds after the Big Bang was the QGP. Hence, study of this extraordinary phenomenon is essential to understand the formation of the early universe and the history of particle production.

High Energy Heavy Ion Experiment was initiated to study the QGP in laboratories without travelling to the past when Big Bang happened. By colliding two high speed nuclei, one can heat space around collision point to high temperature enough to make QGP. It is Initially in a cylindrical shape with radius of ∼5 femtometers, then it begins to cool down as well as it expands. About 20 fm/c ($\sim 7 \times 10^{-23}$ seconds) later - in each particle's frame - the medium decays into thousands of stable particles such as pions, kaons and protons. Since the hot matter is too small and transient, the final state of stable particles, which is actually perceived by detectors, are used to backcast the history of underlying phenomena.

In 1980s and 1990s the SPS at CERN in Geneva [2] and AGS at Brookhaven National Lab [3] carried out heavy ion experiments using lead and gold nuclei. Later, these are followed by the RHIC program - PHOBOS [4], PHENIX [5], STAR [6] and BRAHMS [7] - at BNL. Since June 2000, RHIC has done collision experiment with various heavy ions, mostly gold nuclei, at the center of mass energy up to 200 GeV per nucleon pairs since 2000. For the last decade, those experiments found various thermodynamic properties of hot and dense medium.

The discoveries at RHIC were accomplished primarily via direct measurement of particle multiplicities and spectra. On the other hand, there is an indirect method to study a state of matter. One can shoot a high momentum particle and probe the modification of it after passing though the medium. An excellent example is the Rutherford scattering [8, 9] by which Ernest Rutherford revealed the structure of gold nucleus by shooting alpha particles. More recently, the Deep Inelastic Scattering used electron as probe to explore the constitution of proton [10]. Similarly, we may use a highly energetic quark as a probe to examine the QGP. But we can not produce an external isolated quark source due to confinement. This obstacle can be resolved by creating the probe internally at the initial state of nuclei collision.

If the collision energy is high enough, hard scatterings of partons can happen occasionally and induce the production of high energy quark in the middle of hot medium. It has been expected that the quark would lose significant amount of energy by strong interaction as it traverses though the medium([11–13] and Bjorken's unpublished note).

This phenomenon is called **Jet Quenching** and its study is the major theme of this thesis.

In particular, we will focus on the quarks produced in **photon-jet**, or $\gamma-$jet , channels in which a quark is recoiled by photon so the pair is scattered in back-to-back nature. These quark decay into a bunch of collinear hadrons which is called **Jet**. This channel has great advantage compared to other hard scatterings in that the photon does not exert strong force so it can escape the medium without any interaction. Thus, the information of quark before jet quenching can be inferred from the photon, and that after quenching from the jet. Hence, we can directly compare status of the quark before and after jet quenching by correlating the photon and jet.

There have been trials to observe photon-jet evens in the past experiment - at RHIC. The collision energy, however, was not high enough and it was technically hard to find jets to tag individual quarks. Instead, the correlation between photon and high momentum particles was studied with a reasonable assumption that the most high momentum hadrons are made by jets [14]. The result indirectly indicated evidences of jet quenching, but it could not clearly quantify the energy loss of individual partons.

Efficient identification of jets in photon-jet channels in heavy ion experiments became possible in the LHC era where the collision energy was increased by 14 times. This lucky situation enabled me to write this dissertation on this topic. The experiment was done using Compact Muon Solenoid (CMS) detector and Large Hadron Collider (LHC) at CERN in Geneva. The heavy ion program at the LHC began in November 2010 and has delivered lead ion beams at the centre-of-mass energy of 2.76TeV per nucleon pair. The highest ever collision energy was critical for the analysis also because it amplified the production rate of photon-jet events and enabled to collect sufficient amount of data for analysis. In addition, the proton-proton collision experiments at the same centre-of-mass were conducted in 2011 and 2012 to support heavy ion studies.

This thesis is composed of 9 chapters.

The first chapter introduces the background knowledge to be used in this thesis. Parton models and QCD will be briefly addressed and the characteristics of Quark Gluon Plasma and Jet quenching phenomenon will be discussed.

In Chapter two, detailed phenomenology of the jets and photons in heavy ion experiments is discussed. The definition and conventions of jets will be mentioned and the reason why the $\gamma-$jet channel was chosen as the topic of this dissertation will be explained.

The third chapter describes the hardware setup of the LHC and CMS detector. In the

first section, the process of heavy ion beam production and acceleration is discussed. In the second section, detailed explanation of the sub-elements of CMS detector and the data acquisition system is explained. In addition, the trigger strategy to select the $\gamma-$jet events out of the huge amount of background is expounded.

In the fourth chapter, the Monte Carlo simulation study is reported. Collisional event simulators were used for the generation of heavy ion events and $\gamma-$jet scatterings . Those events are used for the validation of various analysis algorithms, such as the jet energy correction and the background subtraction methods.

The fifth chapter presents the detailed reconstruction procedure which converts the raw data into the higher level physics objects. Reconstruction of photons and particles will be introduced and then jet finding algorithm specialized for the CMS experiment will de mentioned. In addition, the analysis of collision impact parameter, called centrality determination, is also introduced.

The main analysis of this thesis is shown in sixth and seventh chapters. The main obstacles of $\gamma-$jet study are the contamination of the background photons from decayed neutral mesons and the background jets from underlying events. Both backgrounds were statistically subtracted using the **photon template method** and the **event mixing method** respectively. Chapter 6 was dedicated to explain the extraction of direct photon signals, and the chapter 7 will discuss detailed background subtraction.

In eighth chapter, the final result of this thesis, angular correlation and energy ratio of photon-jet pair, will be revealed. By comparing the $\gamma-$jet kinematics of heavy ion collisions with those of pp collisions and Monte Carlo simulation at the centre-of-mass energy, the modification of quark momentum due to QGP is inferred. The systematic uncertainty studies will be also reported. In addition, the phenomenological study using a toy model will be shown. The energy loss scenario inspired by perturbative QCD and constant energy loss scenario were applied in the toy model and they were compared to the real data. In particular, we will extensively discuss how the jet quenching depends on the path length though the Quark Gluon Plasma This thesis will be summarized in the final chapter. The results will be reviewed and the lessons we learned from the analysis will be reflected.

1.2 Quantum Chromodynamics

QCD is the most successful theory that can explain the strong interaction phenomena discovered so far. The ingredients of this theory are *quarks* which compose hadrons,

and *gluons* which mediates strong force between quarks. In contrary to QED where the electric charge is the only coupling quantum number, there are three kinds of charges in QCD - usually called red, green and blue. These name have nothing to do with visible colors but is used for the analogy that three sums to white. It constructs a SU(3) symmetry and the strong force is activated when the partons color is not white. In this section, a brief introduction of QCD is mentioned and the prediction about the phase transition of matter under extremely hot and dense system by QCD will be discussed.

1.2.1 Hadrons, Quarks and Gluons

Hadrons are the particles which strongly interact with each other. They can be classified into two kinds - baryons and mesons - by the number of inner constituents which are quarks. Baryons are composed of 3 quarks, for example, protons and neutrons. Mesons are composed of a pair of quark and anti-quark (anti-matter of a quark), for example , pions and kaons. Quarks are the most fundamental elements of hadrons discovered so far. They have spin 1/2 and there are 6 different kinds of quarks - up, down, charm, strange, top, bottom. and their acronyms are u,d,c,s,t and b. Quarks have another quantum number - *color charge* - which constructs a SU(3) symmetry. For the convenience of labelling, they are called blue (b), red (r) and green (green). These colors are the charges which incurs the strong force, and the origin of the name *Chromodynamics*. Detailed information of quarks are summarized in the Table 1.1. There is one more important fundamental particle, called a **Gluon**. A gluon is a massless spin-1 boson and plays the role of mediating the strong force by being radiated from or absorbed to quarks. The relation between quarks and gluons are analogous to that between electrons and photons in the QED theory. But, the major difference of gluon from photon is that its propagation length is limited to about the diameter of a proton. This property makes the strong interaction a short range force.

1.2.2 QCD Lagrangian

The actual calculation of interaction rate of the strong force is done starting from the QCD Lagrangian which was built on SU(3) Yang-Mills theory [15]. The equation is

$$\mathscr{L}_{QCD} = \sum_{\alpha} \bar{\psi}_j^{(\alpha)} (i\gamma_\mu D^\mu_{jk} - m^{(\alpha)}\delta_{jk})\psi_k^{(\alpha)} - \frac{1}{4} F_a^{\mu\nu} F^a_{\mu\nu}, \tag{1.1}$$

with the convention of summing over the repeated indices [16]. $\psi_i^{(\alpha)}$ is the fermion field

Quark flavor (symbol)	charge	current mass (MeV)	constituent mass (MeV)
up (u)	$+\frac{2}{3}$	~ 3	~ 350
down (d)	$-\frac{1}{3}$	~ 7	~ 350
charm (c)	$+\frac{2}{3}$	~ 1800	~ 1800
strange (s)	$-\frac{1}{3}$	~ 140	~ 550
top (t)	$+\frac{2}{3}$	~ 170000	~ 170000
bottom (b)	$-\frac{1}{3}$	~ 4200	~ 4200

Table 1.1: 6 flavors of quarks and their mass and charge. constituent mass includes the vacuum disturbance energy by strong interaction.

representing quarks with flavor α (= u, d, s,...), mass $m^{(\alpha)}$ and color i=R, G, B.
$_\mu$ are the 4×4 Dirac matrices. The covariant derivative $\mathbf{D}_\mu$ is defined as:

$$\mathbf{D}_\mu\psi = (\partial_\mu + i\,g_3\mathbf{A}^a_\mu\frac{\lambda_a}{2})\psi. \tag{1.2}$$

Here, g_3 is the coupling constant of the theory. λ_a ($a = 1,...,8$) are the 3×3 generator matrix of the $SU(3)$ group, which obey the commutation relations:

$$[\lambda_a,\lambda_b] = 2if_{abc}\lambda_c\ (a,b,c = 1,...,8), \tag{1.3}$$

where f_{abc} are called "structure constants" of $SU(3)$. In the end, the gluon field strength tensor is expressed as follows:

$$F^a_{\mu\nu} = \partial_\mu A^a_\nu - \partial_\nu A^a_\mu - g_3 f_{abc}A^b_\mu A^c_\nu. \tag{1.4}$$

The Lagrangian satisfies the Parity, Charge symmetry and quark flavor conservation by construction.

1.2.3 Asymptotic Freedom

As one may see from Eq. 1.1, the QCD Lagrangian is similar to QED one. The mediators of the interactions - photon for QED and gluon for QCD - are massless and have the same spin number. However, why are the two interactions so different in reality? Why is the QCD not shown in our macro level environment? The difference comes from the field tensor term in the QCD Lagrangian (Eq. 1.1). It produces extra terms when the interaction rate formula is expended in the perturbation series. In the Feynman diagram, this can be interpreted as that the gluons interact with themselves, whereas

photons do not.

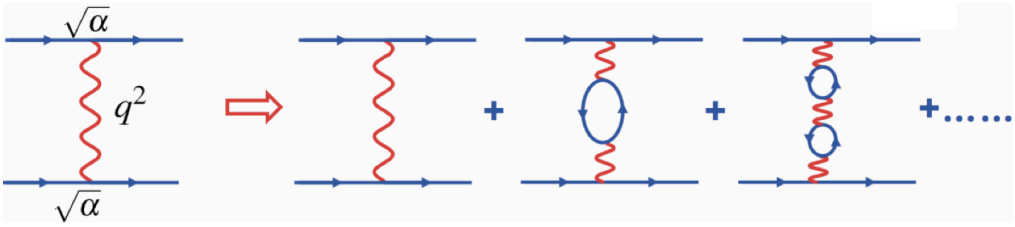

Figure 1.1: Feynman diagram of QED interaction perturbation terms.

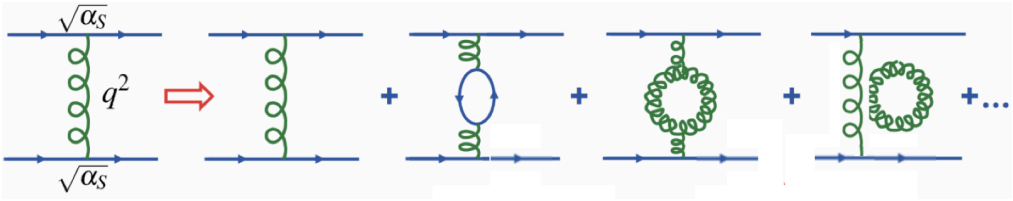

Figure 1.2: Feynman diagram of QCD interaction perturbation terms. In addition to the QED 1.1, there are gluon loops which makes the anti-screening property.

This difference determines the distance dependence of the coupling strength between two particles. Existence of an electric charge makes the surrounding vacuum polarized. So the interaction between two charged particles are screened by the polarized field. Therefore, as the distance of particles are further, there are more polarized vacuum space between them and these consequently weakens the actual force between two particles. This phenomenon is said that the effective charge is screened or **Running coupling constant** because the coupling constant depends on the distance. Similar things happen in the QCD because a gluon also polarizes the vacuum into q-$\overline{q}$ pairs. However, it is more complicated because gluons can interact with other gluons. Surprisingly, this nature makes the color charge not screened by surrounding vacuum but ANTI-screened [17]. In Non-Abelian gauge theory, there are two parameters which compete with each other to determine the distance dependence of the coupling strength. They are manifested in the one-loop beta function

$$\beta(\mathrm{g}) = -(\frac{11}{3}C_2(G) - \frac{4}{3}\mathrm{n_f C(R)})\,\frac{\mathrm{g}^3}{16\pi^2} \tag{1.5}$$

where $\mathrm{n_f}$ is the number of quark flavors, C_2(G) is the quadratic Casimir constant of the gauge group and C(R) is another Casimir invariant defined by the generator of Lie alge-

bra in R representation. When this term is positive the coupling constant enlarges for further distance between two color charges. On the other hand, if this term is negative then the coupling constant will reduce. In QCD that is the SU(3) case of Non-Abelian theory, $C_2(G) = 3$ and $C(R) = 1/2$. In the standard model $n_f = 6$. Although nobody knows if there are more undiscovered, unless we miss more than 8 extra quark flavors (total 14 quark flavors), the strong force will be anti-screened by the vacuum polars. This nature is exactly contrast to that of QED and called **asymptotic freedom** because the interaction between quarks and gluons are asymptotically small when particles are very close. On the other hand, when two particles get very far, the energy to stretch quarks are extremely high, so quarks do not exist isolated. This phenomenon is called **confinement**. It is the reason why the quarks are never observed as in the isolated state but only inside of baryons.

1.2.4 QCD Phase Diagram

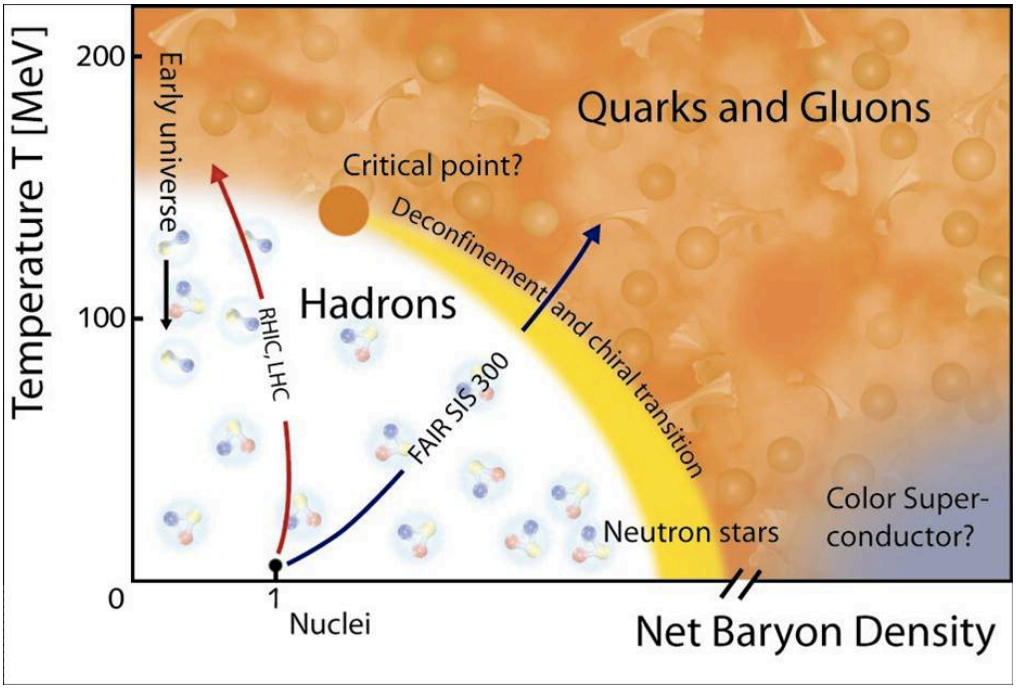

Figure 1.3: A figure taken from Ref. [18]. Phase diagram of partons and hadrons anticipated in the QCD calculation. The heavy ion collision experiment at LHC is expected to bring the vacuum into Quark Gluon Plasma state along the red vertical path in the figure.

In the previous section, we discussed about the confinement property of QCD and understood why the quarks are never found in isolated states. However, this is true only in a specific range of temperature and density of matter, including the earch where we live. The QCD theory predicts that strong force between quarks can be weakened and the quarks can freely move out of the hadron shell when the temperature is higher than a certain critical point, which is extremely high. The breakdown of confinement can be understood by studying the *effective* potential energy between $q-\overline{q}$. As already discussed in Sec. 1.2.3, the potential energy between q and $\overline{q}$ infinitely grows as the quarks move farther away. The V(r) can be computed using lattice QCD calculation as shown in Fig. 1.4 or in Ref.[19]. Hence, a $q-\overline{q}$ pair must keep distance $1/\Lambda_{\mathrm{QCD}} \sim 1$fm.

In the high temperature, however, the medium produces numerous number of $q-\overline{q}$ pairs filling the space. Those particles surround a quark and suppresses the effective color charge felt by other quarks far away. This is very similar to the Debye screening effect in a QED plasma. The effective force between two quarks now falls down exponentially as a function of distance, and now the V(r) curve is modified to have a plateau in high r regime as shown in the right panel of Fig. 1.4.

In this environment, the statistical feature of matter is completely different because the smallest elements of the thermal system are quarks and gluons, not nucleons any more. This new state is called the Quark Gluon Plasma (QGP).

1.2.5 Quark Gluon Plasma

The QCD theory predicts various phases of matter in extreme environments which are summarized in Fig. 1.3. The orange colored section in the figure is the QGP where we will pay our attention from now on. In particular, we will focus on the top left corner, high temperature and low baryon density because that is where the LHC heavy ion program can reach.

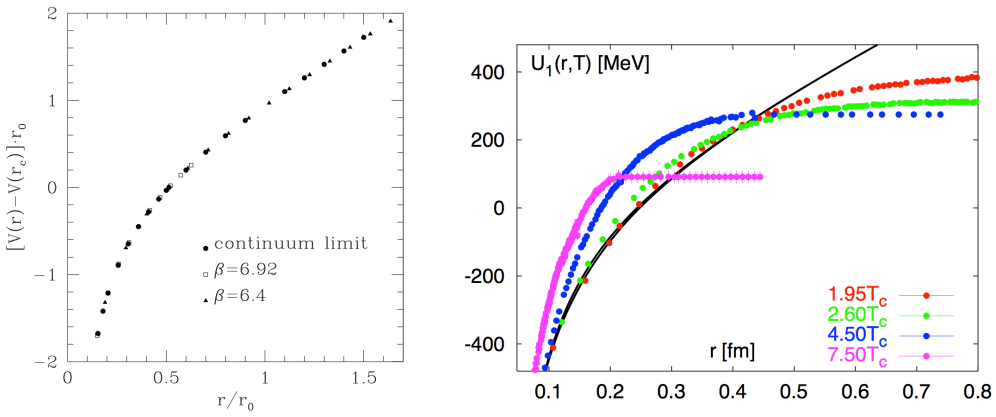

Figure 1.4: Potential between two quarks computed by lattice QCD calculation in vacuum (Left) and in thermalized medium at various temperature levels(Right).[19]. T_C ($\sim$ 170MeV) stands for the critical temperature where the phase transition happens.

2 Jet Quenching and $\gamma -$ jet Scatterng

The two main keywords of this dissertation are **Jet quenching** and $\gamma -$ jet scattering. In this chapter, we will review their nature and learn how to use them for the investigation of Quark Gluon Plasma. In Sec. 2.1.1, the definition and production mechanism of jets and photons in high energy physics experiments are discussed. General aspects of parton energy loss will be described in 2.2. By narrowing down the topic, the property of $\gamma -$ jet events will be mentioned in Sec. 2.3 and Section 2.4. After all, this chapter will be closed by the review of the past relevant experiments.

2.1 Jet Production In Vacuum

This section is devoted to explicate the definition of a jet and its relation to high energy quarks. And the method of the jet searching in the experiments will be described.

2.1.1 Definition of Jet

As explained in the previous chapter, it is impossible to directly observe an isolated parton. Imagine a quark or a gluon is apart from its parent nucleon with very high energy, for example in collision experiments. After O(1) fm/s, the energy of this parton results in the production of a shower of particles. This phenomenon is called *parton fragmentation*. If we measure the 4-vectors of all fragmented hadrons, we will be able to reproduce the parent parton's energy. However, counting the all particles in a shower is technically very hard. Another problem is that when there are several parton showers happened in a single event, it is very hard to clearly draw the family tree, because the low momenta particles can be scattered in non-collinear directions from the parent partons. Even in $e^+ + e^-$ experiment which are known to provide the smallest amount of background particles, at least 2 partons are produced at the same time. The situation is worse for nucleus-nucleus collision experiments because they are basically collisions between hundreds of valence quarks, sea quarks and gluons.

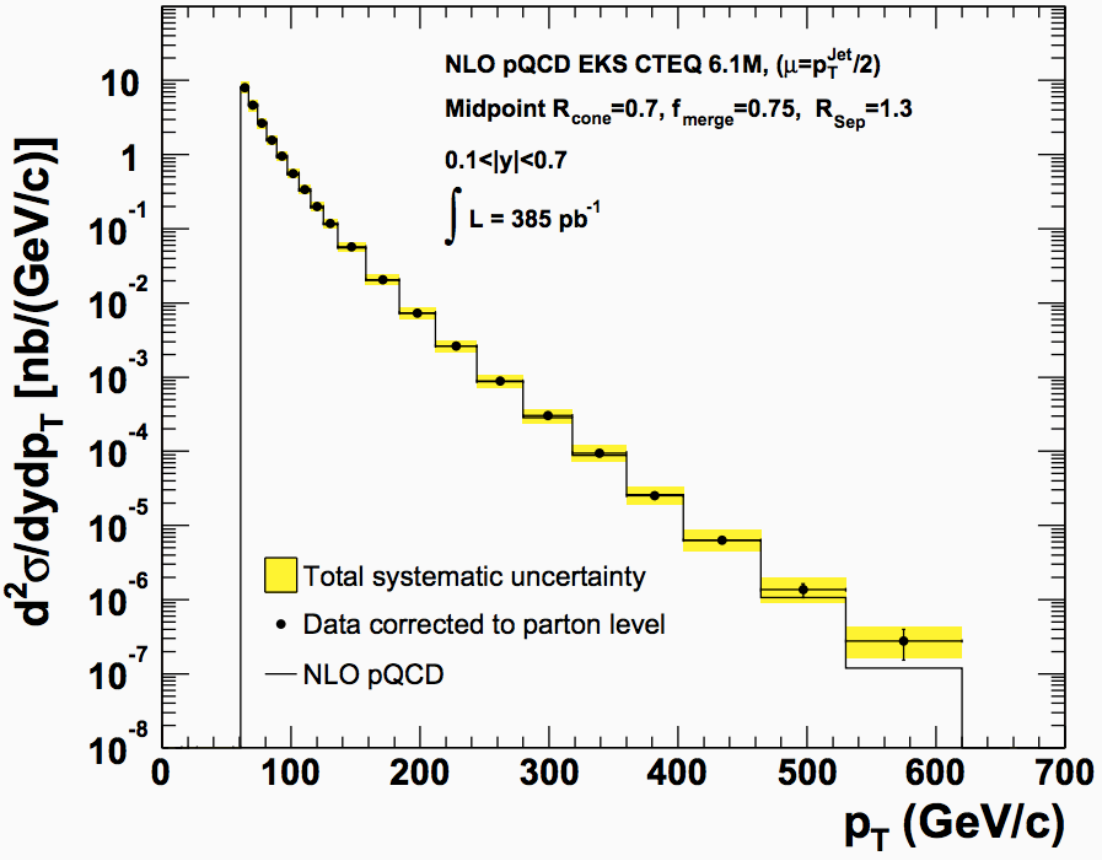

Figure 2.1: Measurement of the differential cross-section of inclusive jet using a Cone jet algorithm in CDF experiment [20]. The result agrees with NLO calculation within systematic uncertainty. (The yellow band represents systematic uncertainty, but it may not be shown in black & white prints.)

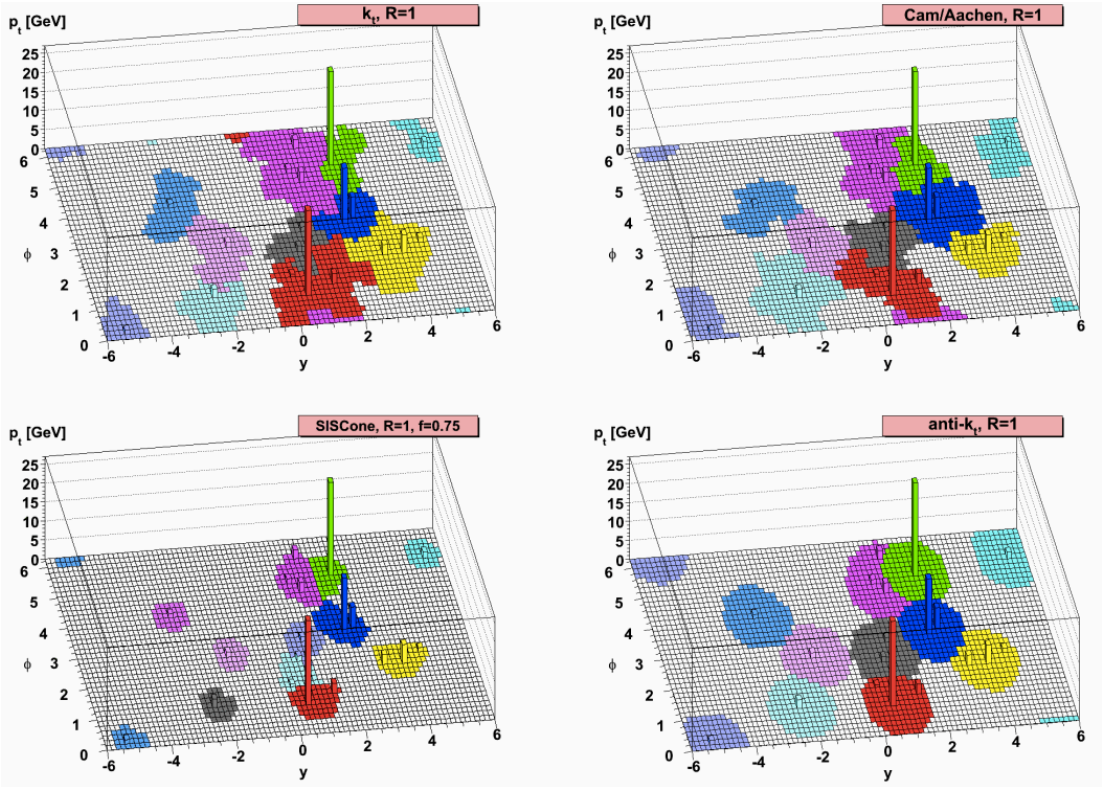

Figure 2.2: Illustration of various jet finding algorithms used to the same hard scattering event in proton+proton collision. Clockwise from top left corner : k_T, Cambridge/Aachen, SiSCone and anti-k_T algorithms [21]. The jet resolution parameter, R, was consistently set as 1. anti-k_T algorithm is the one to be used for this analysis. As shown in the illustration, all algorithms were able to catch high p_{T} jets (3 eminent topers). However, they showed discrepancies in finding low p_{T} (or soft) jets.

Then, how can we wisely bunch the particles in this situation? The idea about **jet** was made to resolve the difference between what we *wish* to measure and what we *can* measure. The critical property of high energy partons is that the fragmented particles are likely to be collinear to the momentum direction of their parent parton. Therefore, one can make a close guess of the parton momentum by finding the collimated set of high momentum particles. This is the abstract concept of a jet. Still, a few things have to be clarified - what is the criteria for being collimating? What will be the shape and size of jets? Another trouble is that the meaning of parent parton is ambiguous even at the theoretical point of view. For example, the calculation of the fragmentation of a parton depends on scale. Therefore it is important to make a clear definition of jets which can be theoretically valid and matched with experiments as well. In 1990, theorists and experimentalists sat together and made the SNOWMASS accords [22] to make a good definition of a jet. The main principles are listed below.

1. Jet definition should be simple to be used in experimental analysis and theoretical calculations.
2. It must yield finite cross sections at any order of perturbation theory - infrared and collinear safe.
3. Obtained cross sections should be relatively insensitive to the hadronization pattern.
4. It must be insensitive to underlying events.

Many developments have been made in jet finding algorithms so far and a jet became one of concrete physics observables in high energy experiments. For instance, in Fig. 2.1, the measurement of the differential cross section of inclusive jets in CDF experiment shows nice agreement with QCD calculation.

2.1.2 Jet Finding Algorithm : Anti-k_T

Among several jet finding algorithms, the one named **anti-**k_T [21] was chosen to be the most suitable for this analysis. The main reason is that it is less sensitive to the background fluctuation of the heavy ion underlying events so it gives the best performance in energy measurement. The angular distance from jet axis to particle is defined in $\boldsymbol{\eta} \times \boldsymbol{\phi}$ plane and is used as a selection determinant. Radius R is the major parameter in jet finding algorithm, which limits the angular distance of particles from the jet axis. In

heavy ion experiment, huge amount of background particles interrupts accurate jet energy measurement especially for low p_{T} range. In order to reduce the fluctuation, R was set 0.3 which is smaller then the typical value used in proton-proton collision analysis.

Below are the steps of the Anti-k_T jet finding procedure.

1. Find particles having high p_{T}ãbove a certain threshold and set them as seeds of clusters.

2. Starting from the seed of highest p_{T}, calculate the distance measures and find the smaller one between
$$d_{ij} = \min(k_{it}^{-2}, k_{jt}^{-2}) \frac{\Delta R_{ij}^2}{R^2} \tag{2.1}$$
and
$$d_{iB} = k_{it}^{-2} \tag{2.2}$$
where, k_{it} and k_{jt} are the transverse momentum of the seed and searching particles respectively and ΔR is the distance defined as
$$\Delta R_{ij} = \sqrt{(y_i - y_j)^2 + (\phi_i - \phi_j)^2} \tag{2.3}$$

3. If d_{ij} is smaller than d_{iB} the searching particle is merged into the seed jet. In the other case, it is dropped from the jet entities.

4. Step 2 and 3 are repeated until there is no seed remaining.

2.2 Jet Quenching Phenomenology in Perturbative QCD

Jet quenching means that a high energy parton is largely damped by the QGP and radiates the energy before fragmentation. Eventually, the outcome jet has less energy compared to what it is supposed to have in vacuum. Several theoretical and experimental studies are ongoing to understand this interesting phenomenon. In the theoretical side, studies can be divided into two classes by the assumption of the coupling constant between the parton and medium - weak or strong coupling (*Warning : These terminologies are different from Weak and Strong nuclear forces. Obviously, both result from strong nuclear force*). In the weakly interacting medium model, the running coupling constant is sufficiently low for perturbative calculation. Studies in this situation was broadly done by Baier, Dokshitzer, Mueller, Peigne, and Schiff [23, 24], Zakharov [25, 26] and relatively

recently by Gyulassy and Wang [27] in order to explain the results from RHIC. In the case of strongly interacting model, perturbative expansion terms do not converge. To overcome this problem, the calculation tools used in Gauge/String duality recently have been deployed in QGP and brought different prediction of parton energy loss [28, 29].

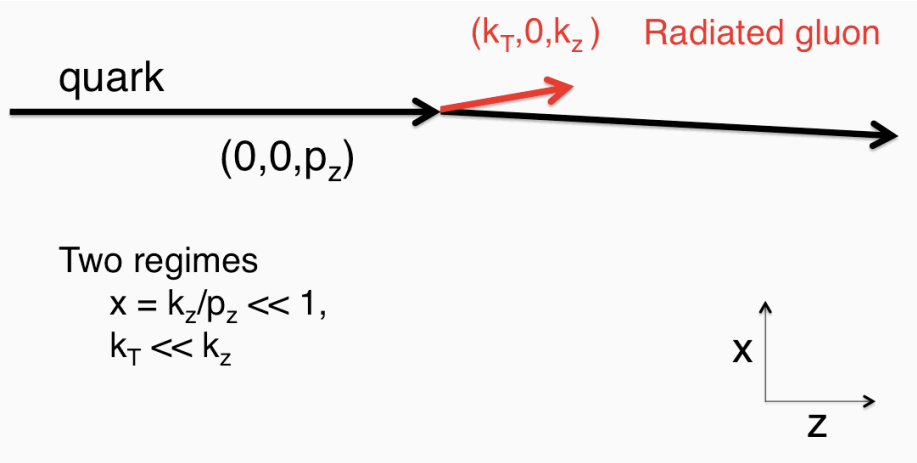

Figure 2.3: Illustration of collinear gluon bremsstrahlung of high energy quark in vacuum. Eq. 2.4 can be used in this regime.

Weakly coupled system means that the coupling constant of the vertex between the propagating parton and medium constituents are much smaller than 1 (g << 1), so we can use perturbative expansion to calculate the interaction rate. The parton energy loss can be visualized by radiation of soft gluons stimulated by the medium constituents. The Feynman diagram of this model is illustrated in Fig. 2.4. In this section, the hand-waving explanation of gluon radiation introduced by Iancu [30] and Tywoniuk [31] will be reviewed.

2.2.1 Gluon Radiation in Vacuum

Before discussing about the medium induced energy loss of a quark, it is worthy to review how a quark radiates gluons in vacuum in general. Once a quark is produced from hard scattering it is in off-shell state which means the energy is larger than the mangitude of the momentum. Several radiation of gluons make the quark lose tis virtuality and pull it closer to the on-shell state. Consider a quark is moving along z axis with momentum p_z and a gluon with energy k_z and transverse momentum $\mathbf{k}_\perp$ is emitted as illustrated in Fig 2.2. In perturbative QCD, when the fraction of longitudinal momentum

carried by the gluon is very small ($x \equiv k_z/p_z \ll 1$) the probability of this bremsstrahlung can be calculated to the first order of α_s [30].

$$\mathrm{dP_{Brem}} \simeq C_R \frac{\alpha_s(k_\perp^2}{\pi^2} \frac{d^2k_\perp}{k_\perp^2} \frac{dx}{x}, \tag{2.4}$$

where, C_R is the Casimir constant in SU(N_C). So, we can find that the radiation is likely to happen in soft (small x) and collinear (small $k_\perp$) regime. The *Gluon formation time*, $\mathrm{t_{form}}$ is defined as the typical time in which a gluon with a given kinematics to be emitted. In quantum mechanics language, a gluon becomes independent from the quark when their wave functions are de-coherent. The coherence between two objects is measured by their overlap in the transverse space. Gluon lose the coherence when its transverse separation is larger than the Compton wavelength $\lambda_\perp = 1/k_\perp = 1/(\omega\,\boldsymbol{\theta})$. Therefore, $\mathrm{t_{form}}$ can be written as

$$t_{form} \simeq \frac{2k_z}{k_\perp^2} \simeq \frac{2}{k_z\theta^2}, \tag{2.5}$$

where the factor 2 is conventional [30] . This formula can be used for parton fragmentations both in vacuum and in medium [30] .

2.2.2 Gluon Radiation in Hot and Dense Medium

Now, what is the difference of the gluon radiation in hot and dense medium? Assuming that the density of medium is very high and the mean free path of the quark is much smaller than t_{form}, the gluon can be produced by the quark's successive collisions with medium. Since the quark makes multiple scattering randomly, the gluon's transverse momentum (k_T in Fig. 2.2) is accumulated in quadrature of time. Therefore, after Δt from the initialization, the average transverse energy of a gluon grows to

$$< k_\perp^2 >= \hat{q} \times \Delta t, \tag{2.6}$$

where $\hat{q}$ is called **jet quenching parameter**. $\hat{q}$ depends on the medium temperature and the particle momentum (because it decides the running coupling). For example, the jet quenching parameter of a quark with p = 20GeV/c in T = 400MeV medium is $0.186\mathrm{GeV}^2$ [32]. Also, the jet quenching parameters can be obtained by independent calculation by Gauge/String duality [29] for strongly interacting medium.

By combining 2.5 and 2.6, we can have

$$t_{form} \simeq \sqrt{\frac{2k_z}{\hat{q}}} \quad \text{,and} k_\perp \simeq \sqrt[4]{2k_z\hat{q}}. \tag{2.7}$$

After all, the formation time is proportional to the square root of k_z and independent on $k_\perp$, which is different from t_{form} in vacuum. Coming back to the assumption we made, this Bremsstrahlung mechanism can be enabled only when t_{form} is much longer than the mean free path l and smaller than the typical size of medium L.

$$l \ll t_{\text{form}} \leq L \implies \frac{\hat{q}l^2}{2} \ll k_z \leq \frac{\hat{q}L^2}{2} \tag{2.8}$$

Combined with 2.7, the emission angle can be determined as

$$\frac{2}{\sqrt{\hat{q}L^3}} \geq \theta = \frac{k_T}{k_z} \gg \frac{2}{\sqrt{\hat{q}l^3}} \tag{2.9}$$

Hence we can see that the medium-induced gluon radiation has lower limit of emission angle and does not tend to be collinear to the parent quark. Interesting feature is that the longitudinal energy loss of the quark is dominated by the leading gluon emission,$\Delta E = \frac{\hat{q}L^2}{2}$, which is the upper limit of Eq. 2.8. Again, the L^2 scaling is due to the non-locality of the gluon formation. If the emission of gluons made by each collision were independent with each other then the energy loss will be simply proportional to L.

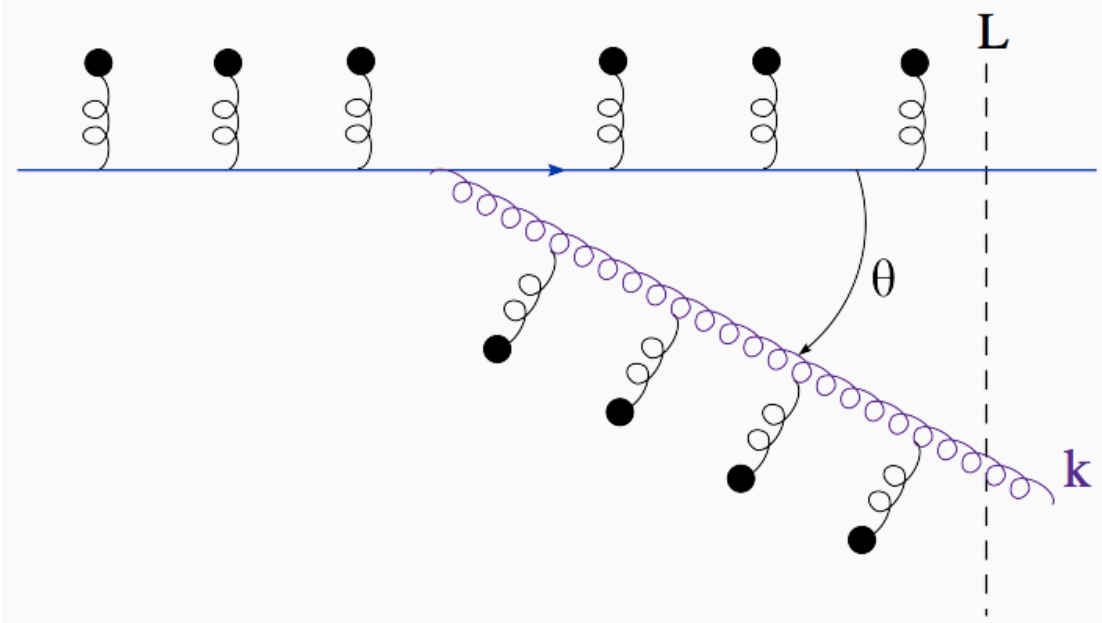

Figure 2.4: Illustration of medium-induced gluon radiation of high energy quark which is propagating though a dense medium [30].

2.3 Isolated Photon

Careful readers may have recognized that there were various adjectives for photons so far- *direct* photon, *prompt* photon, *isolated* photon, *fragmentation* photon. To avoid the ambiguity, this section is devoted to clarify the definition of various photons and explain why we want to measure **isolated** photons for the analysis. In the theoretical basis, photons can be classified in 3 categories by its production mechanism.

- (a) Prompt photons : Photons radiated from the primary collision vertex. Most of them are produced by the leading order Compton scattering and annihilation process as shown in the left-hand side of Fig. 2.5
- (b) Fragmentation photons : Photons from secondary radiation from partons after the primary hard scattering. They are produced by bremsstrahlung of quarks or fragmentation of partons as shown in the right-hand side of Fig. 2.5
- (c) Decay photons: Photons decayed from mesons, such as $\pi^0 \rightarrow \gamma + \gamma$ channel. They are the major backgrounds that we want to reject.

First of all, (c) decay photons can be removed out of our attention because they are major backgrounds which will be subtracted in this analysis. Among (a) and (b), the prompt photons are better objects both in experimental point of view and in perturbative calculation. Prompt photons have good back-to- back property in azimuthal angle with the recoiled parton, so it is easy to observe from experiment. Plus, the calculation of cross-section agrees well with experiments [33–35]. On the other hands, the fragmentation photons are made in the middle of jet production. The calculation of fragmentation function using QCD is more challenging because one needs to compute higher orders of perturbation series [36]. Furthermore, it is very hard to measure the inclusive fragmentation photons in experiment because fragmentation photons are usually located inside jets. Therefore, we prefer to measure (a) and reject (b) as much as possible.

In hadron collision experiments, however, it is not easy to perfectly distinguish (a) prompt photons from (b) fragmentation photons due to the underlying events. Some prompt photons can be surrounded by many particles from underlying events and look same to fragmentation photons. There is another ambiguity in the border of (a) and (b) - the scale dependence. Imagine that a parton is scattered and radiated a photon taking almost all momentum. In a smaller scale, this is classified as a fragmentation photon. However, in larger scale calculation, the vertex can be merged together in Feynman diagram and this can be seen as a leading order process.

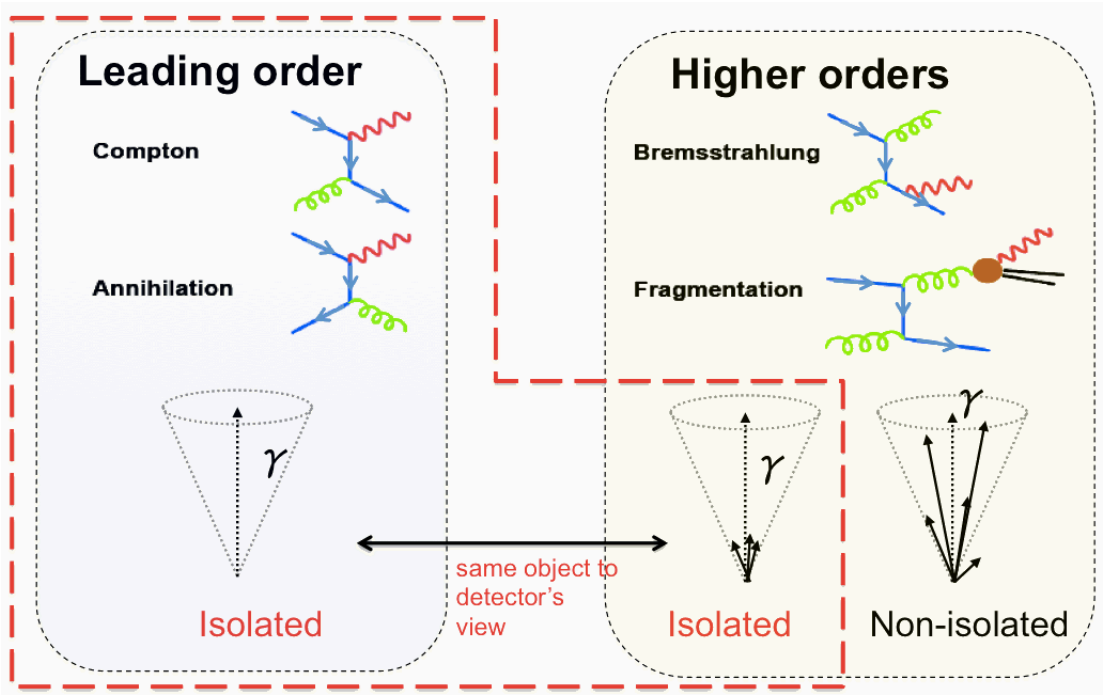

Figure 2.5: Leading Order photons are the best observable for physics study for its simplicity of production mechanism. However, it is practically impossible to completely distinguish them from fragmentation photons in both pp and Pb-Pb experiments. Isolation criteria provides the reasonable borderline in manner of feasibility of experiment and perturbative calculation.

The **Isolation** criteria is introduced to reconcile this obstacle. Requiring a certain limit of energy around photons, we can keep of prompt photons and reject large fraction of fragmentation photon. The biggest advantage of this cut is that the perturbative calculation of the cross section of isolated photons is well understood. The typical uncertainty of isolated photon cross-section in NLO calculation is less than 10% according to JETPHOX program [37, 38]. Technical details about the isolation criteria will be discussed in Sec. 4.2.2.

2.4 Photon (γ) : A great tool to probe into initial state of hard scattering

Direct photon is a clean signal in QCD backgrounds because it does not have any color charge. For the last 2 decades, the biggest interest involved with the direct $\boldsymbol{\gamma}$ in pp collisions have been related to the gluon distribution function. The parton distribution function (PDF) of quarks has been intensively studied in the past using deep inelastic scattering in the SLAC-MIT experiment [39] and the HERA experiment [40]. In order to study the gluon PDF, proton+proton or proton+ anti-proton collisions need to be done to make strong interaction. The photon production is one of the simplest channels made by a gluon scattering. Recently, CDF, D0 at 1.96TeV and CMS experiment at 7TeV [41] has measured the differential photon cross-section by this motivation.

2.4.1 Preservation of Initial States of Hard Scatterings in PbPb Collision

Can the hard scatterings in heavy ion collisions be understood as a simple superposition of the ones in pp collisions? In other words, would the initial state of hard scattered partons be already modified even before propagating the medium due to the other nucleons in the ion? This is a very important question because the physics observables in pp collision at the same $\sqrt{s_{NN}}$ with heavy ion are usually used as the reference for the PbPb experiment. To prove the preservation of initial state of the hard scattering, CMS collaboration measured the cross section of isolated photons in PbPb at $\sqrt{s_{NN}}$=2.76TeV and compared to pp collision [46, 47].

A scaling factor, the nuclear overlap function T_{AA}, is needed to provide proper normalization to compare the cross sections of high-p_{T}photon in pp and PbPb. T_{AA} was computed with the Glauber model [48]. The value varies from 1.45mb^{-1} to 23.2mb^{-1} depending on how much the collision is head-on. The "head-on"ness is quantized

as centrality which will be explained in Sec. 5.1. This factor, equal to the number of nucleon-nucleon (NN) collisions, $N_{\rm coll}$ (to be explained in Sec. 5.1) can be interpreted as the NN-equivalent integrated luminosity at any given PbPb centrality. The LHC collaborations use a common nucleon-nucleon inelastic cross section of $\sigma = 64 \pm 5$ mb at 2.76 TeV, based on a fit of the existing data for total and elastic cross sections in proton-proton and proton-anti-proton collisions.

Combining the all scaling factors, the nuclear modification factor ($R_{\rm AA}$) defined as

$$R_{\rm AA} = dN^{\gamma}_{\rm PbPb}/dE^{\gamma}_{\rm T}/(T_{\rm AA} \times d\sigma^{\gamma}_{\rm pp}/dE_{\rm T}), \tag{2.10}$$

is computed from the measured PbPb scaled yield for each centrality and the pp differential cross section. If the production rate of isolated photon in PbPb collision per $N_{\rm coll}$is same to that in proton-proton collision , then $R_{\rm AA}$will be 1. If it is enhanced $R_{\rm AA}$will be higher than 1, and if quenched then $R_{\rm AA}$will be smaller than 1.

Figure 2.6 displays $R_{\rm AA}$ as a function of the isolated photon $p_{\rm T}$ for the 0–10% most central PbPb collisions. And The ratio is compatible with unity within the experimental uncertainties for all $\mathbf{E_T}$ values. And Fig. 2.7 shows the dependence of $R_{\rm AA}$on both centrality and $p_{\rm T}$.Clearly, the results show that $R_{\rm AA}$is always one for all circumstances. This confirms the preservation of initial state of hard scattering as well as the validity of $N_{\rm coll}$scaling of the Glauber model . Similar studies were done for the Z^0 [49] and $W^{\pm}$ [50] bosons, which came up with the same conclusion.

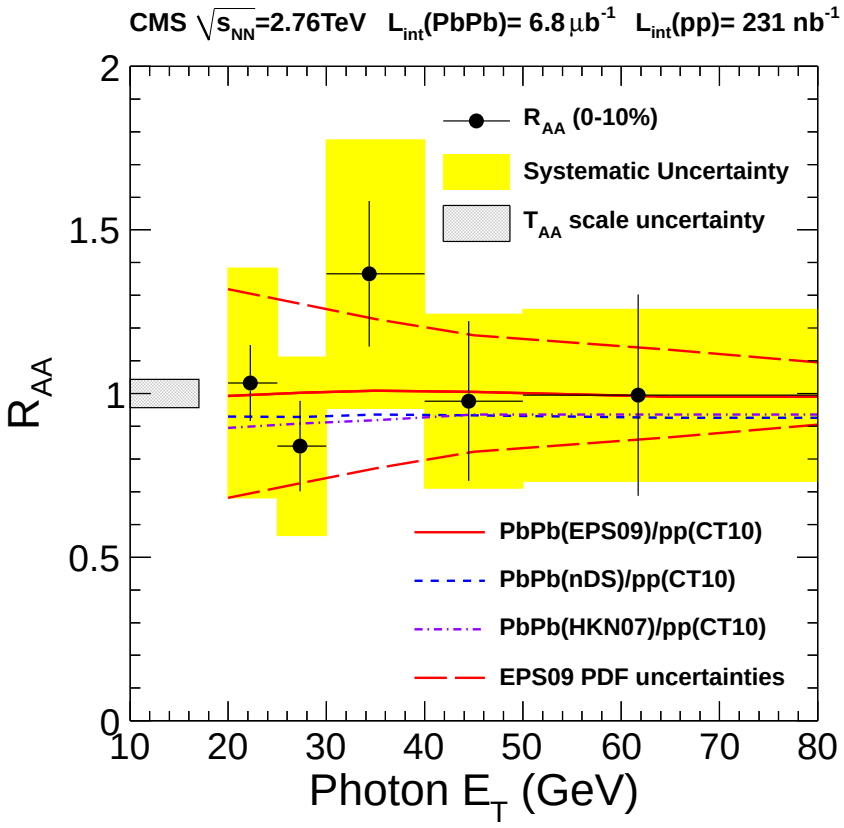

Figure 2.6: Nuclear modification factor R_{AA} as a function of the photon p_T measured in the 0–10% most central PbPb collisions at 2.76 TeV. The vertical error bars indicate the statistical uncertainty. The total systematic uncertainties without the T_{AA} uncertainty are shown as yellow filled boxes. The T_{AA} uncertainty, common to all points, is indicated by the box on the left-hand side. The curves show the theoretical predictions obtained from JETPHOX program [37] for various nuclear PDFs [42–45] The uncertainty from the EPS09 PDF parameters is shown as the red dashed lines.

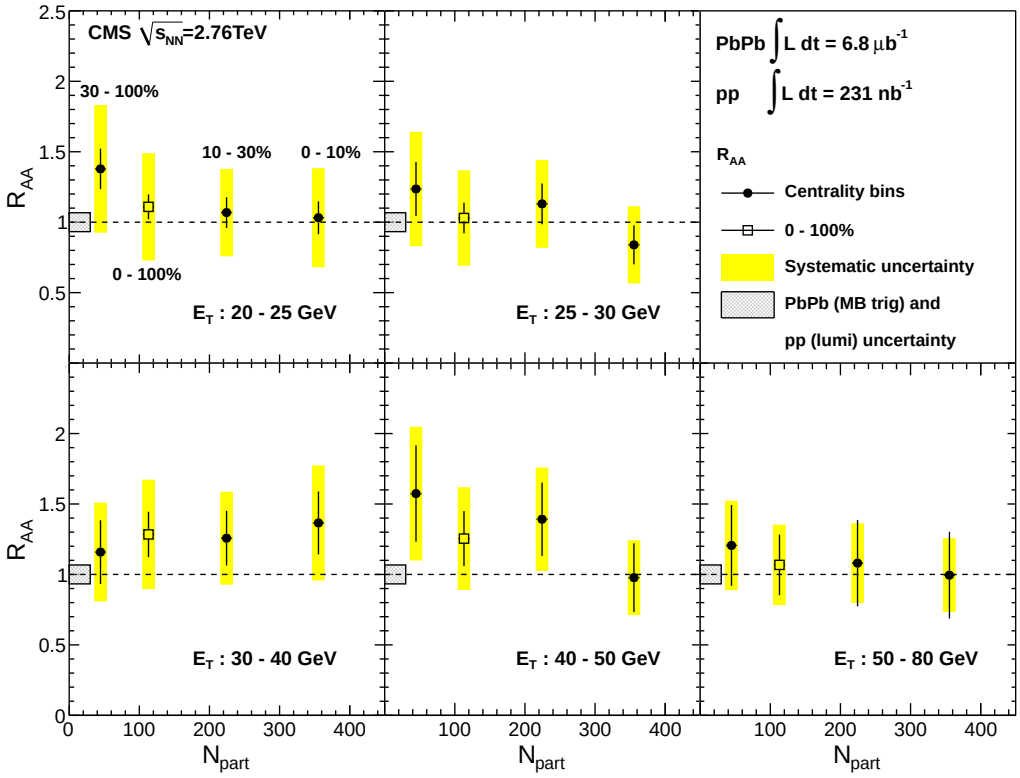

Figure 2.7: The measured nuclear modification factor R_{AA} as a function of PbPb centrality (given by the number of participating nucleons, N_{part}, to be explained in Sec. 5.1) for five different photon transverse energy intervals. The error bars on each point indicate the statistical uncertainty. The systematic uncertainties are shown as yellow boxes, including the centrality dependent T_{AA} uncertainty. The common uncertainties related to event selection efficiency and and pp integrated luminosity are shown as grey hatched boxes around unity. [46]

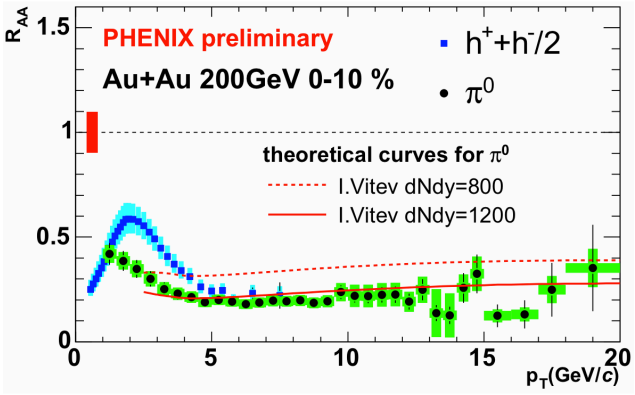

Figure 2.8: R_{AA} of charged hadrons and π^0 in PHENIX experiment in the most head-on (central) Au+Au collision, and their corresponding theoretical predictions. The number of high p_{T} particles are suppressed as much as factor of 5.

2.5 Results of Past Experiments

Due to the low collision energy and luminosity, experiments in RHIC have not shown the direct correlation results of $\gamma-$jet. However, they were able to show indirect evidence of jet-quenching by searching the correlation between photon and high-p_T charged particles [51, 52]. We will review those results. In addition, the CMS results on jet quenching observation from di-jet events will be discussed.

2.5.1 R_{AA} of High p_{T} Hadrons

Suppression of high p_T hadrons in heavy ion collisions has been a indirect evidence of jet quenching [53–58]. Using the method described in Sec. 2.4.1, the $R_{\mathrm{AA}}$of charged hadrons were measured in various experiments and they consistently found significant suppression of high p_{T} particles. Fig. 2.8 shows the charged particle R_{AA}result of PHENIX experiment at RHIC. The number of hadrons above 10 GeV/c were suppressed by factor of 5 in the most head-on collision events.

Measurement of high p_{T} particles were followed by LHC heavy ion experiments with much more extended p_{T} reach [59, 60]. In Fig.2.9, the R_{AA} value rises up from 10GeV/c and then become flat at 0.5 from 40GeV/c. As one can see from the reference theory curves, the R_{AA} study at CMS and ALICE gave constraints on various theoretical models. Yet, it is not clear what kind of modification happened to individual jets. Maybe, half of jets were selectively disappeared and rest jets were not modified at all. Or maybe, all the

jets lose their energy by equal amount so the spectra were shifted to the lower p_{T}region. Therefore, measurement of particle spectra does not provide the comprehensive picture of jet quenching.

2.5.2 Two Particle Correlation Result

Another interesting result from RHIC experiments is the suppression of the correlation of back-to-back high p_{T} hadrons [14]. The STAR collaboration measured the azimuthal angular correlation of high p_{T} charged particles in mid-rapidity. A particle in range of $4\mathrm{GeV/c} < p_{\mathrm{T}} < 6\mathrm{GeV/c}$ was tagged and the $\Delta\phi$ with associated particles in $2\mathrm{GeV/c} < p_{\mathrm{T}} < p_T^{trigger}$ was measured in p+p and Au+Au collisions (also in d+Au collision) at the same collision energy $\sqrt{s_{\mathrm{NN}}} = 200\mathrm{GeV/c}$. As shown in Fig. 2.10 there are two strong correlations at 0 and π radian in pp collision (solid line). The first peak at $\Delta\phi = 0$ represents the particle pairs decayed from the same jet. And the second peak at $\Delta\phi = \pi$ represents the particle pairs radiated from each of back-to-back jets which is made by the momentum conservation on transverse plane. In Au+Au collision (blue data point), the first peak of the correlation is found, however the second peak completely disappeared. It indicates that either one of the jet pairs was absorbed by the medium produced by Au+Au collision or the jet lost its function to fragment into high p_{T} particles.

As shown in the last few sections, several results using hadron observables show the evidence of jet quenching. However, it can not clearly pin down the phenomenology because we still do not know what happens during the evolution from parton to hadron. What we are really interested is not the *hadron quenching*, but *jet quenching*.

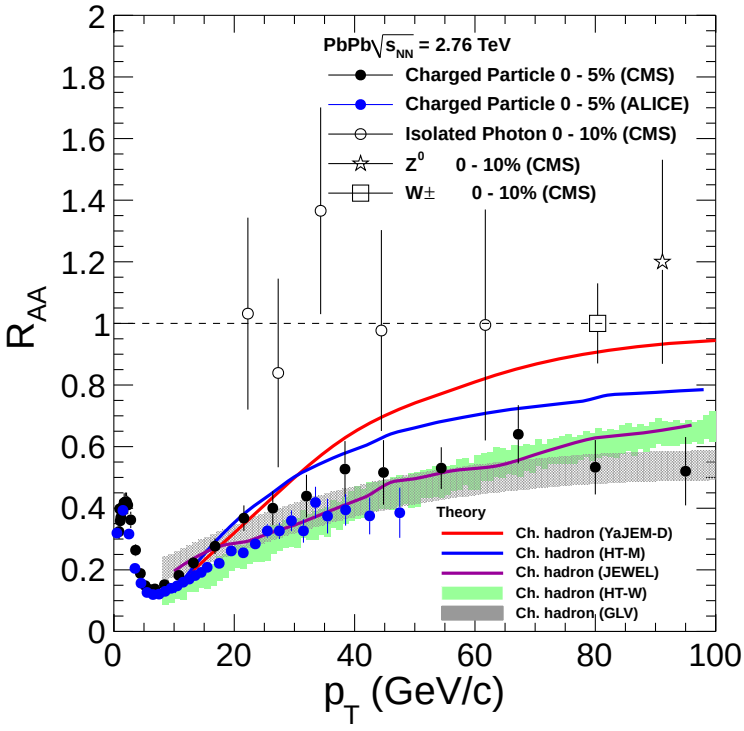

Figure 2.9: R_{AA} of charged hadrons, isolated photons, Z^0 and W bosons in the most central Pb+Pb collisions (top 10% central for CMS and top 5% for ALICE) at $\sqrt{s_{NN}} = 2.76$TeV. The centrality indicates that the impact parameter of collisions, as well as the size of produced medium. Details about centrality will be introduced in Sec. 5.1 The R_{AA} of charged hadrons are significantly lower than 1, meaning that their parent jets were suppressed. On the other hand, the R_{AA}'s of direct photon, Z^0 and W bosons are all consistent with unity because they are colorless and do not strongly interact with medium. The unity R_{AA} can also underline that the initial states of hard scatterings is heavy ion collisions is equivalent to that of pp after simple scaling by number of binary collisions. (This will be discussed in Sec.2.4.1) indetail.

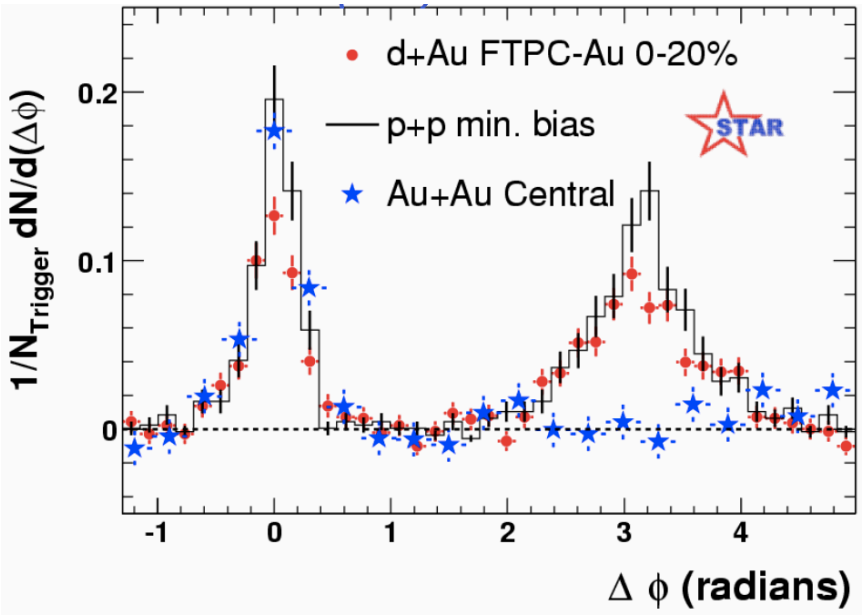

Figure 2.10: Two particle correlation results from STAR experiment [14]. Charged particles in 4 GeV/c $< p_{\mathrm{T}} <$ 6 GeV/c range were used as trigger and associated particles with 2 GeV/c $< p_{\mathrm{T}} < p_T^{trigger}$ were searched to obtain the di-jet yields. In Au+Au events, associated particles completely disappeared. It indicates that one of di-jet pairs lost energy more than the other because its propagation length in medium was longer than the other.

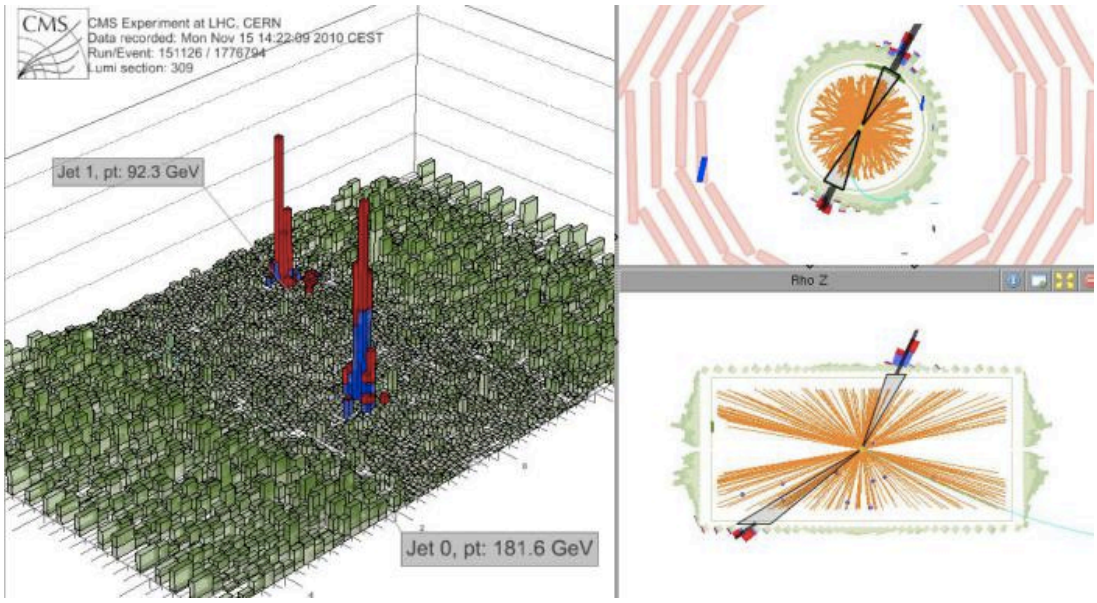

Figure 2.11: One example of back-to-back dijet events collected by CMS detector. Moment of jets are large enough to be distinguished from the bubble of background energy fluctuation (Green).

2.5.3 Dijet Asymmetry Observed in LHC

From November of 2010, the heavy ion collision at LHC launched at the center of mass energy of 2.76TeV, which is 14 times higher than at RHIC. By virtue of the high collision energy and intense luminosity CMS experiment collected very high p_{T} jets, higher than 100GeV/c. The energy of selected jets are much more eminent than the background energy fluctuation by underlying events around itself. One example is the event display of PbPb collision in Fig. 2.11. With almost full jet reconstruction efficiency (and very low fake rate), CMS were select back-to-back dijet events which is originated from hard scattering of two partons. In pp, both jets usually have similar transverse momenta by conservation law. But, as you can see from the example figure 2.11, CMS found that large fraction of jet pairs had significant imbalance which is out of scope of energy resolution range.

This imbalance can be possibly explained as following. The hard scattering was produced near the surface (but inside) of hot and dense medium, therefore the path length of one parton through medium was longer than its partner. As the parton was exposed to the medium longer than the other, it loses more energy and this makes the severe jet momentum asymmetry.

Careful analysis was done by quantifying the jet momenta imbalance into $\frac{p_T,2}{p_T,1}$ which is t he p_{T} ratio of sub-leading jet to leading jet. Its dependence on collision centrality and leading jet p_{T} was studied [61, 62]. As shown in Fig. 2.12, the p_{T}ratio is significantly smaller for central collisions compared to peripheral events for overall leading jet p_{T}bins.

In this figure, the p_{T} ratio monotonically increases as a function of $p_T, 1$ for all centrality bins. This phenomenon results from not only jet quenching but the nature of hard scattering. In order to separate two sources, a Monte Carlo (MC) simulation was used as a reference - open square points in figure. This MC sample imitates the jet production in heavy ion environment, except that the jet does not lose energy by medium. As shown in this figure, the p_{T} ratio in MC sample is closer to unity compared to data, but has similar slope as a function of $p_T, 1$.

On the bottom of Fig 2.12 the average $\frac{p_T,2}{p_T,1}$ in data was subtracted by that in MC in order to extract the effect by jet quenching only. The result shows that the jet quenching give rise to the momentum asymmetry of di-jet pairs 10% of leading jet $p_T, 1$, and this effect is independent on $p_T, 1$.

This result provides more detailed information about the medium endued energy loss than hadron correlation results and helps to build the comprehensive picture of jet quenching. However, there is a major weak point to make complete measurement of jet quenching. As both of parton pairs lose energy, we do not know the initial energy of them before they propagates the medium. The main motivation of this thesis is to overcome this point. For the rest of this thesis, the measurement of various physics observables in γ-jet events and their physics message about jet quenching will be discussed.

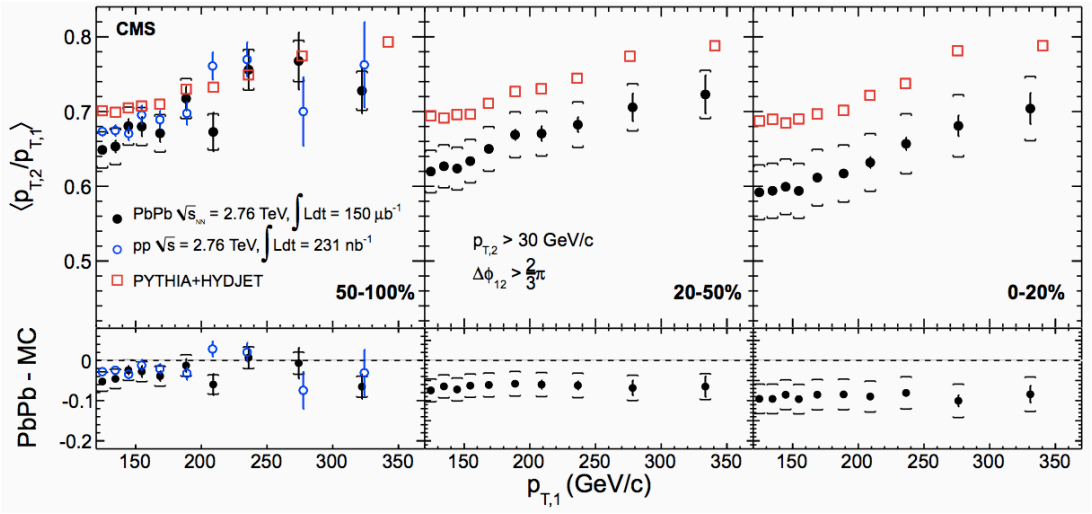

Figure 2.12: Momentum ratio of dijet pairs ($\frac{p_{T,2}}{p_{T,1}}$) and its dependence on medium size and leading jet $p_T,1$ [62]. The percentiles (50-100%, 20-50% and 0-20%) represents the size of medium (See Sec. 5.1). PYTHIA+HYDJET, MC simulation to be explained in Sec. 4, was used as reference events in which jets are not quenched. The discrepancy between data and MC results are gradually increased as the medium size gets larger, which means that jet quenching depends on the partons' path length in medium.

3 LHC and CMS

The particle accelerating system and detecting apparatus are reviewed in this chapter. The LHC enables the protons and heavy ions to be accelerated at the extremely high energy and then collided at superb luminosity [63]. Then, the collision events are recorded by CMS detector and delivered on our hand for the analysis [64].

3.1 The Large Hadron Collider

The LHC is the largest particle accelerator ring and produce the highest energy proton and heavy ion beams in the world. It is located underground near CERN in Geneva, crossing the border of Switzerland and France (Fig. 3.1). The diameter of the ring is 27 km and can speed up protons up to 14 TeV. In order to keep the beams in the circular orbit 1,232 dipole magnets are operating and 392 quadrupole magnets are used to focus the beams. The design luminosity of the proton-proton collision is $10^{34}\text{cm}^{-2}\text{s}^{-1}$.

The particle beams are gradually accelerated up to a certain lower energy by subordinate accelerating systems before entering the LHC main ring. The proton beams starts from LINAC 2 (50MeV/c) and go though SPB (1.4GeV/c), PS (26GeV/c) and SPS [63] to reach to 450GeV. The heavy ion beams - Pb^{208} - start from LINAC 3 and go though LEIR before entering the sequence of PS $\rightarrow$ SPS $\rightarrow$ LHC. LHC can generates two beams circulating in the opposite directions, so it is possible to make the collisions of p+p, Pb+Pb and p+Pb.

3.2 Compact Muon Solenoid

There are several collision points on the ring where an experiment can be done. One of them is Point 5 (or P5) where CMS detector is located as shown in Fig. 3.1. The main components of CMS are a superconducting solenoid magnet which provides magnetic filed of 3.8T, silicon trackers, lead tungstate electromagnetic calorimeter (ECAL),

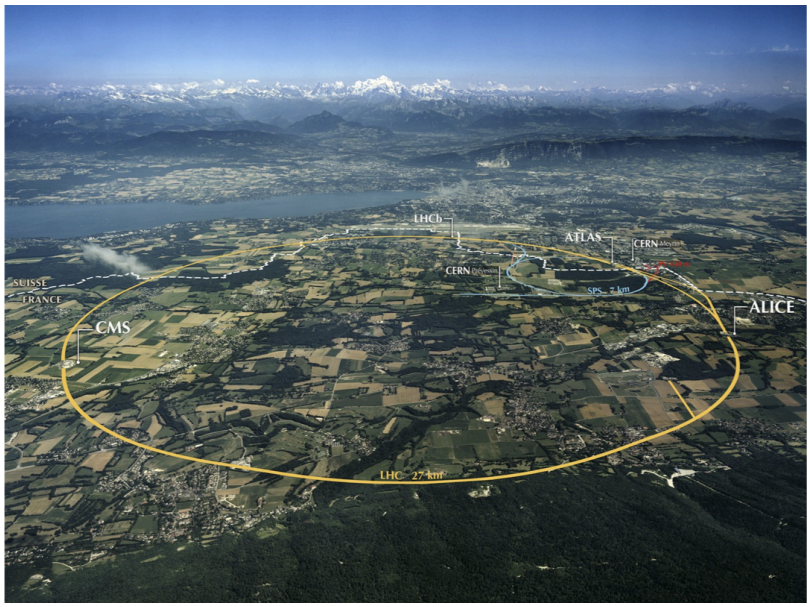

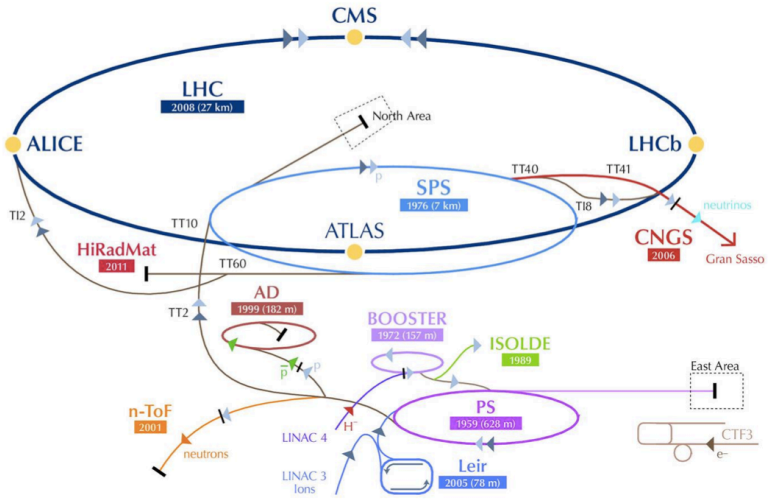

Figure 3.1: (Top) LHC ring is located underground of border between Switzerland and France. (Bottom) Proton and heavy ion beams are accelerated up to 450GeV times the number of protons by a series of supporting accelerators and then enter to the LHC ring.

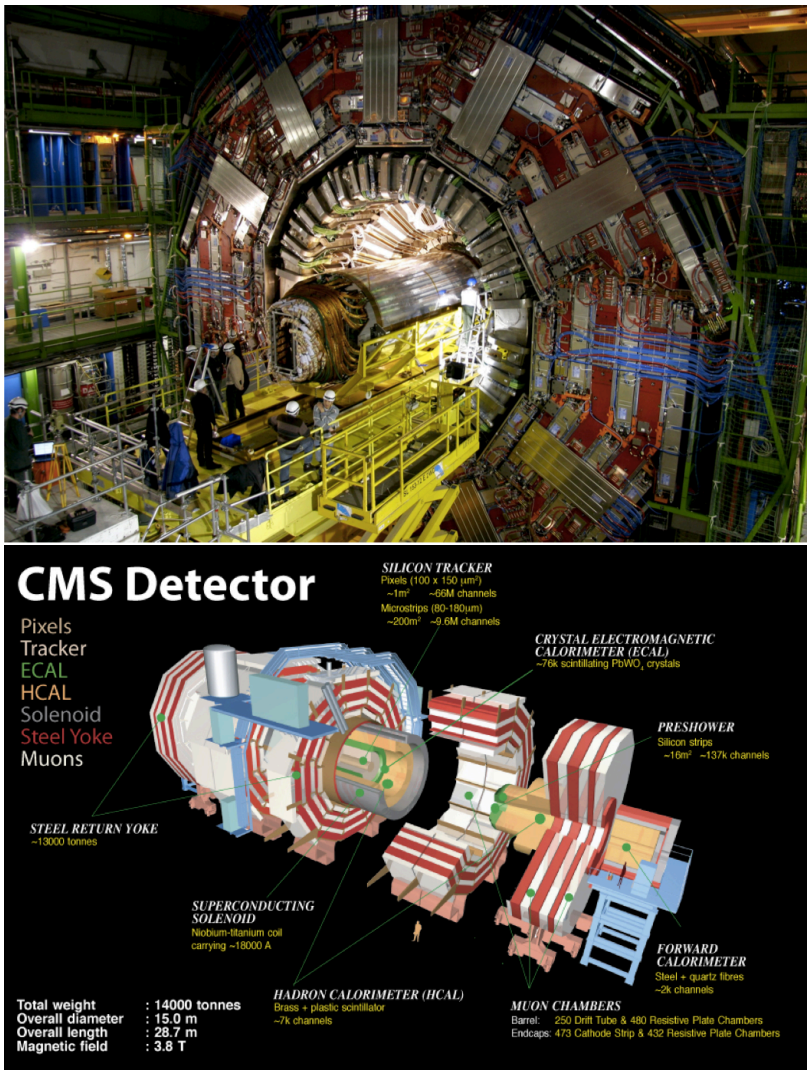

Figure 3.2: Picture of CMS detector and its components.

brass/scintillator hadron calorimeter (HCAL) and composite muon detecting system outside of the solenoid. The geometry of sub-detectors can be found in Fig. 3.2.

3.2.1 Tracking System

The silicon tracking system measures the momenta of charged particles in $\left|\eta\right| < 2.5$. It consists of 1,440 silicon pixels and 15,148 silicon strip modules. By means of fine segmentation, the impact parameter resolution is $\sim$15μm. So it can measure very high transverse momentum particles with excellent accuracy. The resolution is only $\sim$1.5% for 100GeV charged particles. More Details about the CMS tracking system can be found in Ref. [65].

3.2.2 Electromagnetic Calorimeter : ECAL

Electromagnetic Calorimeter (ECAL) is the sub-detector designed to measure photons and electrons as they deposit all of its energy on ECAL. Composed of 75,848 lead tungstate ($PbWO_4$) crystals, the ECAL covers $\left|\eta\right| < 1.479$ in a barrel region (EB) and $1.479 < \left|\eta\right| < 3.0$ in two endcap regions (EE). Each crystal in the barrel has the width of 0.017 in pseudo-rapidity and 0.017 in azimuth (ϕ). The energy resolution for photons with transverse energy of 60GeV is about 2% in p+p collision events. More details about ECAL can be found in Ref. [66].

3.2.3 Hadronic Calorimeter : Hcal

Hadronic Calorimeter (HCAL) is designed to measure the energy of hadrons and to reconstruct jets. The HCAL cells have widths of 0.087 in pseudo-rapidity and 0.087 in azimuth (ϕ). Each HCAL cell maps to 5×5 ECAL crystals arrays in order to form calorimeter towers projecting radially outwards from the nominal interaction point. Combined with ECAL, the calorimeter towers can measure jets with $\sim$ 5% resolution for 100GeV/c jet. More details about HCAL can be found in Ref. [67].

3.3 Collision Event Selection

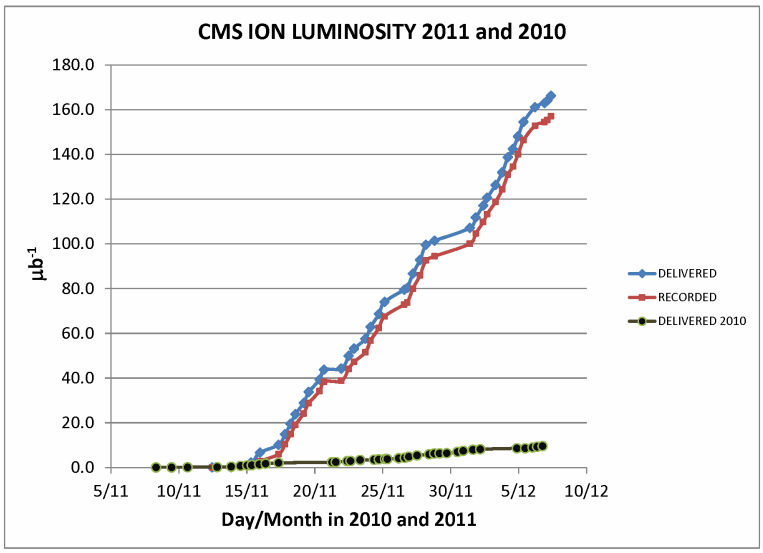

Figure 3.3: Recorded integrated luminosity for the Heavy Ion runs.

The primary dataset used in this thesis is PbPb collisions taken from Nov. 11, 2011, 23:57 UTC to Dec. 2nd, 2011, 03:26 UTC. The corresponding CMS run numbers are from 181530 to 183013 and the integrated luminosity is 150 μb^{-1}. Figure 3.3 shows the recorded integrated luminosity during the data taking period. Red symbols show sampled luminosity, when the CMS trigger and DAQ worked. As the cross section for hadronic inelastic collisions is expected to be 7.65 barns, the total integrated luminosity of 150 μb^{-1} corresponds to about 1 billion inelastic collisions of lead ion pairs. It would have been superior if all the collision events can be saved in storage tapes. However, due to the limited bandwidth of the downstream in DAQ system, CMS were able to save only 300 Hz out of total event rate which reaches up to 3,000 Hz. This does not mean that we must lose 9/10 of all interesting events, for example Gamma-jet events. The events containing high p_{T} photons, which are useful for this analysis, are very rare. For instance, a photon with p_{T} above 40GeV is produced per about 10,000 collisions Therefore, one can design an online event selection system which enables to fill the 300 Hz bandwidth with only interesting events and veto rest other events. For these reasons,

the CMS trigger system was deployed to provide a very efficient and clean selection of events in which the analyzers are interested. The major hard probe trigger channels are high-p_{T} photons, jets and muons, and each occupies 50Hz - 100Hz out of the total bandwidth.

The rest of the available bandwidth was used to record randomly selected inelastic collision events for many purposes including trigger performance monitoring. Such events are called **Minimum Bias**, or MinBias, events as it represent the most typical inelastic collision events. In order to save all high p_{T} $\gamma-$jet events, an ECAL trigger named **HLT_HIPhoton30** was developed for this analysis, which is fully efficient for the events containing photons with $p_{\mathrm{T}} > 40$GeV/c.

3.3.1 Online MinBias Trigger

The CMS apparatus has various ways to trigger on PbPb collisions, mostly using the sub-detectors in forward region. It have used the Beam Scintillator Counters (BSC) and Hadronic Forward Calorimeter (HF) triggers to select inelastic PbPb collisions. The geometry and additional information of BSC and HF can be found in Ref. [68].

MinBias collisions were selected by two clean and highly efficient triggers. One is the BSC “threshold 1" trigger based on trigger based on BSC which is installed on $3.23 < |\eta| < 4.65$. This requires at least one segment of BSC fired on both forward and backward sides. The BSC has 16 segments on each side (a total of 32 segments). Most ($\sim$ 75% of) the collisions illuminate all 32 segments, thus the effect of one dead channel on the overall trigger efficiency is negligible. The second MinBias trigger system is based on HF installed on $2.9 < |\eta| < 5.2$. It requires at least two HF towers to be fired. The thresholds in HF towers are controlled by a firmware. It has the similar efficiency as the BSC coincidence and the fake rate is very low. It is also more in line with (but less strict than) the offline event selection, which uses HF as well.

The minimum bias trigger was all accepted at L1 level until the collision rate reached 60 Hz, and then a luminosity dependent prescale was applied to keep the accept rate of minimum bias collisions at a constant rate of $\sim$ 50 Hz to fit into 300 Hz total HLT physics trigger limitation. The MinBias triggered sample was used to check the photon trigger efficiency and the energy fluctuation of the underlying events.

3.3.2 Rejection of Non-Collision Events

In order to clean the non-collision background events made by beam gas, PKAM (Previously Known As "Monster") events and ultra peripheral events, more cuts have been applied at offline. These cleaning cuts have only a small effect on the number of selected events. The strategy described below was used not only for MinBias events, but for all the events used for the overall analysis in common.

1. BSC halo filter: If a lead ion was distracted and scattered by beam gas or beam pipe, it can react with a forward sub-detector which may fire a MinBias trigger without real collision. To avoid those, events where any of the BSC halo bits

- Technical bit 35 : L1Tech_BSC_halo_beam2_inner.v0
- Technical bit 36 : L1Tech_BSC_halo_beam2_outer.v0
- Technical bit 37 : L1Tech_BSC_halo_beam1_inner.v0
- Technical bit 38 : L1Tech_BSC_halo_beam1_outer.v0

were excluded from the analysis. Figure 3.4 shows a correlation between the number of hits in the first pixel layer and the total HF energy. Collisions passing all offline event selections (colored points) have a very tight correlation between the two quantities. However, events that fire the BSC beam halo bits have very small HF energy and quite a large number of pixel hits (points near vertical axis). These are excluded from the analysis.

2. Requirement of a reconstructed 2-track primary vertex was imposed: A well-identified vertex must be reconstructed. In peripheral events, all tracks above 75 MeV/c transverse momentum were used to reconstruct the vertex. In central events, the minimum p_T requirement was increased, and the tracking region was narrowed down, to keep the maximum number of fitted tracks stable around 40–60, ensuring time-efficient reconstruction. This requirement removes non-inelastic-collision events (e.g. beam-gas, UPC) with large HF energy deposits but very few pixel hits

3. A cut to remove PKAM events, which is a requirement of pixel cluster-length compatibility with the vertex. It removes a event where a particle went though a layer of the silicon detector in longitudinal direction.

4. A requirement of an offline HF coincidence, which requires at least 3 HF towers on each side of the interaction point in the HF with at least 3 GeV total deposited energy.

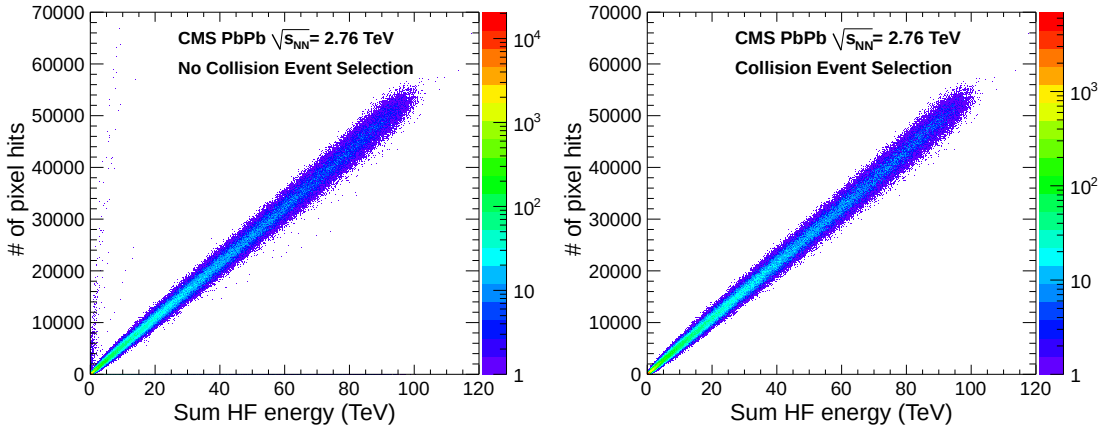

Figure 3.4: (Left) Correlation between the number of pixel hits and the total energy deposited in the HF. Good collisions have a sharp correlation, while events firing the BSC halo bits, displaying PKAM-like features, or lacking a valid reconstructed vertex are off-diagonal. (Right) The same correlation for only those events passing all selection cuts described in the text.

3.4 Selection of High p_{T} Photon Events

3.4.1 Photon Triggering

By means of the fast response timing, ECAL can be used as a part of the triggering system. *L1_SingleEG5* is the name of Level 1 trigger based on ECAL. It is the first requirement of the photon event selection. Events are selected by this trigger when it has at least one ECAL tower with the transverse energy above 5 GeV. In general, L1 triggers are designed to be the least complicated because it needs to manage gigantic amount of events as the first gatekeeper of the data taking system. Due to the simple design of the photon finding algorithm, the energy calibration is not accurate as much as the offline reconstruction. So there is small inefficiency for photons right above 5 GeV. However, this inefficiency is negligible because the final photon selection of the analysis is p_{T} $>$ 60Ge and the L1_SingleEG5 is fully efficient.

One the events are selected by the L1 trigger, it is delevered to the high level trigger (*HLT*). The HLT menu for the 2011 heavy ion data taking contained Photon, Jet, Muon, High p_{T} track and UPC triggers. The photon triggers are composed of 4 single photon triggers and 5 double photon triggers at various thresholds. Since the input events for HLT are already skimmed by L1_SingleEG5 trigger, the HLT farm can tolerate more time to work on each event. The Photon HLT channel reconstructs the energy deposited in

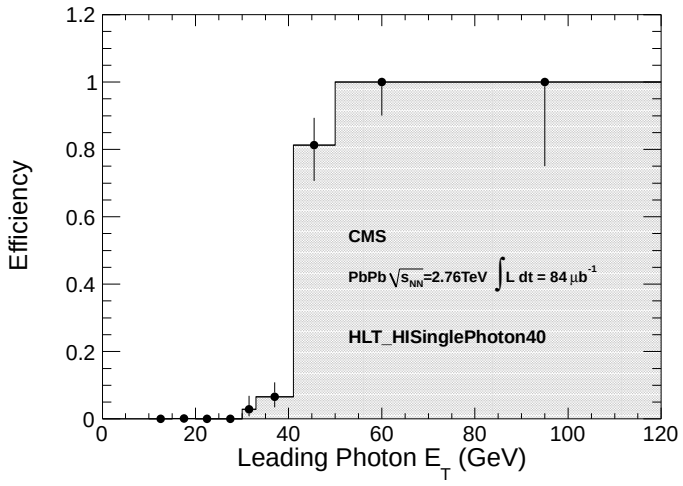

Figure 3.5: Trigger Efficiency turn-on curve of HLT_HISinglePhoton40 trigger. It is fully efficient from 50 GeV.

the ECAL crystals and find energy clusters made by electromagnetic showers, which is called **Superclusters**. Among several clustering algorithm, the CMS PbPb analyzers used the *island clustering algorithm* which can determine the photon energy within 2% resolution. This clustering algorithm will be be explained in detail in Sec. 5.2. The same clustering algorithm is used for HLT and offline analysis, except that the offline analysis used more sophisticate energy correction.

For this analysis, we used the HLT path named *HLT_HISinglePhoton40* which fires when there is at least one reconstructed supercluster whose transverse energy is above 40 GeV. The trigger rate was ~ 0.00024 per minimum bias event during the data taking. Figure 3.5 shows the data driven trigger turn on curve. The HLT_HISinglePhoton40 trigger efficiency is $> 80\%$ for SuperClusters with $p_T > 40$ GeV and fully efficient for $p_T > 50$ GeV.

3.4.2 Rejection of Anomalous Signals in ECAL

On January 2010, right after the LHC first began the 900GeV, 2.76TeV and 7TeV collisions, CMS collaboration was validating the detector performance. And the ECAL subgroup was very surprised by the result that the rate of high p_T photons were 100 times higher than expected. The reason was turned out to be the detector noise made by an unexpected reason. It was named **Anomalous ECAL signal** or **ECAL spike**.

The ECAL spikes are made by the interaction of a neutral hadrons and avalanche pho-

todiode which is attached to the end of ECAL crystals [69]. The avalanche photodiode is the signal amplifier of electromagnetic showers . However, when a low energy neutral particles directly hit the avalanche photodiode, the signals are anomalously amplified and pretends to be photon signals. The ECAL noise is an extremely serious problem for trigger system because the it can be misidentified as photon candidates in HLT system and cause photon trigger menu to be fired at O(10) times higher rate than designed. It could explode the trigger rates over the bandwidth and make the data taking situation very dangerous. Therefore, a spike removal filter in the trigger sequence was developed and implemented on the next few days after this problem was detected in the heavy ion run.

The judgement of noise was done by *swiss cross cut* which is defined as $(1 - E_4/E_1) < 0.95$, where E_1 is the highest energy crystal in the cluster and E_4 is the total energy of the four crystals right, left, top and bottom of the highest energy crystal [69]. Figure 3.6 shows the schematic performance of the spike cleaning.

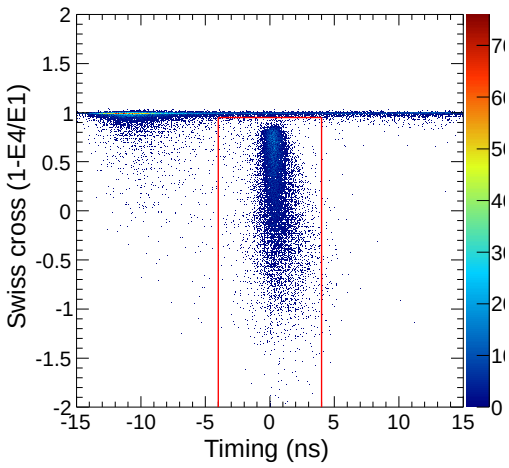

Figure 3.6: The swiss cross variable and ECAL reconstruction timing. The photon candidates inside the red box are used for analysis, and the others - called spikes - are rejected in both online and offline. In online, only the swiss cross variables are used for filter, and in offline the timing information is additionally used.

In the offline analysis, ECAL spike rejection was done by tighter cut $(1 - E_4/E_1) < 0.9$. Additionally used is the hit timing of the crystal which measured the travelling time of the electron showers arrive to the APD. Due to the high refractive index of crystal ($PbWO_4$ has n $\sim$ 2.2 for visible light wavelength), photons travel slower than other par-

ticles which are the source of spike. In addition, the drifts of electron showers in the crystal delays the timing. This signal arriving time called *Seed Timing* was required to be $|t| < 3$ ns. Figure 3.7 shows the distribution of reconstruction timing of the ECAL supercluster seed (p_{T} >60 GeV/c) for various centrality intervals (centrality is defined later in Sec. 5.1). Normal superclusters are distributed within ± 3ns, but the spikes are linearly distributed. By utilizing the sideband of ± 2 - 4ns, the fraction of underlying spikes within ± 3ns is interpolated in the shaded area. The remnants of spikes are estimated to be less than 1%.

3.4.3 Rejection of Anomalous Signals in HCAL

Also In HCAL, there were considerable amounts of anomalous signals that pretends to be jets. HCAL in CMS uses hybrid photo-diodes (HPDs) to amplify the scintillation lights. It is understood that the anomalous signals resulted from the HPD noise threshold which was tuned for proton+proton collision events. HCAL was being run in different mode (*Non-Zero Suppression mode*) from default proton+proton runs [67]. More about the HCAL noise and its cleaning procedures can be found in Ref. [70].

The number of events removed by various cuts described so far were summarized in Table 3.1.

Table 3.1: The effects of various cuts on the 150 μb^{-1} data sample. In the third column, the % values are with respect to the line above and in the fourth column they are with respect to the skimmed sample. The cuts are applied in sequence.

Cut	events	% of previous	% out of triggered events
HLT_HIPhoton40 trigger	260758	100.00	
Offline collision event selection	252576	96.86	96.86
HCAL cleaning	252317	99.90	96.76
Isolated photon candidate $p_{\mathrm{T}} > 60$ GeV/c	2974	1.18	1.14

3.5 Data Taking of Proton-Proton Collisions at $\sqrt{s}$ =2.76TeV

The pp collision data at the same centre-of-mass energy were used as the reference data for the comparison to the PbPb results. The $\gamma-$jet scatterings of pp collisions are made in vacuum. So, if the kinematic characteristics are different between (pp $\rightarrow$ $\gamma-$jet) and (PbPb $\rightarrow$ $\gamma-$jet), it can be attributed to the presence of hot and dense medium.

The pp collision experiment at the same center-of-mass energy ($\sqrt{s}$ =2.76 TeV) had been conducted from Feb. 11th, 2013 to Feb. 13th, 2013. CMS recorded total luminosity of 5.4 pb^{-1} out of 5.5pb^{-1} delivered from the LHC. The trigger strategy was almost identical to that used in PbPb data taking periods, except that the photon reconstruction used Hybrid clustering algorithm [71] rather than the island algorithm. A trigger path named **HLT_PAPhoton40_NoCaloIdVL_v1** was used for this analysis because it was un-prescaled and fully efficient for the photons with $p_{\mathrm{T}} > 60$GeV/c. For the rejection of ECAL and HCAL noises and non-collisional events, the same methods used in PbPb data taking were applied

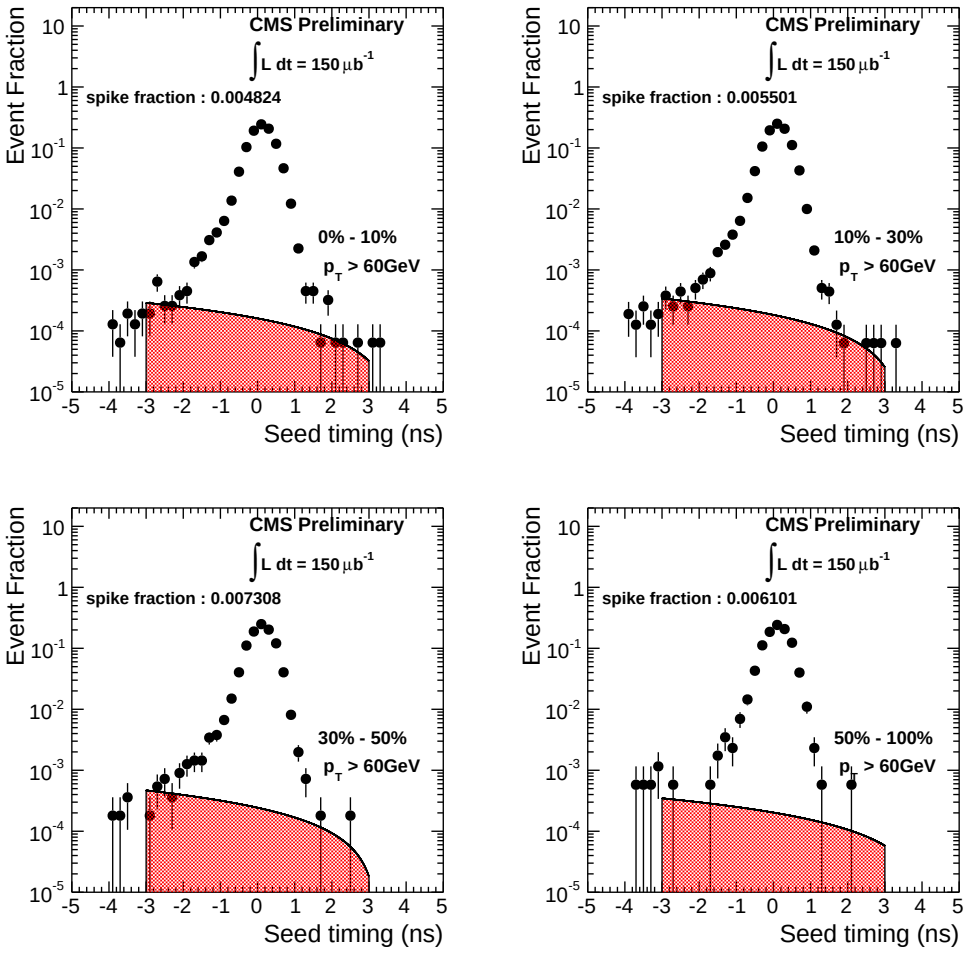

Figure 3.7: Distribution of signal arriving timing at APDs of seed crystals of supercluster (p_T >60 GeV/c) in 4 collision centrality intervals (Centrality is explained later in Sec. 5.1). The shed area is the remnant of spikes after cleaning, which are less than 1%.

4 Monte Carlo Simulation

Monte Carlo (or **MC**) simulation tools were used to understand how the detector responds to the particles produced by collision events. It is used in many analysis steps including energy correction of photons and jets, determination of various reconstruction efficiency and fake rate, and the validation of overall analysis sequence. Therefore, it is worthy to review the usage of MC simulated events sbefore moving forward to the actual analysis.

The simulation of events can be divided into two steps. First is the *particle generation step* which computes the multiplicity, species, energy and direction of particles expected to be produced in collisions. PYTHIA [72] was used to generate the high p_{T} photon events and HYDJET [73] was used to generate MinBias heavy ion collision events. The HYDJET events are later overlaid to PYTHIA events one-to-one in order to make a realistic heavy ion background environment.

Second step (*detector simulation*) is the technical simulation of the detector's responses by *GEANT4* [65, 74]. It simulates the interaction between detector materials and the particles prepared in the first step. Detector materials include the Silicon (Trackers), $PbWO_4$ crystals (ECAL), copper layers(HCAL) and steel observers (HCAL).

The detector simulation step takes much longer time than the particle generation step because it uses the numerical simulation method. For economical use of computing resources, the PYTHIA events are filtered by the presence of high p_{T} photons before entering to the detector simulation step.

In this chapter, only the **particle generation** step will be discussed. More general information about *GEANT4* simulation can be found in Ref [65, 74].

4.1 PYTHIA - Hard Scattering Simulation Software

Simulated $\gamma-$jet events were generated by PYTHIA [72] that is the software widely used for high energy physics researches. It can produce many built-in hard scatterings from p+p, p+e and e^++e^- collisions. The cross-sections of various scatterings are not sophis-

ticatedly calculated by Lagrangian from the scratch. Instead, the cross-section function is parametrized by several scaling behaviour inspired by either experiments or approximated calculation of pQCD [75]. So, we need to tune the parameters in PYTHIA in order to match the simulation with the given past experiments' data before using for analysis. One of major advantages of PYTHIA is that it can also generate jets using built-in parton shower pattern (or fragmentation of partons) based on scaling functions inspired by pQCD calculation.

In addition, The simulation of soft QCD dynamics makes the jets' kinematics more realistic. For example, it can simulate the underlying events - made by partons that did not participate in hard scattering - and secondary gluon radiation of partons. For this analysis, PYTHIA version 6.422 was used. And a modification in the parton distribution function was applied to take into account the isospin of the colliding nuclei [73], because a lead ion is composed of 82 protons and 126 neutrons.

4.2 Selection of Isolated Photon Events in PYTHIA

4.2.1 $\gamma-$jet Event Simulation

PYTHIA provides multiple channels of high p_{T} photon production, and they can be classified in 4 divisions as below.

(i) quark-gluon Compton scattering $q + g \rightarrow g + q$

(ii) quark-anti-quark annihilation $q + q \rightarrow g + g$

(iii) photons radiated from high p_{T} partons made by any QCD hard scattering

(iv) Photons decayed from neutral mesons (For example, π^0, η and ω)

Processes (i), (ii), and (iii) are produced at the lowest order in the electromagnetic and strong coupling constants. In terms of QCD calculation, (i) and (ii) are called *LO photons* (leading order), those from (iii) are referred to as *fragmentation photons* and (iv) are called *decay photons*. We are interested in (i) - (iii), yet (iv) is considered as background. One obstacle is that the cross section of the backgrounds is by far larger than that of signals as shown in Fig. 4.1. The analysis can not be accomplished in such a low signal/background ratio. This problem can be resolved by requiring the photon candidates to be isolated from hadrons. The necessity of the isolation criteria was already discussed in Fig. 2.5.

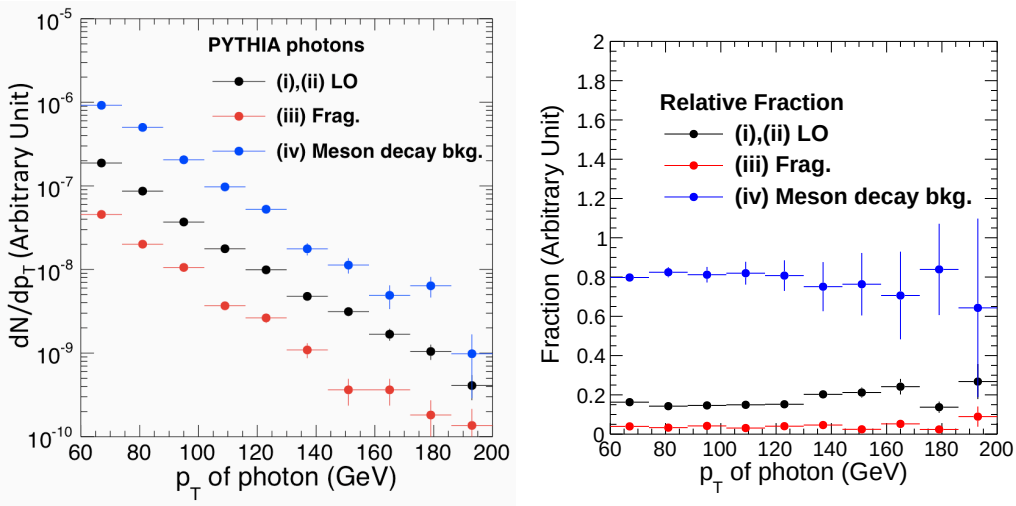

Figure 4.1: (Left) Spectra of photons in p+p collisions at 2.76TeV simulated by PYTHIA. (Right) The relative fraction of each sources. The background photons decayed from neutral mesons (vi) overwhelm the signals. The isolation criteria were introduced to enhance the signal ratio, to be shown in Fig 4.3 and Fig. 4.4

4.2.2 Isolation Criteria

In order to decide whether a given photon candidate is isolated or not, a cone with radius of $\Delta R = 0.4$ ($\Delta R = \sqrt{(\Delta\eta)^2 + (\Delta\phi)^2}$) around the photon in the $\eta \times \phi$ coordinate, which is called the *isolation cone*. The *isolation energy* can be defined as the sum of the transverse energy of particles inside this cone. In the MC generator, we call this value *GenIso*. In experiments, we reconstruct this value by adding the transverse energy deposited in ECAL, HCAL, and the transverse momentum in tracker. The contribution from underlying particles are subtracted using a correction method which will be described in Sec. 5.2.3.2. This reconstructed variable is called *SumIso*. In principle, if the detector is 100% ideal, the reconstructed isolation energy (SumIso) should be always same to the generator level isolation energy (GevIso). But they are smeared by the limited detector efficiency and resolution. Figure 4.2 shows the correlation of *SumIso* and *GenIso* of photons in PYTHIA samples. In this analysis, *SumIso* < 1 GeV cut was used to choose good photon candidates.

The main reason of using the tight threshold (1 GeV) - despite the low efficiency - is its high signal purity. As we use a higher purity of photon candidates, the amount of background subtraction in Sec 6.3 is reduced. Therefore, we can decrease the systematic

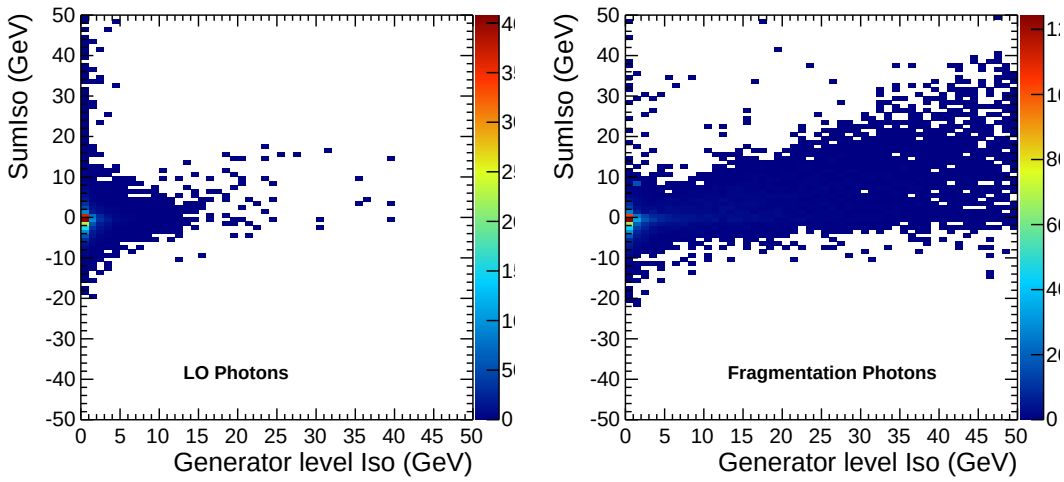

Figure 4.2: Correlation between *GenIso* (generator level isolation energy) and *SumIso* (reconstruction level isolation energy) in the cone around prompt photon (Left) and fragmentation photon (Right). Two variables lose their correlation below 5GeV/c cut due to the limited energy resolution.

uncertainty induced in this step. The 1 GeV cut for *SumIso* was chosen to control the purity to be within 73 - 84% (to be shown later in Fig. 6.2) and to have the efficiency within 65% - 80% (to be shown later in Fig. 6.16).

As shown in Fig 4.3 and Fig. 4.4 (compared to Fig. 4.1), the population of background photons was dramatically suppressed by the ***SumIso*** cut. Additionally, the fraction of fragmentation photons was also reduced. We do not expect that the PYTHIA simulation provides the exact number of photon backgrounds less than 10% level accuracy. Therefore, the precise measurement of photon purity will be obtained using data-driven methods that will be discussed in Sec. 6

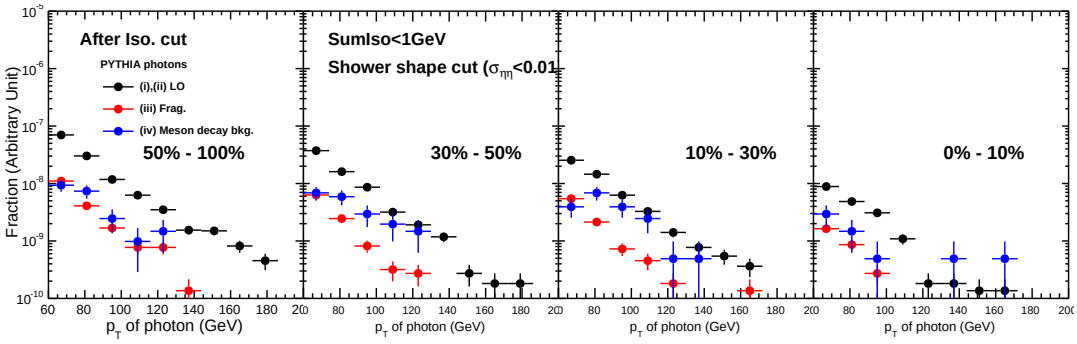

Figure 4.3: Expected spectra of high p_{T} photons in heavy ion collision simulation. The percentile numbers in the figures represents the centrality, the size of the underlying events (See Sec. 5.1). The fraction of direct photon has been clearly enhanced compared to Fig. 4.1. The background fraction from PYTHIA is not credible for this anlaysis, so the accurate signal purity will be calculated using a data-driven method in Sec. 6

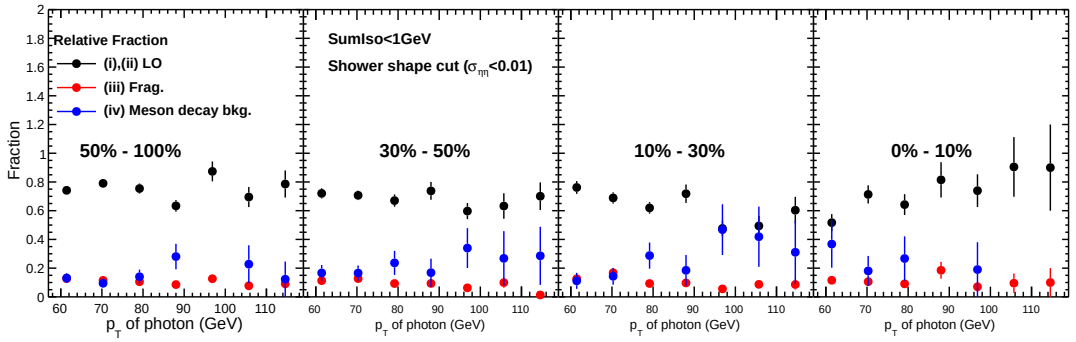

Figure 4.4: Relative fraction of photon sources in Fig. 4.3. The percentile numbers in the figures represents the centrality, the size of the underlying events (See Sec. 5.1). The fraction of direct photon has been clearly enhanced compared to Fig. 4.1. The background fraction from PYTHIA is not credible for this anlaysis, so the accurate signal purity will be calculated using a data-driven method in Sec. 6

4.2.3 High p_{T} Photon Filter

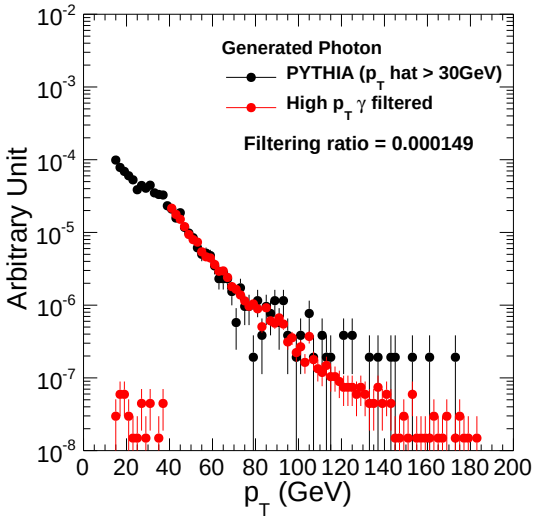

Figure 4.5: Performance of the high p_{T} photon filter installed in PYTHIA generator. Transverse momentum spectra of prompt photons in PYTHIA samples are compared before (black) and after (red) the filter ($p_{\mathrm{T}} > 40$GeV/c). Only the filtered events goes into the full simulation sequence and saves significant amount of computing resource and time.

The high p_{T}fragmentation photons are much rarer compared to the prompt photons. To save computing power and time used for full detector simulation an extension plug-in of PYTHIA was developed, which requires the photon to have at least $p_{\mathrm{T}}>40$ GeV/c. This saves the simulation time by factor of ∼100 . Figure 4.5 shows the performance of this software.

4.2.4 Generation of Background Photons : Di–jet samples

Di–Jet samples are used for the study of background photons such as $\pi^0 or \eta \rightarrow g,g$ channels. When a neutral meson have very high p_{T} and its decayed photon pair hit the ECAL crystals, the two electromagnetic showers merge into a single cluster and pretends a single direct photon. The simulation of di–jet samples were produced to study the background rejection strategy.

In terms of PYTHIA parameters, $q+q' \rightarrow q+q'$, $q+\overline{q} \rightarrow q'+\overline{q}'$, $q+\overline{q} \rightarrow g+g$, $q+g \rightarrow q+g$, $g+g \rightarrow q+\overline{q}$, and $g+g \rightarrow g+g$ channels were used, which are identical to the ones used in fragmentation photon generation.

In order to select events which may create a fake photon signals, a similar trick in 4.2.3 was used. The events were selected only if they have at least one high p_{T} photon above 20 GeV/c which were decayed from neutral hadrons such as π and η.

4.3 HYDJET - Heavy Ion Event Simulator

PYTHIA is not sufficient to support this $\gamma-$jet analysis for the reason that it simulates proton-proton (or neutron) collision which is only a sub-event of a heavy ion collision. The number of nucleons participating in of Pb^{208} ion collision can reaches upto 416 (twice the number of nucleons). A $\gamma-$jet event is rarely produced from the scattering of a nucleon-nucleon pair among these pool of participant nucleons. In order to make similar environment with real experiments, the simulation of the other sub-collisions needs to be done and overlaid on PYTHIA $\gamma-$jet scattering. A naive method would be to generate hundreds of p+p, p+n and n+n MinBias events and merge the single event. However, the heavy ion collisions are more complicated than that because the particles are emerged from the thermalized medium - possibly Quark Gluon Plasma - so the particles' kinematics have strong correlation with each other [76] [77]. It is necessary to use a separate MC event generator which can reproduce the collective behaviour of particles in PbPb MinBias collision.

HYDJET [73] (HYDrodynamics plus JETs) is a heavy ion specialized event generator which can suitably generate the multiplicity and flow effect of particles. For this analysis, HYDJET was tuned to fit the results from CMS and ALICE heavy ion experiments [78]. Fig 4.6 shows the consistency between the tuned HYDJET and real measurement at $\sqrt{s_{NN}} = 2.76$TeV in terms of charged particle multiplicities and momentum spectra.

Prepared with PYTHIA and HYDJET events, the *signal embedding* technique was used to mix both events. By adding two collection of particles generated in PYTHIA $\gamma-$jet events and those in MinBias HYDJET events, we can mock the $\gamma-$jet signals produced on top of PbPb underlying events. From now on, the PYTHIA signals embedded in HYDJET will be noted as **PYTHIA+HYDJET**. Statistics of simulated MC samples and their cross sections computed by PYTHIA are summarized in the Table 4.1.

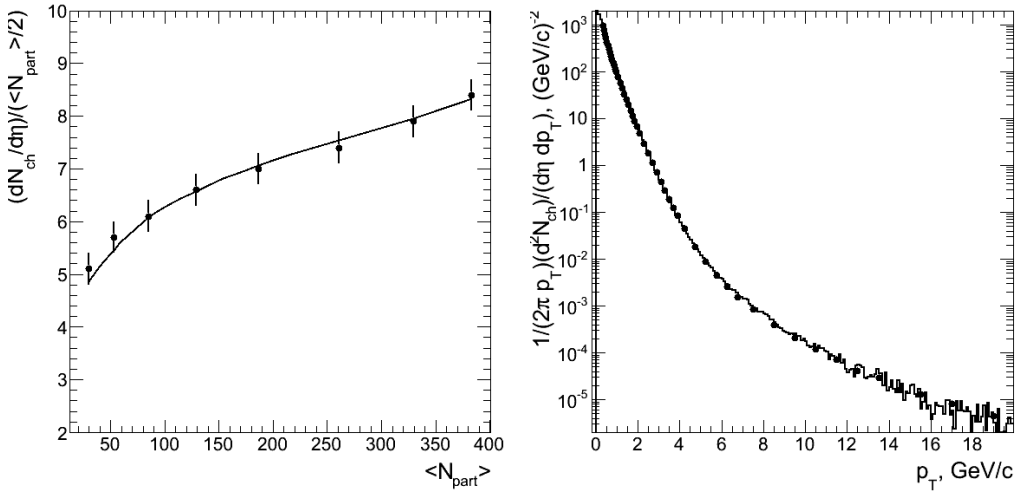

Figure 4.6: HYDJET, a heavy ion collision simulator, (in version 1.8) was tuned to match with the MinBias PbPb collision data at $\sqrt{s_{NN}} = 2.76$TeV measured at CERN [78]. These two plots show the comparison of HYDJET and real data obtained in ALICE experiment. Left is the centrality dependence of multiplicity density in the mid-rapidity. Right shows the spectrum of charged particles in the top 5% central collisions. The collisional centrality and N_{part} will be explained in Sec. 5.1.1.

sample	$\hat{p}_{\text{T}}$	Number of events	cross section (mb)
Photon Jet + PbPb data	30 GeV/c	80k	1.59×10^{-6}
	50 GeV/c	80k	7.67×10^{-7}
	80 GeV/c	70k	1.72×10^{-7}
EM-enriched jet + HYDJET	50 GeV/c	40k	1.587×10^{-4}
	80 GeV/c	50k	1.76×10^{-5}
$Z \rightarrow ee$ + HYDJET	No limit	30k	
$W \rightarrow e\nu$ + HYDJET	No limit	30k	

Table 4.1: PYTHIA events simulated and embedded in HYDJET samples

5 Reconstruction of Events

Once collision events are accepted by the data acquisition system, the signals of detector are digitized and then recorded in a compressed data format of digital signals which is called *RAW* format. In order to visualize detected particles, the data needs to be transformed into the higher level objects which contain physically meaningful values such as charge, momentum and species (jet, photon, lepton and so on). The comprehensive chain of this translation procedure is called *Reconstruction*.

Usually reconstruction process is done several times because the calibration and correction factors are being updated. For this analysis, the first reconstruction dataset - *Prompt Reco* - was used. It was reconstructed by the computing resources close to the CMS detector (P5 at CERN), so the files were accessible only 1-2 days after the collisions. In this section the reconstruction of critical event properties - centrality and vertex- will be reviewed. Then detailed reconstruction method of individual physical objects - photons and jet - will be explained.

5.1 Centrality Determination in CMS

One of the biggest differences of the heavy ion collisions from proton-proton (or electron- electron, electron-proton collisions) ones is that the characteristics of events highly depends on the impact parameter. For example, the multiplicity of the particle production in the head-on collisions at 2.76TeV reaches up to 10,000, whereas in the most peripheral collisions, it is only O(100). In heavy ion experiments, the “head-on"ness of collisions is called *centrality*. When the centrality is higher the size of the produced medium is bigger, so the feature of Quark Gluon Plasma would be more evident.

5.1.1 Glauber Model, N_{part} and N_{coll}

The *Glauber model* is a phenomenological model that is used to understand the collisional geometry of nuclei in heavy ion experiments [48]. It determines the size of collision and probability of hard scattering and its dependence on the impact parameter. There are assumptions of this model and the most important ones are following.

1. A nucleus is a composite of protons and neutrons in ball shape, which are very hard so they do not overlap each other. The radius of a ball is same with a proton (around 1.6 fm) which is calculated based on the p-p hadronic cross section. Therefore, the ratio of the inelastic cross-section of PbPb to that of pp is a fixed number if the collision energies are same.

2. The protons and neutrons are distributed according to Woods-Saxon Potential [79].

3. A collision of two nuclei can be understood as the sum of sub-collisions among consituent nucleons. Such sub-collisions can happen only when two nucleons overlap on the transverse plane relative to beam axis. The nucleons which did not overlapped each other just keep going along the beam line without strong interaction. They are called *spectator nucleons*.

4. Even after a constituent nucleon made one collision, it keeps going straight and possibly makes another sub-collisions with other nucleons.

From this picture, two values related to the impact parameter can be defined. One is the number of participants ($\mathbf{N_{part}}$) that counts the nucleons which contribute at least one sub-collision. This number is particularly important in terms of the size of the medium produced by the collision. It is experimentally known that the particle multiplicity linearly scales by N_{part} for both proton-nucleus [80] and nucleus-nucleus collisions [81]. The other one is the number of binary collisions ($\mathbf{N_{coll}}$) that counts the sub-collisions of nucleon-nucleon pairs. As the assumption mentioned above, a nucleon constituent can make multiple collisions if there are multiple nucleons overlapping on the transverse plane. This value is an essential parameter for the production rate of high p_{T} particles, because the probability of making an hard scattering scales by N_{coll} . For example, N_{coll} is about 1500 for the top 10% central Pb+Pb collision. So, in this interval, the probability to produce a high p_{T} photons is 1500 times more than that of a p+p inelastic collision [46].

Fig. 5.1 illustrates the N_{part} and N_{coll} computation for an AuAu collision (Right) and a simplified toy model of nuclei in 2-dimension (Left)

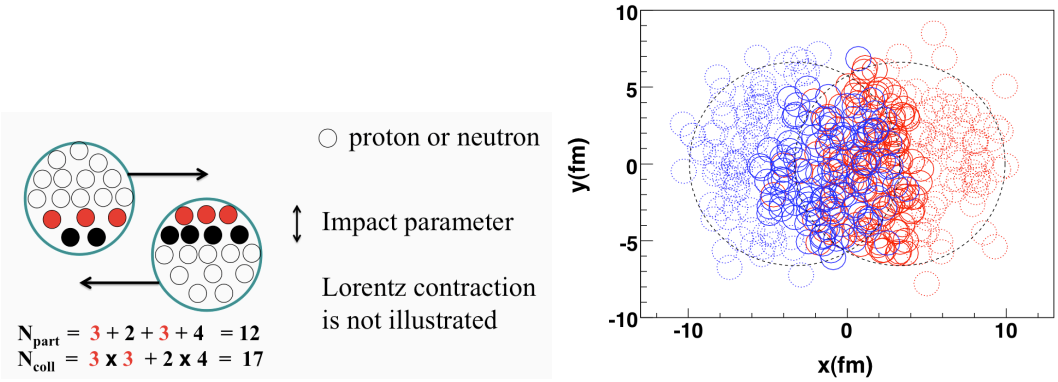

Figure 5.1: (Left) Illustration of counting N_{part} and N_{coll} of an heavy ion collision. For easier visualization the nucleons are distributed in 2-dimension plane. Obviously in reality, they are distributed in 3-dimension space. (Right) Toy MC simulation of Au+Au collision using PHOBOS Glauber program [82].

5.1.2 Reconstruction of Centrality in CMS

Centrality was determined using the sum of transverse energy deposited in the forward hadronic calorimenter (HF) which covers $2.9 < |\eta| < 5.2$ which are close to the beam axis [68]. The distribution of the energy was used to divide the event samples into 40 bins, each representing 2.5% of the total PbPb inelastic cross section. The determination of the boundaries for these bins relies on the collision event selection efficiency, which involves trigger, vertex reconstruction, contamination of the sample by the ultra-peripheral electromagnetic collisions as well as other requirements mentioned in Sec. 3.3.2. From the simulation study of collision, the overall efficiency of the event selection was estimated to be 98% and the contamination by the ultra peripheral collisions is estimated to be 1%, resulting in a correction factor of 1% in the selected event cross section with uncertainty of 2%.

In order to overcome the small statistics of $\gamma-$jet events in this analysis, fine-grained bins were combined into 4 coarser bins which are 0%-10%, 10%-30%, 30%-50% and 50%-100%. The percentiles corresponds to the fraction out of the total hadronic cross-section and smaller number represents more central collisions. So, the 0%-10% (Most

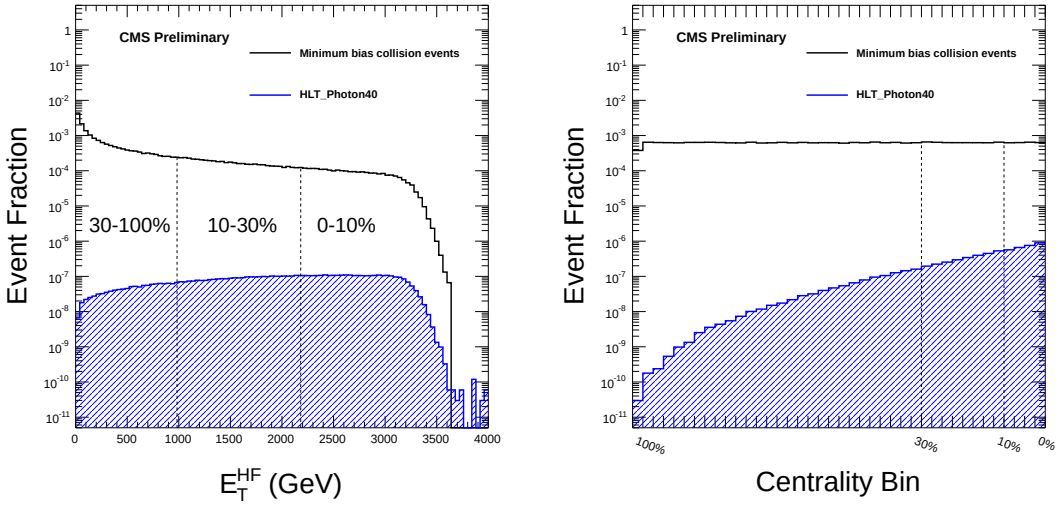

Figure 5.2: All histograms show the fraction of the total number of triggered minimum bias events. Left: Distribution of event fraction versus the total HF energy used to determine centrality of the PbPb interactions included in this analysis. The three regions correspond to the centrality ranges described in the text. The open (black) histogram is for minimum bias events while the cross-hatched (blue) one is for events passing the HLT photon trigger (see text for details). Right: Distribution of fraction of events in the 40 centrality bins for minimum bias (black open histogram) and HLT photon triggered (blue cross-hatched histogram) events. The percentage cross section labels run from 100% for the most peripheral to 0% for the most central events.

central collision) bin has the smallest impact parameters and 50%-100% (Most peripheral collisions) bin has the largest ones.

The centrality determination accodring to the distribution of the HF energy is shown in the left-hand side of Fig. 5.2. The corresponding number of participants (N_{part}) values for a given fraction of events is determined from the Glauber calculation [48].

The right-hand side figure of Fig. 5.2 shows the fraction of the events falling in each of the 40 centrality bins. Fractions of the total number of minimum bias events in the sample are shown for both minimum bias (black open histogram) and HLT photon triggered (blue cross-hatched histogram) events. From these two distributions, it can be seen that the HLT photons of roughly 40 GeV/c required to pass the on-line trigger are more common in central events, as expected by its larger N_{coll}.

5.2 Reconstruction of Photons

An high p_{T}photon makes an electromagnetic shower on multiple on multiple ECAL crystals (10-100). Therefore, the reconstruction of photon begins by finding a conglomerate of energy deposits in crystals. This object is called a *supercluster* and the algorithm to find superclsuters will be introduced in Sec. 5.2.1. Due to the high multiplicity of underlying events in PbPb collisions, a handful of hadrons can pile up on the electromagnetic shower made by a high p_{T} photon. The clustering algorithm can not avoid to pick up additional energy made by pile-up hadrons such as pions and kaons. Therefore, an additional energy correction is applied to remove this contamination. The correction procedure of the reconstructed photon candidate is detailed in Sec. 5.2.2.

Once the superclusters are reconstructed, we then examine where it is a direct photon or a neutral meson by the isolation criteria. Since the neutral mesons are mostly produced inside jets, they are not isolated. To quantitatively determine the isolation level of photons, Silicon tracker, ECAL and HCAL are used to measure the energy in a cone around the photon. (Sec. 5.2.3.2).

5.2.1 Island Clustering Algorithm

5.2.2 Photon Energy Calibration

The first step of photon reconstruction is to convert the digital signals in ECAL crystals into GeV unit, which are called *Rechits* (reconstructed hits). The energy calibration of crystals was done by the lasers installed inside the detector. Good linear behaviour of the crystal readout guarantees less than 1% of energy resolution for high p_{T} photons [66]. In CMS, a photon (an electron) shower deposits 94% of its energy on the 3×3 crystals, and 97% in 5×5 crystals. Such a group of energetic Rechits is called *superclsuter*.

Among many photon cluster finding algorithms, the *Island clustering algorithm* was used for this analysis. As the first step, clustering algorithm searches for the *seeds* which are defined as the Rechits with transverse energy above a threshold $E_T > 0.5$ GeV. Initiated from a seed position, adjacent crystals are examined whether they will be merged to the cluster or not. Scanning first in the ϕ direction and then in the η direction, crystals are added to the cluster until either a rise in energy or a crystal that has already been assigned to a different cluster (or that has not been hit) is encountered. Fig. 5.3 shows the schematic diagram of the algorithm stated above. Those clusters are called *basic-clusters*, which are the intermediate step just before becoming superclusters.

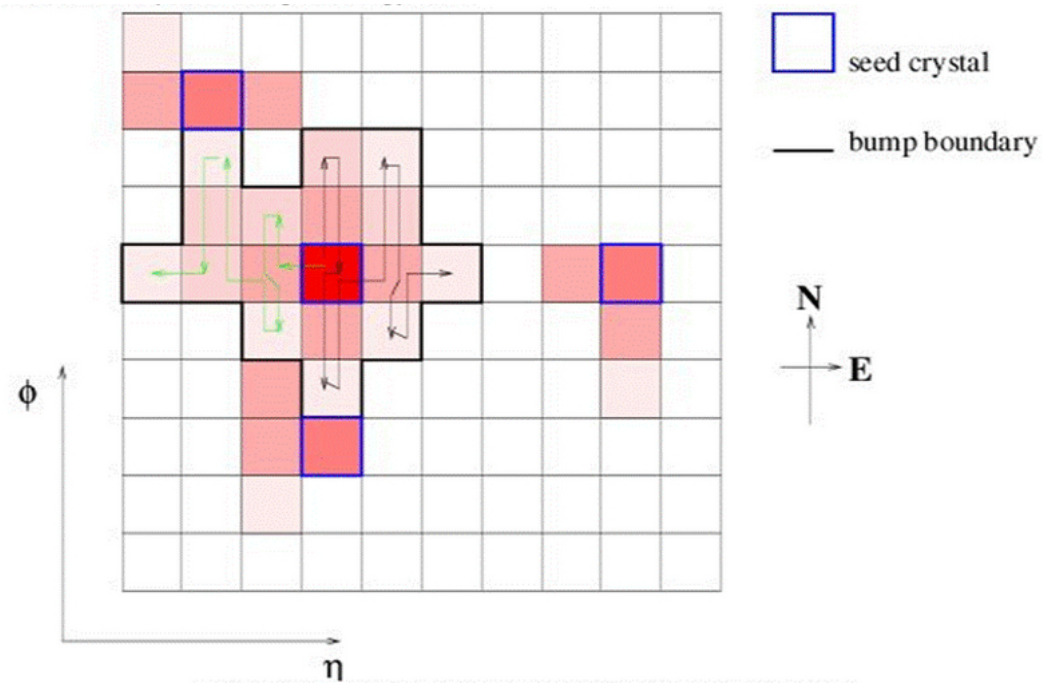

Figure 5.3: Demonstration of the Island' clustering algorithm in the partial map of CMS ECAL crystals.

In the second step, the basic-clusters are clustered into superclusters. The procedure is seeded by searching for the most energetic basic-cluster and then collecting all the other nearby clusters which are not yet been used in a narrow η-window ($\Delta\eta = 0.07$), and a much wider ϕ-window ($\Delta\phi = 0.8$). The position of supercluster is the energy-weighted center of mass of the constitute rechits. The position uncertainty was calculated to be very small, less then 0.006 (=1σ), from the study of MC simulated events (Sec. 4). if a supercluster has transverse energy above 10GeV it is recognized as a loose photon candidate. For this thesis, only the photon candidates in the barrel region ($|\eta| < 1.44$) and $p_T > 60$ GeV are selected, by means of their good energy resolution and signal/background rate.

To the first order approximation, calculation of reconstructed energy of photons can be done by adding up the energies of constitute rechits which is called *raw energy*. But, if multiple EM shower elements are merged in a same crystal, the total energy is underestimated. Therefore, an energy correction must be applied depending on the crystal shape.

We first classifies the photons by whether it was converted into electron-positron pairs before hitting the ECAL. The presence of materials in front of the ECAL - Silicon

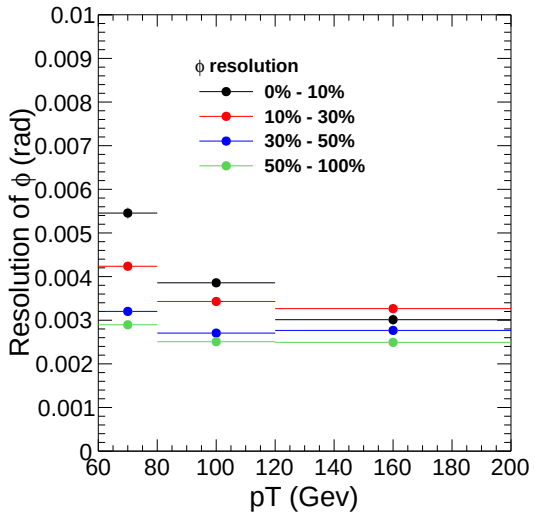

Figure 5.4: Resolution of azimuthal angle measurement of reconstructed photons. The uncertainty is under 0.006. Higher p_{T} photons (or at lower centrality) tend to have better resolution.

detectors and the solenoid magnet - results in the conversion photons into electron-position pairs and Bremsstrahlung before touching the ECAL. In fact, CMS has relatively denser materials compared to other particle detectors, so the conversion probability is considerably high. About 30% of photons are converted. In this case, the energy reaching the calorimeter is more spread in ϕ due by the magnetic filed. Whether a supercluster had been converted was judged by the energy ratio variable $r9$, which is defined as the ratio of the energy in the 3×3 crystals around the supercluster seed (e_9) to the total energy e.

If $r9$ is greater than 0.94, the cluster is classified as an unconverted cluster. The correction of the unconverted clusters is done by multiplying a simple correction factor $f(\eta)$ which is a function of pseudorapidity. On the other hand, the correction of the converted clusters has two additional steps in order to consider the Bremsstrahlung photons radiated from electrons by magnetic filed. The first correction factor is f_{Brem} which is parametrized by the ratio of η and ϕ width of supercluster to account the spread of energy. The second correction by $f_{E_T\eta}(E_T,\eta)$ cleans up the remaining dependence on the cluster E_T and η.

The reconstructed primary vertex was used to correct the η and ϕ position of photon candidates. The resolution of the azimuthal angle of the reconstructed photons is shown in Fig. 5.4. Figures 5.5 and 5.6 show the energy scale as a function of the

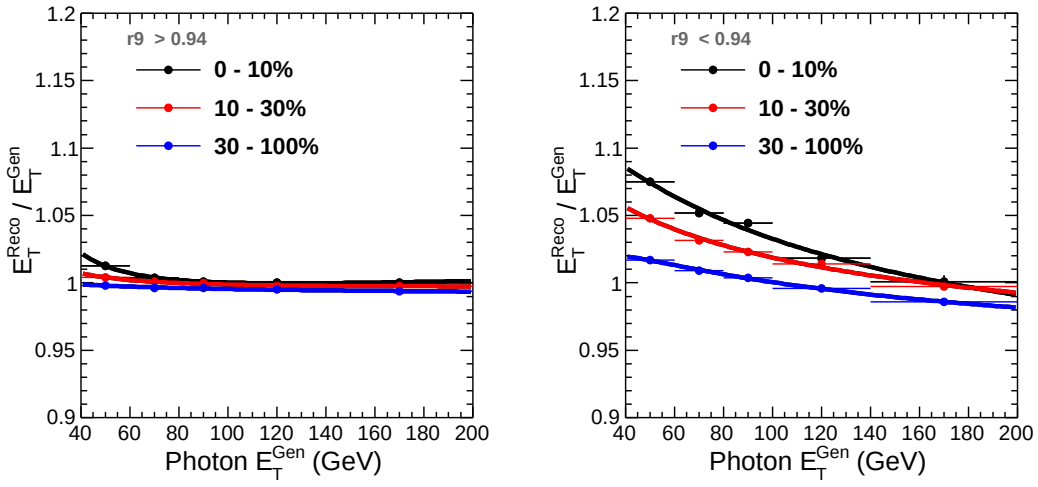

Figure 5.5: Energy scale of reconstructed photons shown for $r9 > 0.94$ (left) and $r9 < 0.94$ (right). MC photon-jet PYTHIA samples embedded in HYDJET were used.

event centrality and photon p_T obtained from PYTHIA+HYDJET simulation. Due to the large PbPb underlying event (UE), the ratio of p_T^{Reco}/p_T^{Gen} in simulated events is larger than 1 in central (high multiplicity) PbPb collisions. An additional energy correction is applied to remove the background contribution from the underlying PbPb event ("UE correction"). The correction factors (as a function of photon p_T and event centrality) are obtained from the inclusive isolated photons simulated by PYTHIA+HYDJET.

5.2.3 Photon Identification

Most of the reconstructed photon candidates obtained from the supercluster algorithms are dominated by background photons which are high p_T π^0. Various photon isolation methods were developed and are introduced in this section. It was able to highly suppress the background photons and enhance the fraction of signals by limiting the energy activity around a photon isolation energy.

5.2.3.1 H/E

H/E ratio is defined as the fraction of energy deposited in HCAL to that in ECAL in a cone with radius $\Delta R = 0.15$ around a photon candidate. This variable is useful to reject high p_T hadrons especially charged hadrons because they deposit most of their energy to HCAL whereas photons deposit almost all energy to ECAL. In this analysis, the H/E

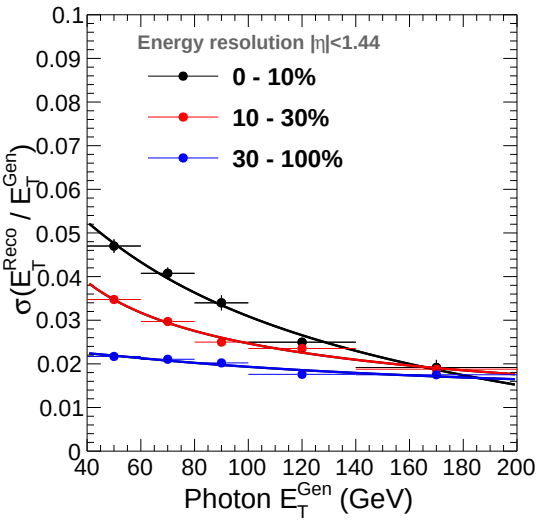

Figure 5.6: Energy resolution of reconstructed photons. MC photon-jet PYTHIA samples embedded in HYDJET were used.

ratio of the photon candidates is required to be smaller than 0.1. The distribution of H/E of photon candidates in data and MC samples are shown in Fig. 5.7. Four centrality bins were used to inspect the multiplicity dependence of this variable.

5.2.3.2 Isolation Energy

Still skimming the superclusters by H/E cut, the majority of the background photons are neutral mesons (π^0, etc). Since these are mostly radiated inside inside jets, it would be verified by bunch of particles around the photon candidates. Although it is mentioned that the particles in a jet are collinear in Sec. 2.1.1 it does not literally mean that they are exactly parallel. Its angular distance Δ R from the axis spans around 0.1 - 1. Three sub-detectors, ECAL, HCAL and tracker, are used to measure E_T (and p_{T} in case of tracker) inside the isolation cone whose radius may vary between 0.1 to 1. The isolation energy (ISO) measured in each component was defined as below,

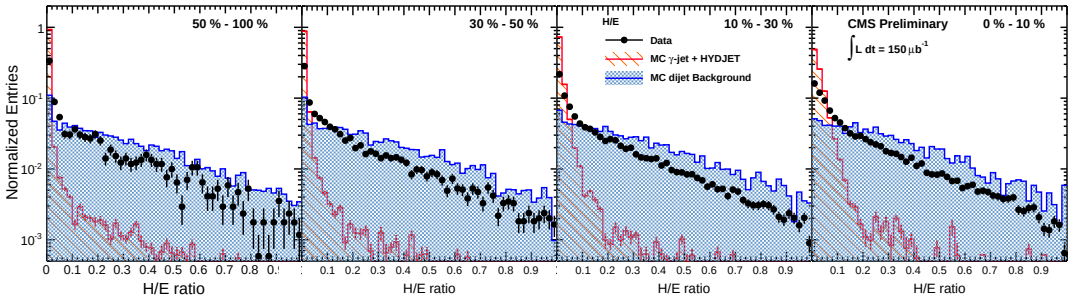

Figure 5.7: H/E distribution of MC signal and background in PbPb data and MC(PYTHIA+HYDJET). In pp, H/E is cut at 0.05, however in this analysis, 0.1 was used due to the energy fluctuation of underlying event.

$$\begin{aligned}
\text{(Uncorrected) ISO}_{\text{i}}^{\text{ECAL}} &= \sum_{\Delta R<i/10} E_T^{\text{ECAL}} - E_T^{\text{Candidate Itself}} \\
\text{(Uncorrected) ISO}_{\text{i}}^{\text{HCAL}} &= \sum_{\Delta R<i/10} E_T^{\text{HCAL}} \\
\text{(Uncorrected) ISO}_{\text{i}}^{\text{Track}} &= \sum_{\Delta R<i/10,\ \text{p}_\text{T}>2.0\text{GeV/c}} p_T^{\text{Track}}
\end{aligned} \tag{5.1}$$

Fig. 5.8 demonstrates the isolation energy in a cone.

The term (Uncorrected) in Eq. 5.1 is the advance notice for the further correction to be applied later. The reason for such correction can be found in the distribution of ISO variables in Fig. 5.9(ECAL), Fig. 5.10(HCAL) and Fig. 5.11 (Track). R=0.4 was used as the radius of isolation cone for these examples.

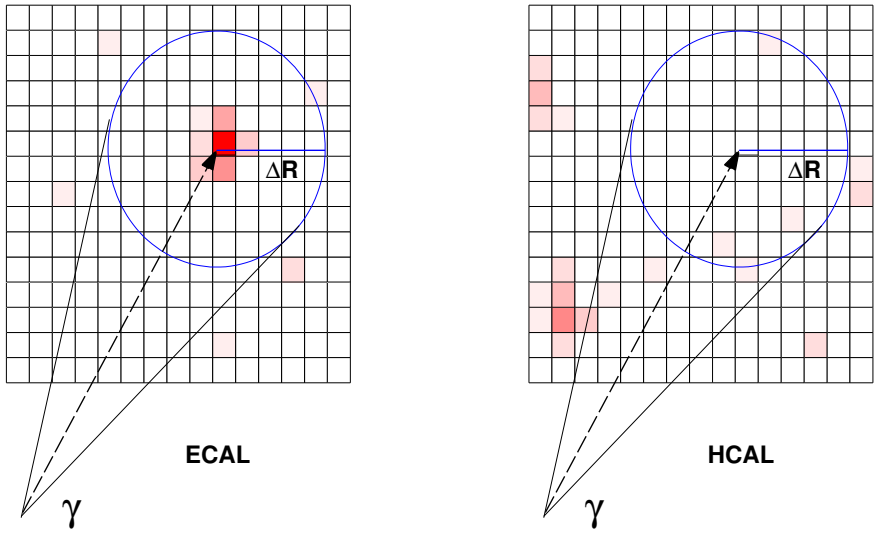

Figure 5.8: Illustration of isolation cone for ECAL(left) and HCAL(right) towers around a photon candidate.

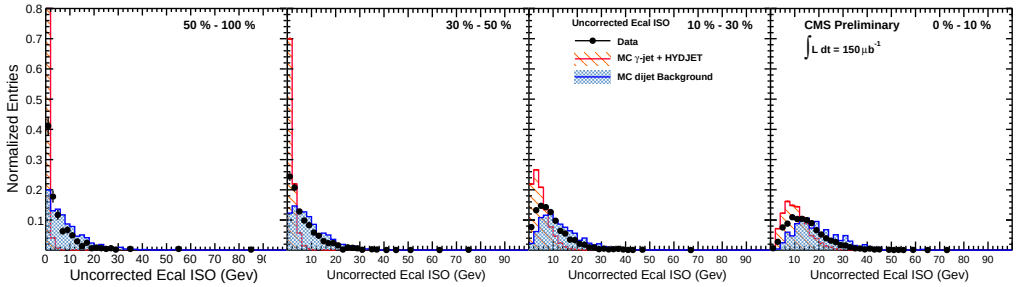

Figure 5.9: Uncorrected ECAL isolation variables of photons with $p_{\mathrm{T}} > 60$ GeV from PYTHIA photon-jet and PYTHIA dijet embedded in the HYDJET sample.

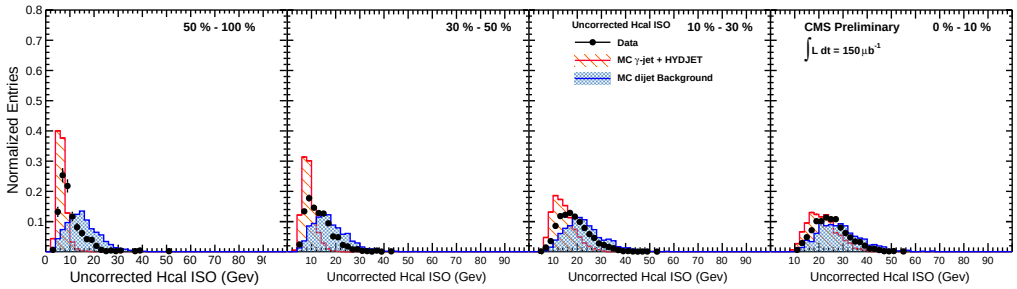

Figure 5.10: Uncorrected HCAL isolation variables of photons with $p_{\mathrm{T}} > 60$ GeV from PYTHIA photon-jet and PYTHIA dijet embedded in the HYDJET sample.

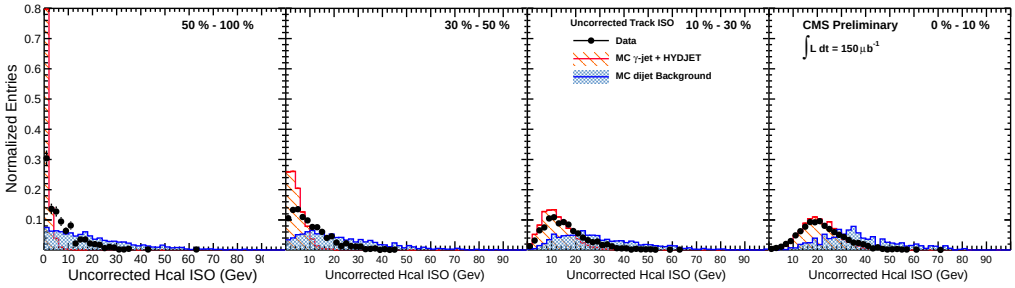

Figure 5.11: Uncorrected Track isolation variables of photons with $p_{\mathrm{T}} > 60\,\mathrm{GeV}$ PYTHIA photon-jet and PYTHIA dijet embedded in the HYDJET sample.

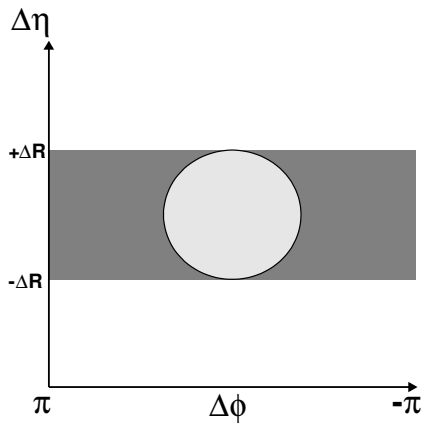

Figure 5.12: Schematic of the normalization scheme for background subtraction.

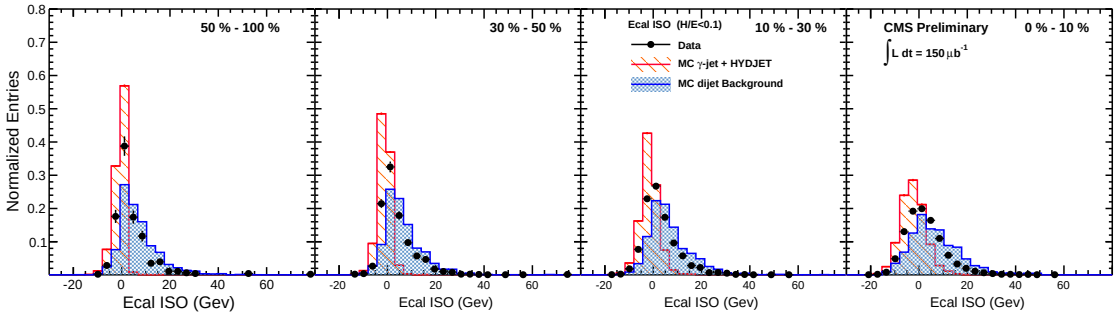

Figure 5.13: Corrected ECAL isolation variables of photons with $p_{\mathrm{T}} > 60$ GeV from PYTHIA $\gamma -$ jetand di–jet dijet embedded in the HYDJET.

The *uncorrected* isolation variables are highly dependent on the event centrality because of the high multiplicity of underlying events. Those particles are not correlated to the jet energy activity and randomly act. Therefore, the real isolation energy that we are interested is piled up on top of the overall pedestals. The pedestals was subtracted in the event-by-event manner. To estimate the contribution of the background in the isolation cone, we computed the average energy in a rectangular area of $\eta^{cand} \pm \Delta R$ in the η-direction and along 2π in ϕ. This energy density were multiplied by the area of the cone, as shown in Fig. 5.12, then it was subtracted to the uncorrected isolation energy. The corrected isolation variables are defined as below

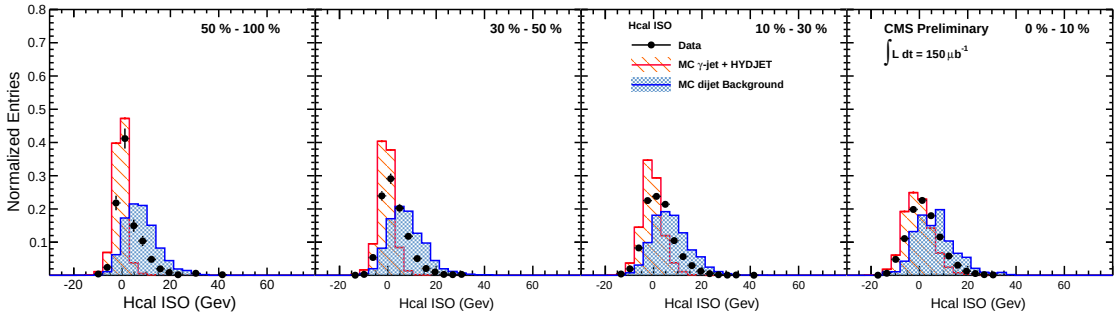

Figure 5.14: Corrected HCAL isolation variables of photons with $p_{\mathrm{T}} > 60$ GeV from PYTHIA $\gamma-$jetand di–jet dijet embedded in the HYDJET.

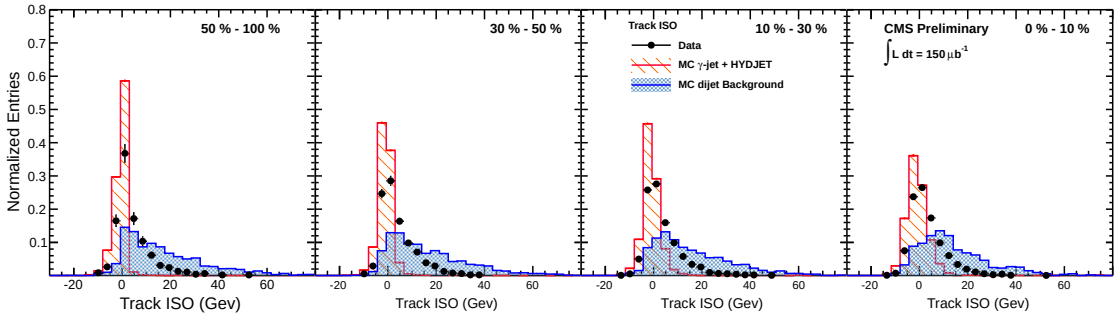

Figure 5.15: Corrected Track isolation variables of photons with $p_{\mathrm{T}} > 60$ GeV from PYTHIA $\gamma-$jetand di–jet dijet embedded in the HYDJET.

$$
\begin{aligned}
(\text{Corrected})\,\mathrm{ISO}_{\mathrm{i}}^{\mathrm{ECAL}} &= (\text{Uncorrected})\,\mathrm{ISO}_{\mathrm{i}}^{\mathrm{ECAL}} - (\text{Bkg})\,\mathrm{ISO}_{\mathrm{i}}^{\mathrm{ECAL}} \\
(\text{Corrected})\,\mathrm{ISO}_{\mathrm{i}}^{\mathrm{HCAL}} &= (\text{Uncorrected})\,\mathrm{ISO}_{\mathrm{i}}^{\mathrm{HCAL}} - (\text{Bkg})\,\mathrm{ISO}_{\mathrm{i}}^{\mathrm{HCAL}} \\
(\text{Corrected})\,\mathrm{ISO}_{\mathrm{i}}^{\mathrm{Track}} &= (\text{Uncorrected})\,\mathrm{ISO}_{\mathrm{i}}^{\mathrm{Track}} - (\text{Bkg})\,\mathrm{ISO}_{\mathrm{i}}^{\mathrm{Track}},
\end{aligned}
\tag{5.2}
$$

where (Bkg) ISO is the pedestal energy described above.

The isolation variables after background subtraction have a much less centrality dependence as shown in Fig. 5.13 (Ecal), Fig. 5.14 and Fig. 5.15. Additionally, the background subtracted isolation variables have better separation power than the uncorrected variables. From now on, the isolation energy refers the corrected value unless it is specified.

As previously stated in Sec. 4.2.2, the sum of ECAL, HCAL and Track isolation energy in the cone of R=0.4 were used as the isolation criteria.

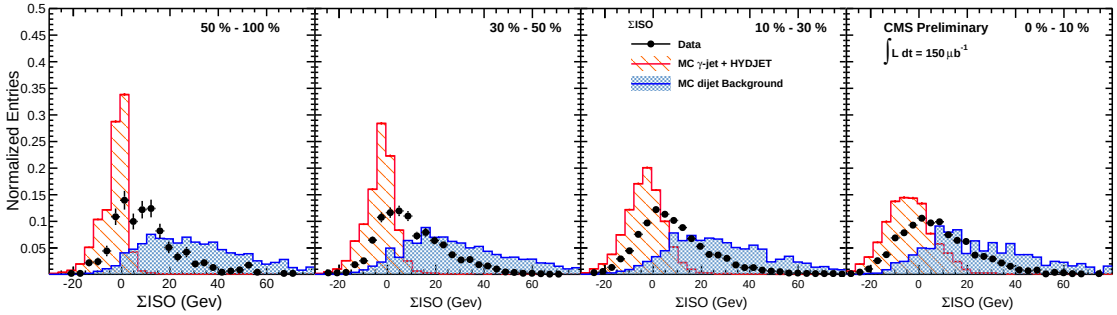

Figure 5.16: Corrected *SumIso* isolation variables of photons with $p_{\mathrm{T}} > 60$ GeV from PYTHIA $\gamma -$ jetand di–jet dijet embedded in the HYDJET.

$$\mathrm{SumIso} = \mathrm{ISO}^{\mathrm{ECAL}} + \mathrm{ISO}^{\mathrm{HCAL}} + \mathrm{ISO}^{\mathrm{Track}} \tag{5.3}$$

The efficiency of photons to pass this cut as a function of the isolation level is shown in Fig. 5.17. The distribution of SumIso from MC simulation is shown in Fig. 5.16. In this analysis, SumIso $<$ 1 GeV was used.

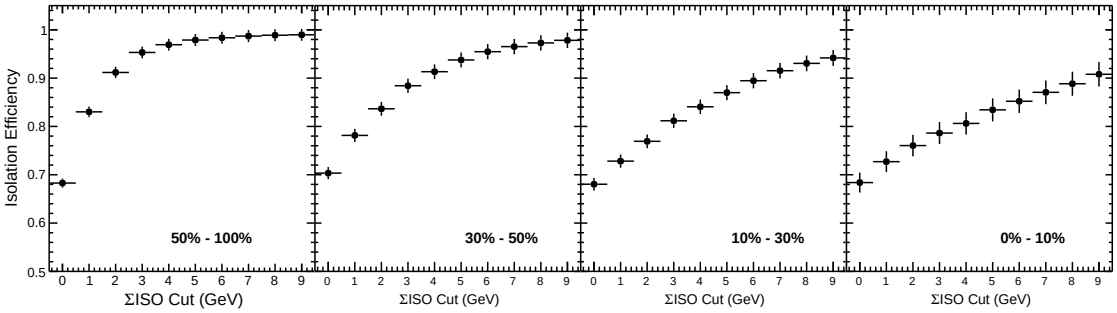

Figure 5.17: Photon isolation efficiency as a function of isolation cut which was applied in SumISO method. 1 GeV cut was used for the main analysis. This includes the supercluster reconstruction and $H/E < 0.1$ efficiency.

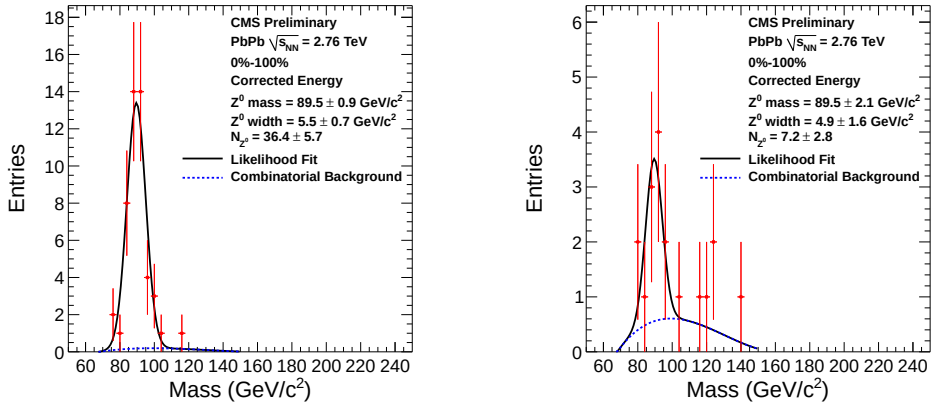

Figure 5.18: The reconstructed Z mass with two photon candidates which is calculated with the corrected photon energy and measured direction of the photon candidates. (Left Panel) Reconstructed Z mass with two photon candidates which matches with electron candidates. (Right Panel) Reconstructed Z mass with only one of the photon candidate matches with an electron candidate.

5.2.4 Rejection of Electrons

In order to suppress the contamination from electrons which come from the decay product of W and Z bosons as well as Drell-Yan processes and inclusive c- and b-jets, if a reconstructed photon candidate was matched to the supercluster reference of an electron candidate within $|\Delta\eta| < 0.03$ and $|\Delta\phi| < 0.03$, then it is rejected. The reconstruction algorithm of electron tracks used is detailed in [83].

$Z \rightarrow e^+e^-$ data was used to check the electron rejection performance. Events are selected if they had two isolated superclusters in the barrel region $|\eta| < 1.44$ (except the tracker isolation cut). Figure 5.18 shows the invariant mass distribution obtained from this study. The yield of Z bosons were computed using the binned likelihood fit. The signal component used in the yield extraction is a Gaussian and the combinatorial background component shape is obtained from a sample 3rd order equation. Then we compare the Z yield obtained from a sample in which one of the photon candidates matches an electron. The electron matching efficiency is obtained from the ratio of the Z yields in the two samples. It is found that the electron matching efficiency is 80%±5% in 0–10% central events. This is in the ballpark of the Gaussian-sum filter(GSF) electron tracking efficiency which was found to be 70–85% with $W \rightarrow e\nu$ simulation samples in PYTHIA+HYDJET.

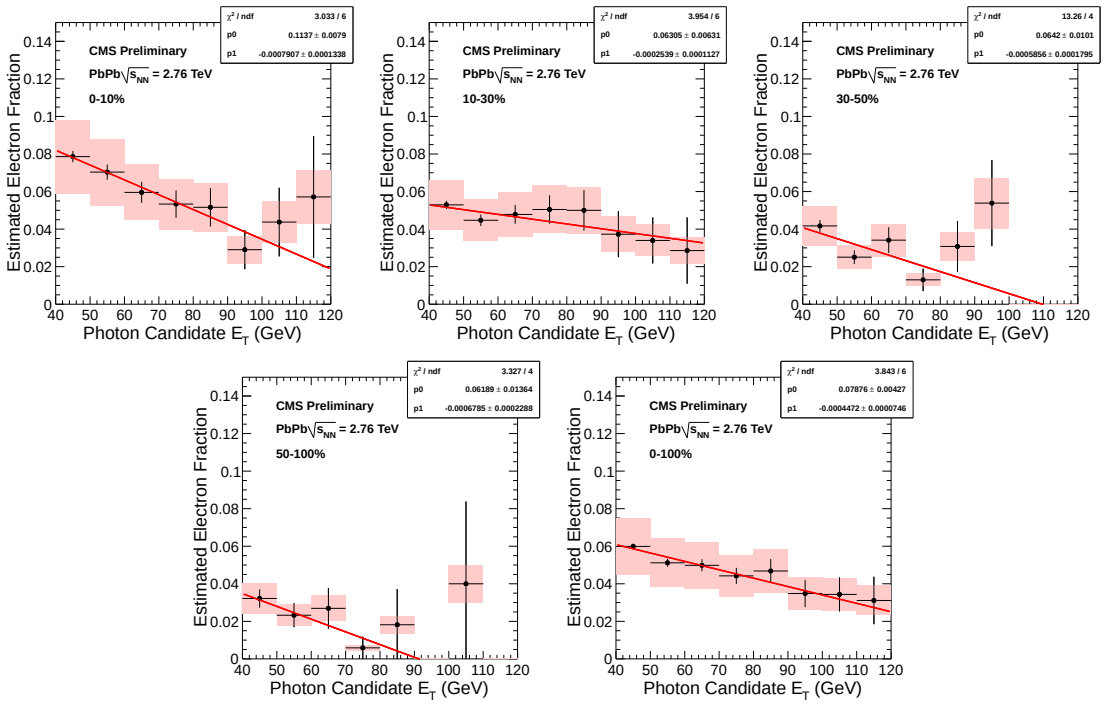

Figure 5.19: Estimated electron contamination as a function of photon candidate p_{T} for different event centrality intervals. The red line are linear fits which are only used to guide the eye (not used in the analysis). The error bars shown are statistical and the red shaded areas are the statistical uncertainties of the data-driven electron matching efficiency.

To estimate the electron contamination, we used the p_{T}spectra of isolated electron candidiates. With the electron matching efficiency obtained from Z, we can extrapolate the remaining contamination of electron candidates to the leading photon candidate after applying electron rejection criteria, which is 2–5% for photon $p_{\mathrm{T}} > 60$ GeV/c for 0–100%. The estimated electron contamination as a function of p_{T} is shown in Fig. 5.19. The electron fraction is dropping for higher photon p_{T}.

5.3 Reconstruction of Jets

The overall reconstruction procedure of jets in PbPb and pp collisions is reviewed in this section. Anti-k_T algorithm was used as the major jet finding tool as previously mentioned in Sec 2.1.2. The validation of jet reconstruction performance was done using PYTHIA+HYDJET MC samples which was introduced in Sec. 4.

5.3.1 Anti-k_T Revisited

As a **jet** is composed of **particles**, we need to reconstruct particles before finding a jet. Among various particle reconstruction methods, a CMS specialized particle reconstruction technique called **Particle Flow (PF)** was used [84]. Combined information of trackers and calorimeters are used to search particles and determine succinct characteristics. For example, if a track is found in the tracker and its position is matched to an small hit of calorimeter then it is classified as a charged particle. If a hit was found in the HCAL but no hit in the ECAL and no track in the tracker, then it is classified as a neutral hadron (neutron etc). After all, we can have the collection of PF charged particle, PF photon, PF neutral particles and these are used as the candidates of jet constituent particles. More details, i.e. efficiency and fake rates, can be found in [84]. But, the PF objects are not ready to be clustered in raw due to the background energy from underlying events. So, first the background contamination must be subtracted (Sec. 5.3.2) and then clustering algorithm can be used according to the steps described in Sec. 2.1.2.

Jets were reconstructed for $p_{\mathrm{T}} > 20$ GeV/c and $|\eta| < 3$ at the beginning. Later, we will limit our attention on narrower range $p_{\mathrm{T}} > 30$GeV/c for good energy resolution and low fake jet rate. Also, the pseudo-rapidity is restrained to be $|\eta| < 1.6$ where the PF objects are efficiently reconstructed. The jet cone radius, or jet resolution parameter, R was set as 0.3 in order to reduce the energy fluctuation caused by underlying events. This reasoning will be also explained in the following section.

5.3.2 Subtraction of Pedestal Background Energy in Jet Cone

One of the major challenges of jet reconstruction in heavy ion experiment is the the large particle multiplicity made by underlying events. As introduced in Sec. 5.1.1, a hard scattering of jet can be attributed to a single sub-collision of two constituent nucleons in each of colliding ions. Rest of nucleons - upto ∼416 participants ($= 2 \times$ number of nucleons in a lead ion) - contributes to the production of soft underlying particles

which are not correlated to the jet.

In other words, the jet signal is made on top of pedestal background energy. Traditionally, the jet algorithms had been designed to be optimized for pp or electron-positron collisions where the underlying event is negligible. This is also true for anti-k_T. Therefore, it should be modified to coun out the background energy.

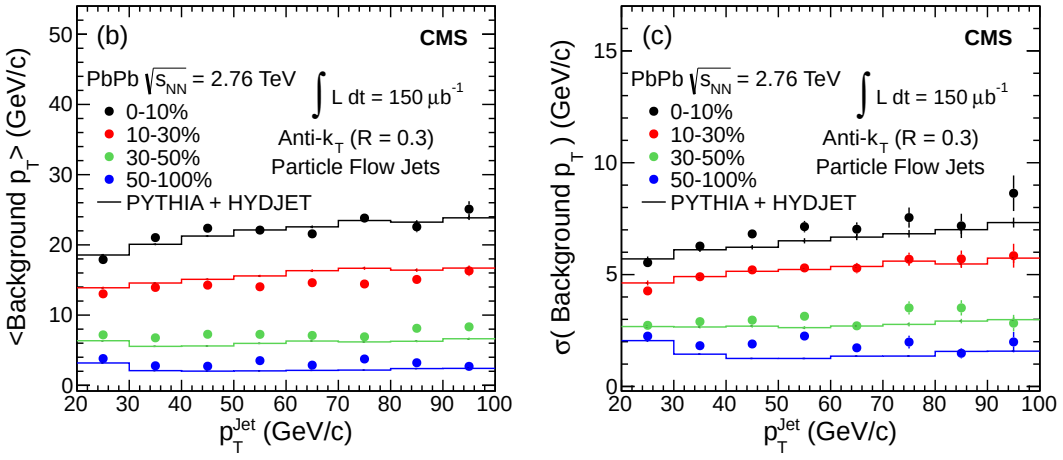

Figure 5.20: The average transverse background energy and its σ, or fluctuation level, for reconstructed jets within $|\eta|<2$ in 4 centrality bins. Data points represent the real Pb+Pb collisions and histogram lines mean PYTHIA+HYDJET simulation.

The "noise/pedestal subtraction" technique introduced in Ref [85] was used to subtract the background contamination in jet cone event by event. Originally this algorithm was designed for jets whose constituents are discrete energy towers of granular calorimeters, whereas we want to make jets based on PF objects which are mapped in the continuous $\eta\times\phi$ plane. So, a minor modification was applied in this algorithm. The PF objects are merged to a fixed $\eta\times\phi$ bin which corresponds to the HCAL cells. After this projection, the mean value and dispersion of the energies recorded in the calorimeter cells are calculated for the band of cells in the area of $0<\phi<2\pi$ and η.

The value of pedestal energy as a function of pseudo-rapidity, P(η), is essentially the mean value of energy in this band of cells. This value is subtracted from all cells. If a cell energy comes out negative then it is set to zero. The algorithm subtracts $\langle E_{\text{cell}}\rangle+\sigma(E_{\text{cell}})$ from each cell in order to compensate for the bias caused by this elimination of negative energy.

Finally, it is time to cluster the cells - to which PF objects are projected - into jets

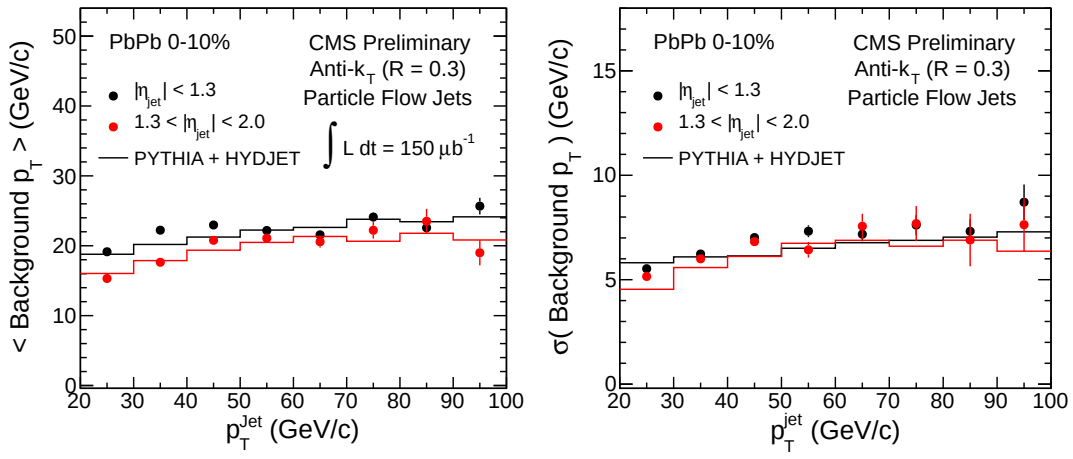

Figure 5.21: The average transverse background energy and its σ, or fluctuation level, for reconstructed jets in two η < bins at the most central collision events. Data points represent the real Pb+Pb collisions and histogram lines mean PYTHIA+HYDJET simulation.

using anti-k_T algorithm. In the second iteration, the pedestal function is recalculated using only calorimeter cells outside of the area covered by reconstructed high jets with $p_T > 15$ GeV/c. The threshold 15GeV/c was chosen to optimize the final extracted jet energy resolution.

The estimated background energy $\langle p_T \rangle$ for jets within $|\eta| < 2$ as a function of collision centrality in PbPb data can be found in Fig 5.21. The average background (in terms of $\langle p_T \rangle$ and RMS) seems to be moderately consistent with MC simulations over wide range of reconstructed jet p_T. The background energy subtraction considerably takes part in the uncertainty and the contribution is proportional to the cone radius. This is the reason why we prefer to use relatively small cone radius $R = 0.3$, although we have to surrender covering softly radiating particles.

For the p+pdata anlasis, the pileup subtraction is not applied.

5.3.3 Energy Correction for Reconstructed Jet

Reconstruction efficiency of PF object (Sec. 5.3) is not obviously 100% because of the detector is not literally ideal. In other words, some fraction of particles can randomly pass though the detector and are not caught by PF algorithm. So, the raw energy of jet - sum of energies in PF object projected cells - tends to be lower than the real energy of it. To recover this discrepancy, we need to multiply a correction factor which can be

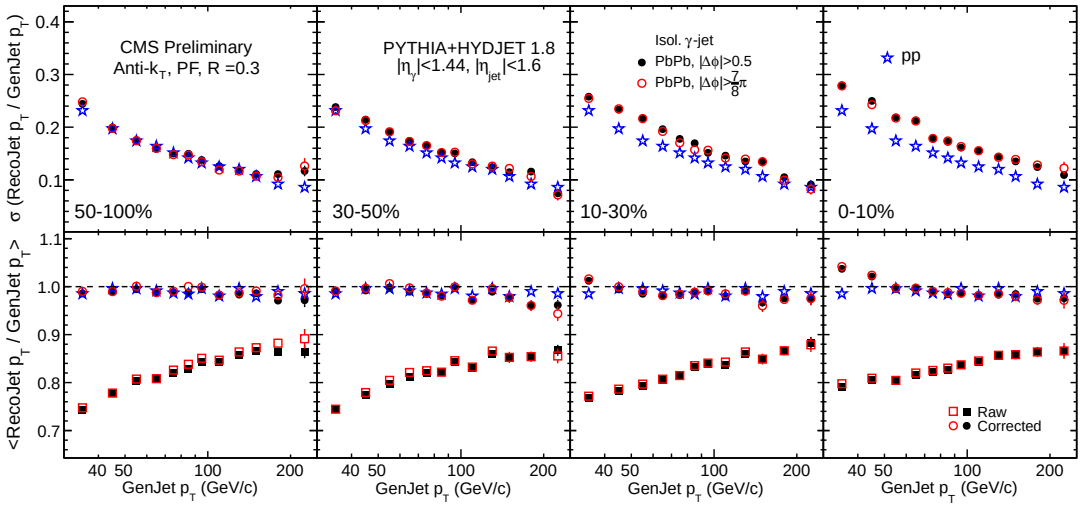

Figure 5.22: Jet energy scale and resolution of anti-k_T PF algorithm with $R = 0.3$. PYTHIA and PYTHIA+HYDJET sample was used for the simulations of p+p and Pb+Pb respectively.

obtained from PYTHIA+HYDJET simulation.

As one can access to the generated particles in MC simulation, jets can be clustered based on the MC particles by the anti-k_T algorithm. This is called *GenJet*, or generator level jet. On the other hand, the jet based on the reconstructed particles is called *RecoJet*. If the detector can perfectly detect all the particles and their momenta, the reconstructed jet energy would be identical to that of GenJet. The correction factors were obtained by comparing the reconstructed jet energy to GenJet energy, in various p_{T} and η bins to reduce the systematic uncertainty.

In the technical language, the correction factor is the ratio of raw energy of RecoJet to energy of the corresponding GenJet. It can be seen from Fig 5.23 that the energy scale at higher η (1.6<| η |<2.0) in 0-10% central collisions is off from unity due to poorer jet reconstruction efficiency in this pseudo-rapidity interval. In order to avoid any ambiguities due to this in the analysis we reconstructed only the jets within <| η |<1.6.

Figure 5.22 shows the resolution of the reconstructed jet energy as a function of p_{T} and collision centralities. There is a good agreement for the most peripheral PbPb and the pp samples. The jet energy scale in pp events do not exhibit perfect closure but a few percent off from unity, because the standard correction factor in CMS software is made based on di- jet samples in which the majority of jets are seeded by gluons, whereas in $\gamma-$jet events, most of them are by quarks. The amount of non-closure was quoted as

the systematic uncertainty in the final results. From now on, the jet p_{T} means the final value after the applicaiton of all correction factors unless specifically mentioned.

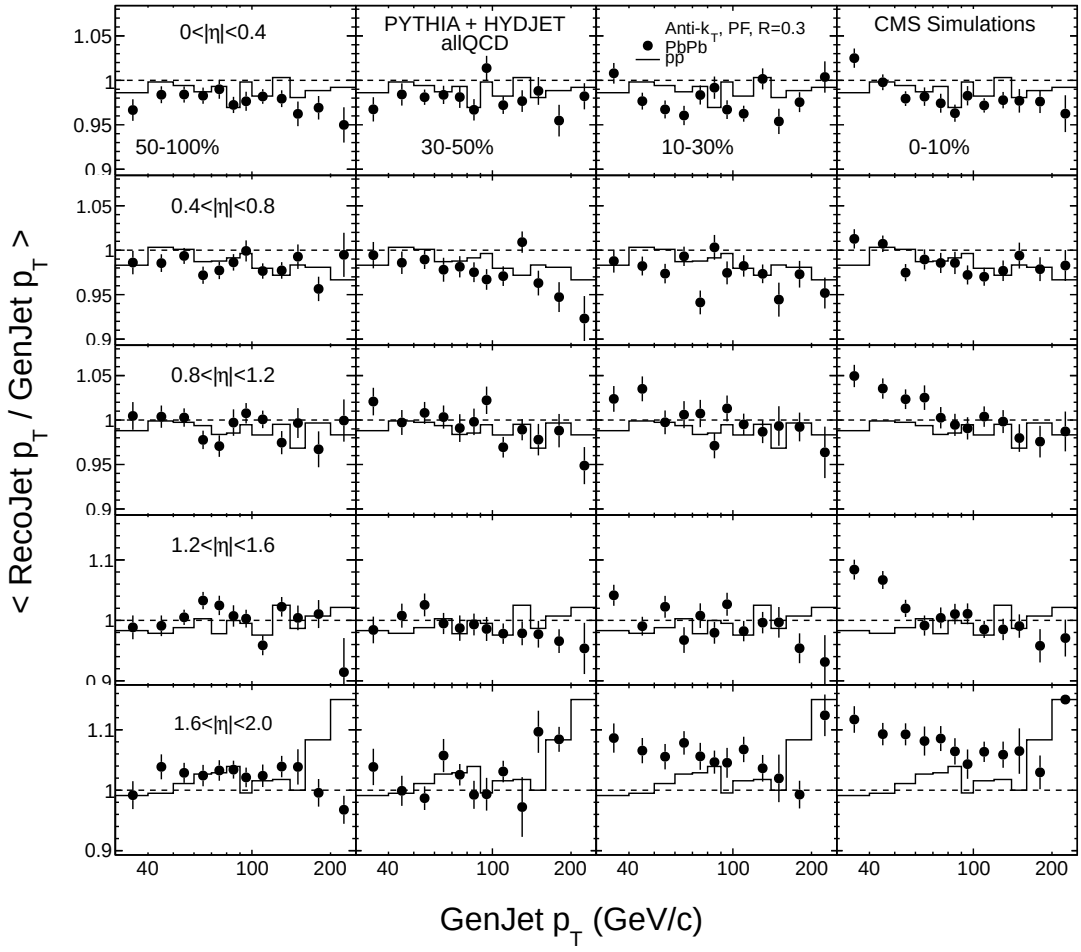

Figure 5.23: η and p_{T} dependence of the jet energy scale of Anti-k_T algorithm used in this anlaysis. PYTHIA+HYDJET MC simulation was used for this study.

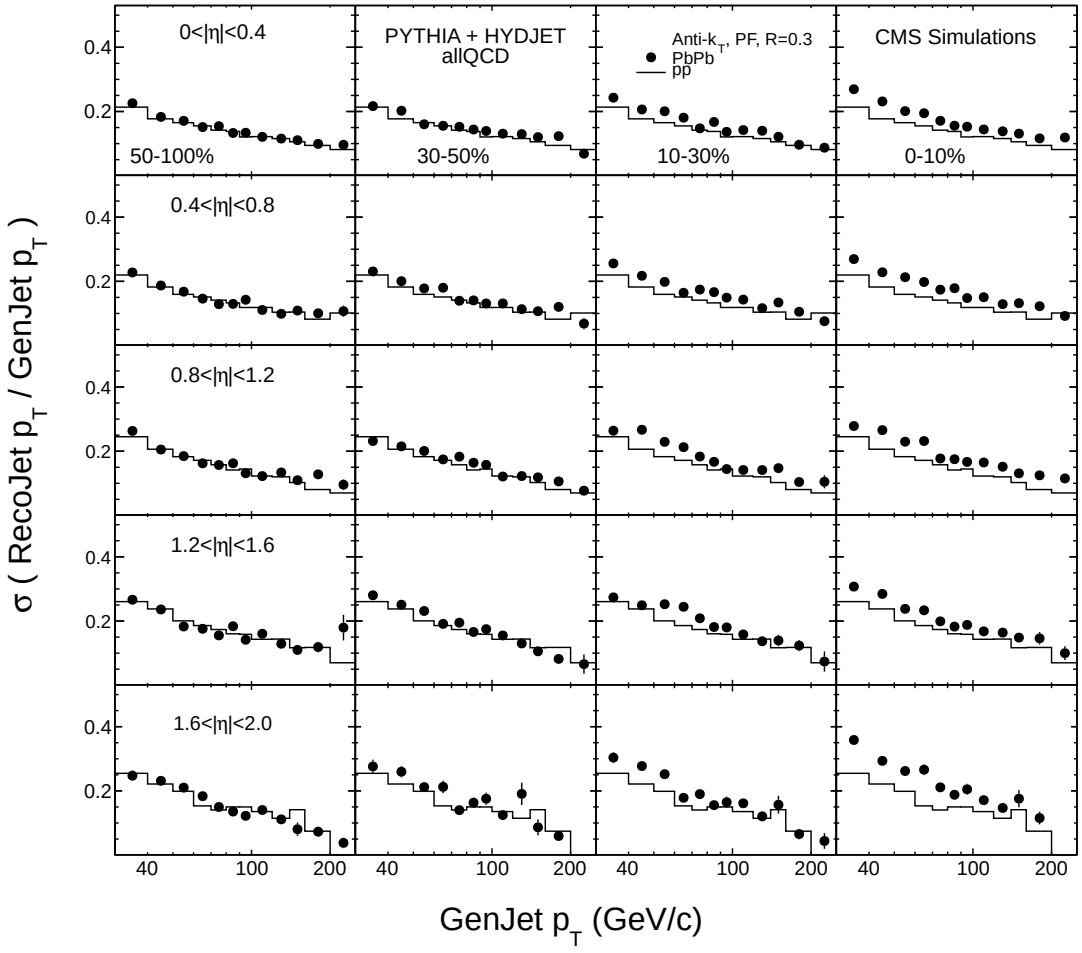

Figure 5.24: η and p_{T} dependence of the jet energy resolution of Anti-k_T algorithm used in this anlaysis. PYTHIA+HYDJET MC simulation was used for this study.

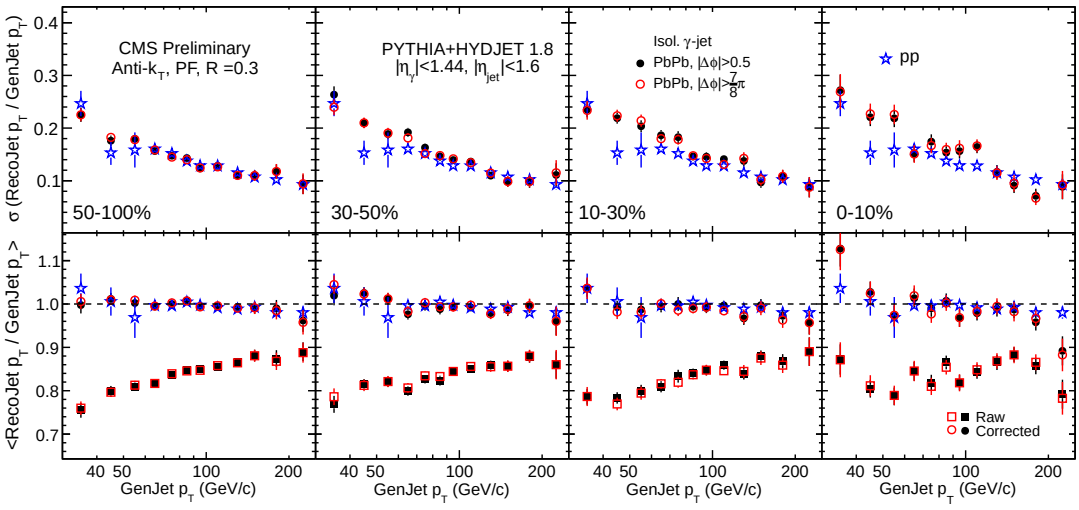

Figure 5.25: Jet energy scale and resolution of Anti-k_T algorithm used in this anlaysis. PYTHIA+HYDJET MC simulation was used for this study.

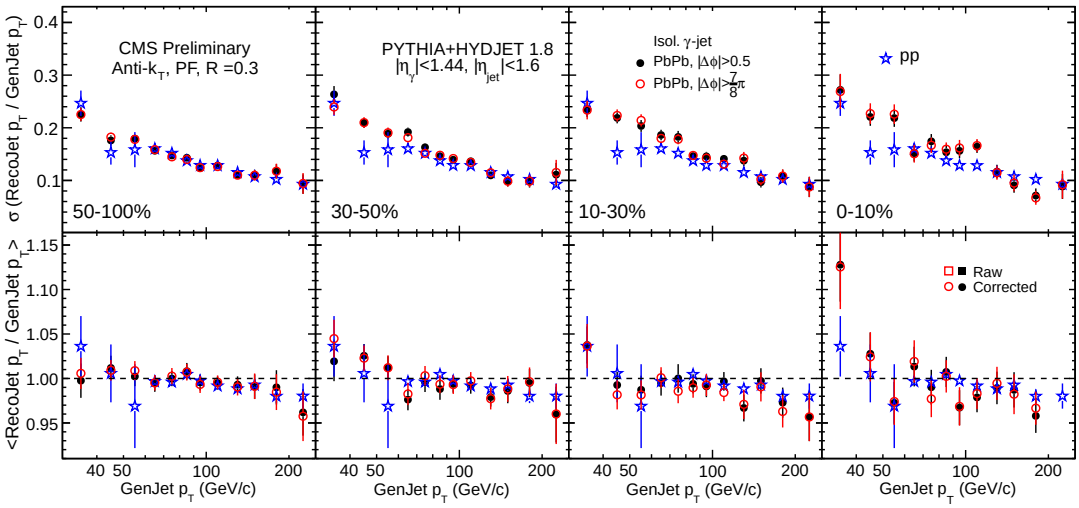

Figure 5.26: Zoomed in version of Fig 5.25.

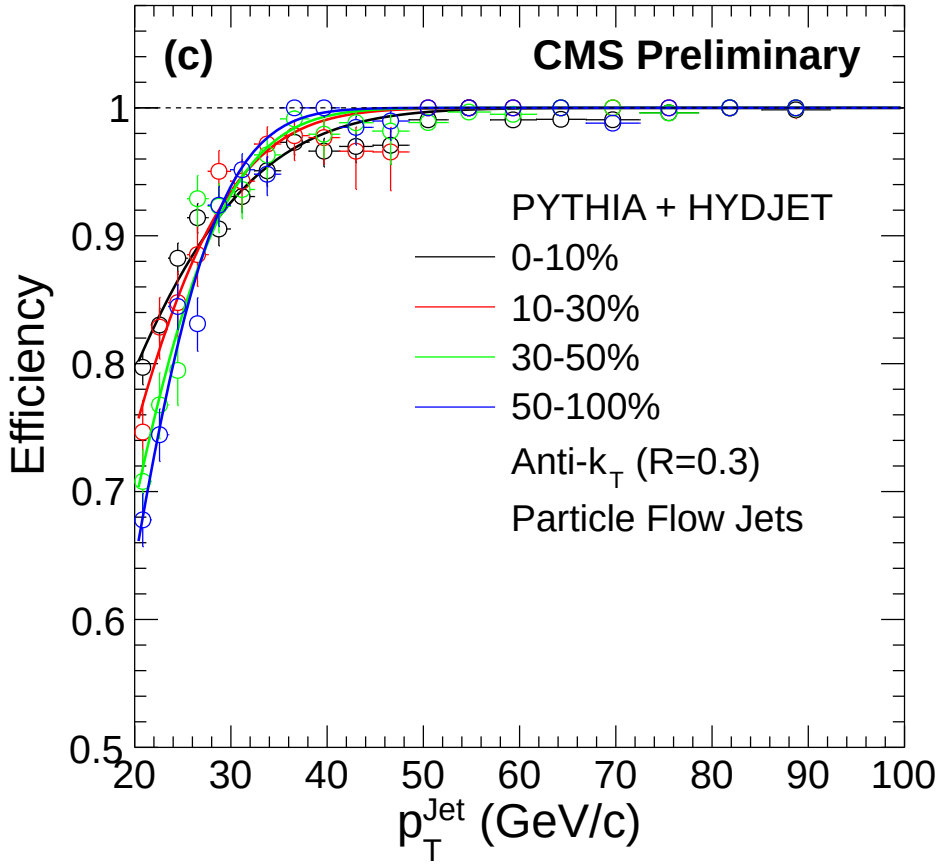

Figure 5.27: The jet finding efficiency of Anti-k_T algorithm used in this analysis. The $\gamma-$jet events generated in PYTHIA+HYDJET MC simulation was used for this study

5.3.4 Validation of Jet Reconstruction Algorithm

The $\gamma-$jet MC samples using PYTHIA+HYDJET were used to study various jet reconstruction performance including jet finding efficiency, energy scale/resolution and position resolution.

5.3.4.1 Jet Finding Efficiency

Jet finding efficiency is the probability for a real jet to be found in the reconstruction level. It depends on the detector condition and jet finding algorithm, so the efficiency varies by the jet energy and its position in the $\eta \times \phi$ map. In th technical language of MC simulation, the efficiency is defined by the probability that a GenJet is found as a RecoJet. Figure 5.27 shows the efficiency turn-on curve.

5.3.4.2 Jet Energy Scale

The jet energy scale and resolution for can be found from Fig. 5.22 to Fig. 5.26. As expected, the energy scale is almost flat at the unity. For some bins, they are a few percent off from the unity by the reasons explained in Sec. 5.3.3 (discrepancy between quark jets and gluon jets).

5.3.4.3 Jet Angular Resolution

Angular resolution of the jets is studied by comparing RecoJet ϕ and the matched GenJet ϕ in bins of centrality as well as in bins of the jet p_{T}. In addition, the angular resolution of reconstructed photon was also investigated using the same method, because we will be interested in the angular correlation between photon and jet later (Sec. 8.2.1). Figure 5.28 shows the angular resolutions of the reconstructed jet, photon, and photon-jet.

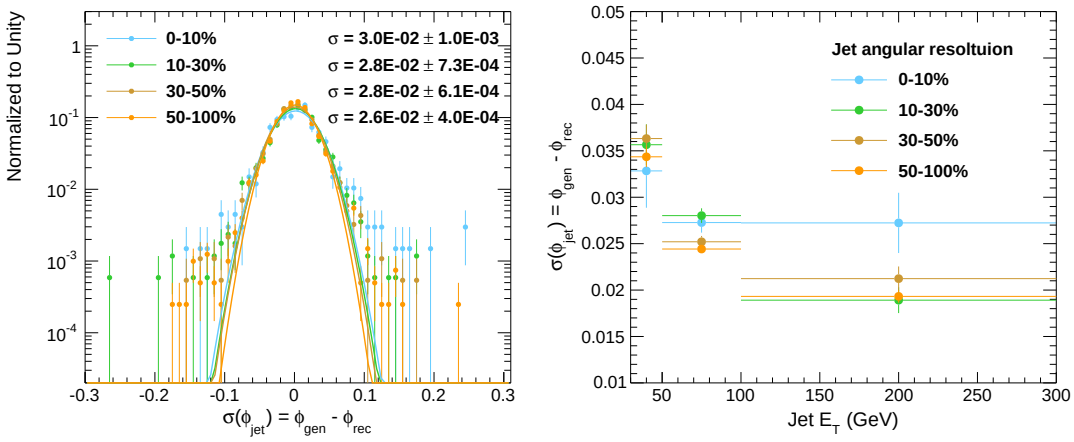

Figure 5.28: (Left) Angular resolution of reconstructed jet axis in 4 centrality bins. Each distribution is fitted with single Gaussian function. The σ's (width) of each distributions are shown in the legend. (Right) The angular resolution of reconstructed jet as a function of jet p_{T} in 4 centrality bins.

6 Extraction of Direct Photons

In the previous chapter, we discussed the reconstruction sequence of the isolated photon candidates. Using the H/E and isolation cut, bulk of the background photons (mostly π^0) can be rejected, but the fraction of background to signal is still O(1). Since it is not anymore easy to distinguish signals from backgrounds event-by-event, the last step to extract the direct photons is made by a statistical approach. The final number we want to extract out of this process is the **purity** which is defined as the ratio of direct photons to the all candidates. This chapter is devoted to thoroughly explain the procedure of purity determination, because it is the most important key parameter in the background subtraction procedure in the whole analysis of this thesis.

6.1 Shower Shape

The *shower shape* variable $\sigma_{\eta\eta}$ characterizes the energy distribution of a photon candidate by means of the fine segment of the ECAL crystals. Since the background photon candidates are made by double photon pairs (π^0, η, etc $\rightarrow \gamma+\gamma$), they tend to produce wider transverse shower shape compared to prompt photons. In CMS experiments, it is possible to statistically separate the signals from backgrounds up to about $p_{\mathrm{T}} \sim 150$GeV.

$\sigma_{\eta\eta}$ was defined to quantitatively characterize the shower shape in the η direction as below.

$$\sigma^2_{\eta\eta} = \frac{\sum_i^{5\times5} w_i(\eta_i - \eta_{5\times5})^2}{\sum_i^{5\times5} w_i}, w_i = \max(0, c + \ln\frac{E_i}{E_{5\times5}}), \tag{6.1}$$

where E_i and η_i are the energy and pseudo-rapidity of the i^{th} crystal within the 5×5 crystals.

The value of c is a constant which was set to 4.7 in and effectively cut-off the low energy crystals for the shower shape sampling. The isolated photon candidates tend to have smaller $\sigma_{\eta\eta}$ while hadrons and decay photons to have larger $\sigma_{\eta\eta}$ as shown in Fig. 6.1.

The photon candidates with $\sigma_{\eta\eta} < 0.01$ were selected for the final results and they

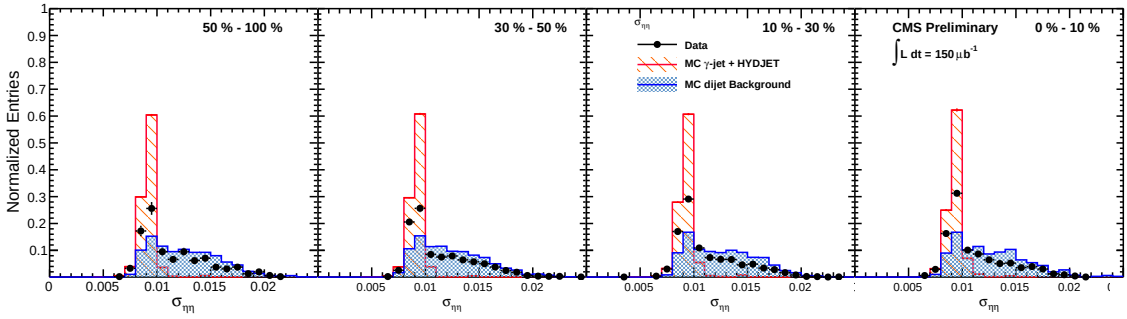

Figure 6.1: Comparion of $\sigma_{\eta\eta}$ of PYTHIA direct photons, PYTHIA background photons and photon candidates in real Pb+Pb data. Studied were repeated for 4 centrality intervals to check the dependence on underlying events, but apparently the shower shape is almost independent on it by virtue of the cut-off of crystal energy. The kinematic cuts of $p_{\mathrm{T}} > 60$ GeV and $|\eta| < 1.44$ was applied.

are called *good (tighti) photon candidates*. The photon candidates with $\sigma_{\eta\eta} > 0.011$ are background enriched region, so they are used as the input for the background subtraction procedure which will be explained in Sec. 7.3.

6.2 Selection of Good Photon Candidates

In order to maintain high purity of the photon jet events, various cuts using photon identification variables were applied.

First, reconstructed ECAL superclusters with $E_T > 60$ GeV and $|\eta| < 1.44$ are selected as the primitive photon candidates.

Secondly, offline ECAL spike rejection is done by requiring the *Swiss Cross Variable* $(1 - E_4/E_1) < 0.9$ and hit reconstruction timing $|t| < 3$ ns; settings which are tighter than the online filtering [46]. In addition, a candidate is rejected if it fails to find its seed in the reconstructed crystal collection. The fraction of such superclusters is negligible (less than 0.5%) and it is counted in the reconstruction efficiency calculation. Also we require the $\sigma_{\eta\eta} > 0.002$ to reject very short clusters. The remnants of spikes were estimated to be smaller than 2% as shown in Fig. 3.7.

Third, $H/E < 0.1$, the fraction of HCAL energy relative to the ECAL energy in the cone of R = 0.15, is applied to reject most of the high p_{T} changed hadrons from jets.

Forth, **SumIso** (defined in Sec. 4.2.2) is calculated around the candidate and it is selected if it is smaller than 1 GeV. This procedure is done in order to reject the neutral

hadrons that is fragmented from jets and non-isolated photons as well. As the last step, $\sigma_{\eta\eta} < 0.01$ is required to suppress the contamination of the isolated neutral mesons such as high p_{T} π^0.

Fifth, if the photon candidate is identified as electrons by GSF track matching (Sec. 5.2.4) then it is disqualified.

In summary, the reconstructed photon in ECAL is counted as good photon if it satisfies (1) transverse energy is higher than 60 GeV and $|\eta|$ is smaller than 1.44 (2) it is identified as not being an anomalous signal, (3) the fraction of hadronic activity in the cone of R = 0.15 is smaller than 0.1 (4) reconstructed isolation energy after background subtraction is smaller than 1 GeV, (5) the shower shape variable $\sigma_{\eta\eta} < 0.01$ and (6) it is not matched with reconstructed electron candidate. The selection criteria are summarized in Table 6.1.

Kind of cuts	Shower shape method
Vertex constraint	$\lvert Z_{vertex}\rvert < 15$ cm
Anomalous signal removal	$1 - E_4/E_1 < 0.9$
Ratio of hadronic and electromagnetic energy	$H/E < 0.1$
Electron rejection	No electron candidates matched
Shower shape selection	$\sigma_{\eta\eta} < 0.010$
Isolation selection	*SumIso* < 1 GeV

Table 6.1: List of photon isolation and identification selection criteria.

6.3 Purity of Photon Candidates

Using the selection criteria described above, the population of good photon candidates is now dominated by direct photons, but still there exists background contamination at about 20% level. The accurate fraction of the remaining backgrounds can be statistically calculated via the *Template method*, which uses a two-component fit of the shower shape in ECAL crystal. The purity extracted in this procedure is later used to deduct the contamination of di-jet events, in which one jet has high p_{T} π^0, from the $\gamma-$jetcandidates in Sec. 7.3.

A **template** is defined as the probability distribution function of $\sigma_{\eta\eta}$ of either pure photons (**Signal templates**) or pure background (e.g. π^0) (**Background templates**), which are shown in Fig. 6.1. As discussed in the previous section, the background templates tend to have broader $\sigma_{\eta\eta}$ distribution up to 0.025 because of the wider

transverse shower shape. The signal template was obtained from MC photon samples PYTHIA+HYDJET. And the background template was obtained in data-driven way from the SumIso sideband (10 GeV< SumIso < 20 GeV), which is the background-enriched region. The yield of signals was extracted via fitting the $\sigma_{\eta\eta}$ distribution of the data by the signal and background templates. Figure 6.2 - Figure 6.4 show the performance of the maximal likelihood fits in the 4 centrality intervals. The p_{T} dependence of the photon purity was also studied and shown in Fig. 6.5. The figure indicates that the ratio of direct photons to decay photons increases for higher p_{T} ranges.

The shower shape template method was originally developed by CMS collaboration to measure the spectra of direct photons both in pp and PbPb collisions. More examples of the application of this method can be found in the photon $\mathrm{R_{AA}}$ paper [46].

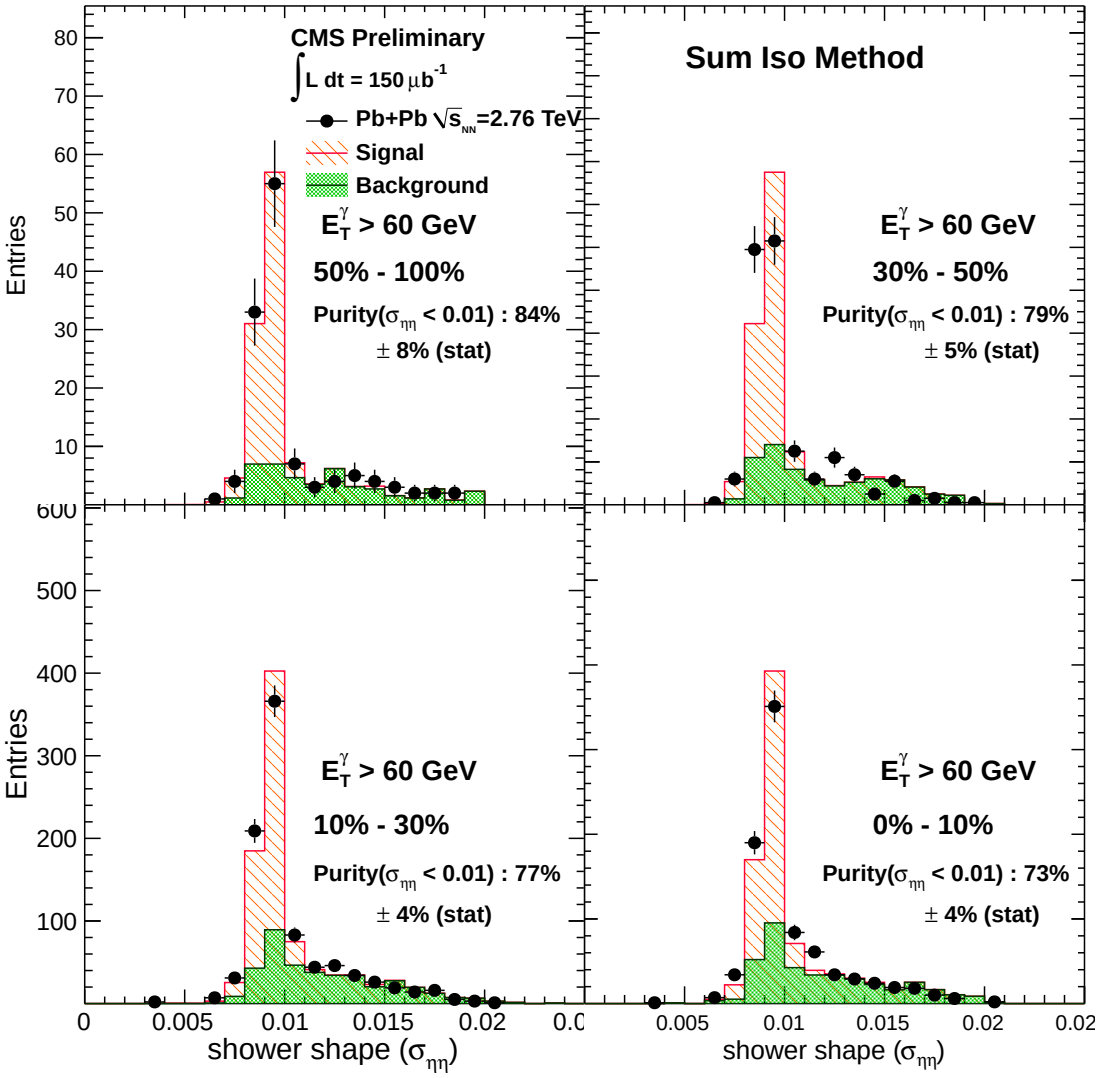

Figure 6.2: Purity calculation of photon candidates with p_T above 60GeV/c, which is used for the $\gamma-$jetselection in four centrality bins. The calorimeter isolation requirement is **SumIso** < 1 GeV in this analysis.

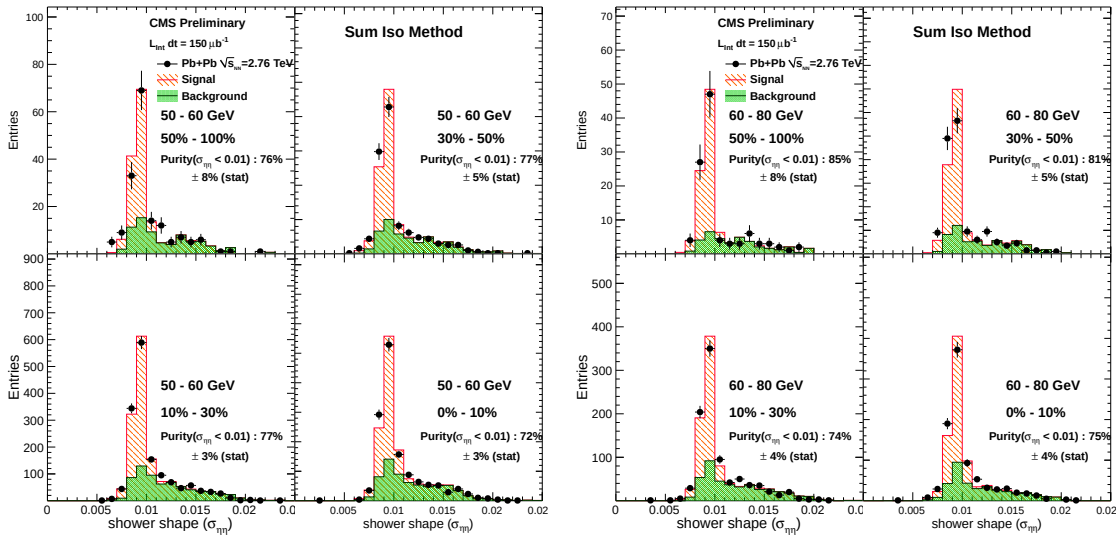

Figure 6.3: Purity calculation of photon candidates with p_T of 50-60 GeV/c and 60-80GeV/c intervals in four centrality bins. The calorimeter isolation requirement is **SumIso** < 1 GeV in this analysis.

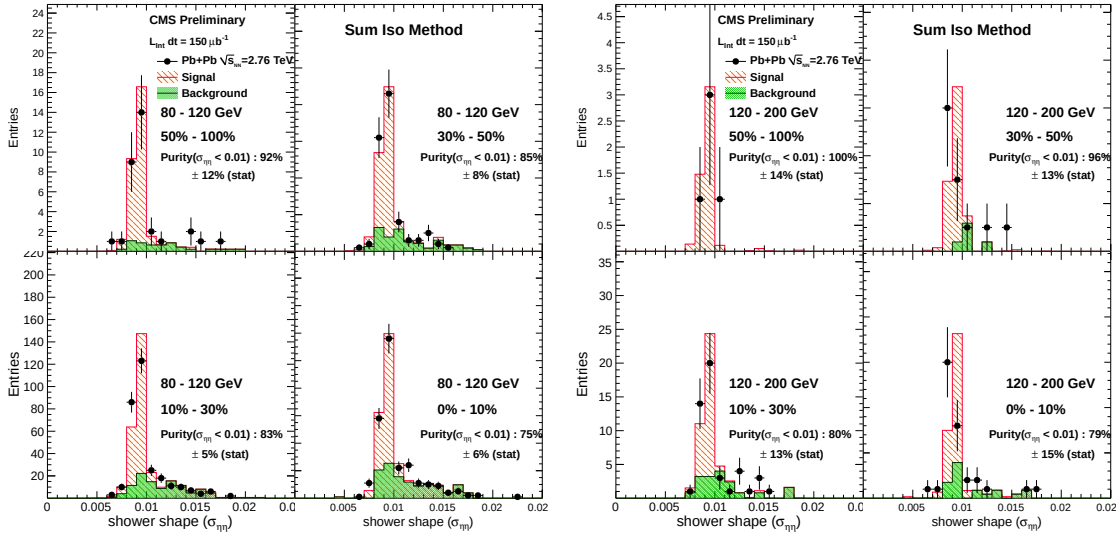

Figure 6.4: Purity calculation of photon candidates with p_T of 80-120 GeV/c and 120-200GeV/c intervals in four centrality bins. The calorimeter isolation requirement is **SumIso** < 1 GeV in this analysis.

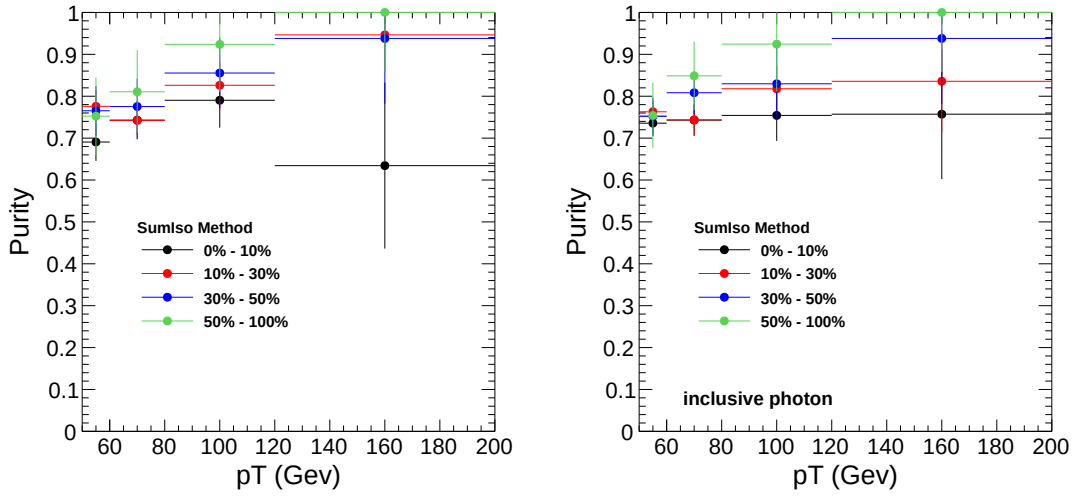

Figure 6.5: Purity of isolated photon candidates. Left is the photon candidates which satisfies away-side jet requirement, and the right is the inclusive photons.

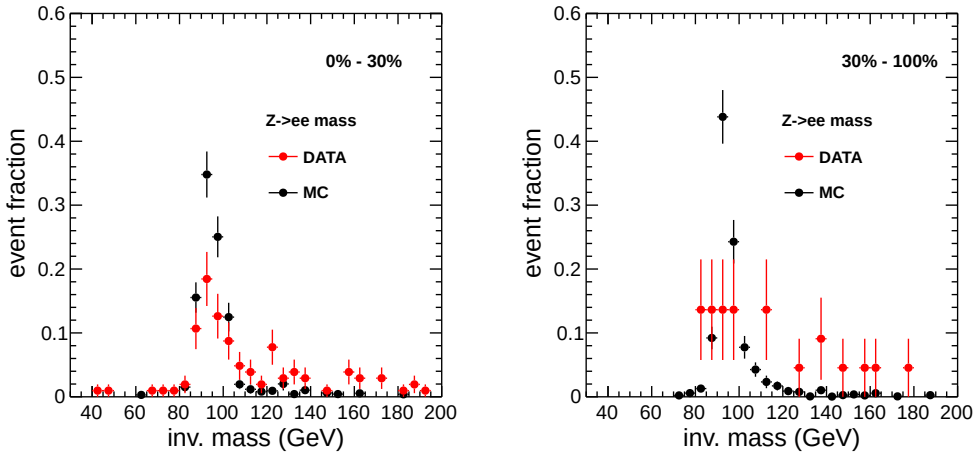

Figure 6.6: Invariant mass of Z bosons reconstructed from electron pairs. One electron was required to satisfy $p_{\mathrm{T}} > 20\,\mathrm{GeV}$, $H/E < 0.2$ and $\sigma_{\eta\eta} < 0.01$, and the second one was required to satisfy $p_{\mathrm{T}} > 50\,\mathrm{GeV}$, $H/E < 0.1$ and SumIso $< 1\,\mathrm{GeV}$.

6.4 Systematic Uncertainty of Photon Counting

6.4.1 Discrepancy of Shower Shape between data and MC

To verify the shower shape ($\sigma_{\eta\eta}$) distribution of signal obtained from MC photon, it was compared with the shower shape obtained from electrons in $Z \rightarrow e\,e$ events in the real data.

Once an electron candidate is found with $p_{\mathrm{T}} > 30\,\mathrm{GeV}$, $H/E < 0.2$ and $\sigma_{\eta\eta} < 0.01$, then the second electron candidate which satisfies $p_{\mathrm{T}} > 40\,\mathrm{GeV}$, $H/E < 0.1$ and SumIso $< 1\,\mathrm{GeV}$ is searched. Figure 6.6 shows the distribution of invariant mass of electron pairs in two different centrality bins.

If the pair of electrons has invariant mass between 80 GeV–100 GeV, then the the shower shape of the second candidate is use to be compared with MC shower shape of photons with same kinematic and isolation requirement. Figure 6.7 shows the comparison of $\sigma_{\eta\eta}$. By comparing the mean of the distributions, the data distribution is shifted by 0.00013 compared to MC.

This kind of data driven method is called **tag-and-probe** and more details can be found in [86].

The systematic uncertainty of purity measurement from this discrepancy is estimated by shifting the MC photon templates by 0.00013 in the following section.

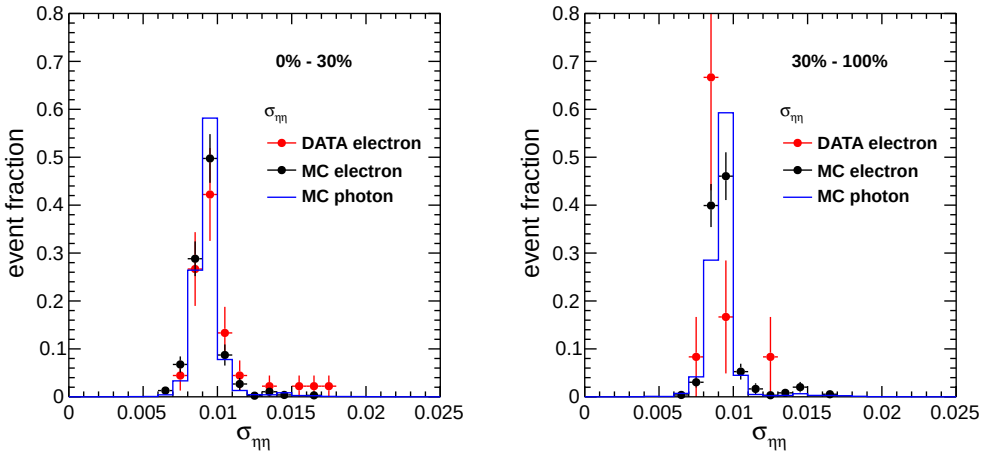

Figure 6.7: Comparison of shower shape of electron in $Z \rightarrow ee$ and MC photon templates.

The uncertainty of the photon purity measurement using template method was estimated by varying (1) the uncertainty by discrepancy of signal templates in MC and data and (2) the selection of sideband region (SumIso $10-20$ GeV) which was used to obtain the background template.

(1) Uncertainty due to the shift of signal template peak. The shift that was seen in Fig. 6.5 is due to the subtle difference between data and MC in the energy scale of the pedestal background. To estimate the systematic uncertainty due to this effect, the signal template was modified by shifting on horizontal axis. The amount of shift was varied from -0.0002 to +0.0002 and we checked how much the fitting performance is improved and what is the variance of purity value. The goodness of fitting was quantified as χ^2 divided by degree of freedom and it was found that the templates fit best when signal template is shifted by -0.00014 (0-30%), -0.00016 (30-100%). (Fig. 6.11 - Fig. 6.13) The deviation of purity is smaller than 2% which is negligible. Fig. 6.13 shows the dependence of purity on photon p_T and centrality, with a linear fit (for illustration).

(2) Uncertainty due to background template. A similar study was performed on the sideband region, which we used to select data-driven background template. The SumIso sideband was varied from 5–15 GeV to 10–20 GeV while fixing the width as 10 GeV and then checked how much is the deviation of the corrected inclusive photon yield, as shown in Fig. 6.14. The amount of maximum deviation of the

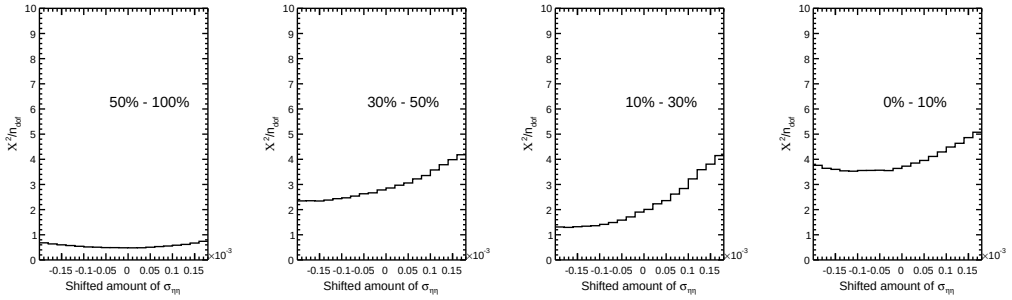

Figure 6.8: χ^2 divided by degree of freedom as a function of shifted amount of signal template.

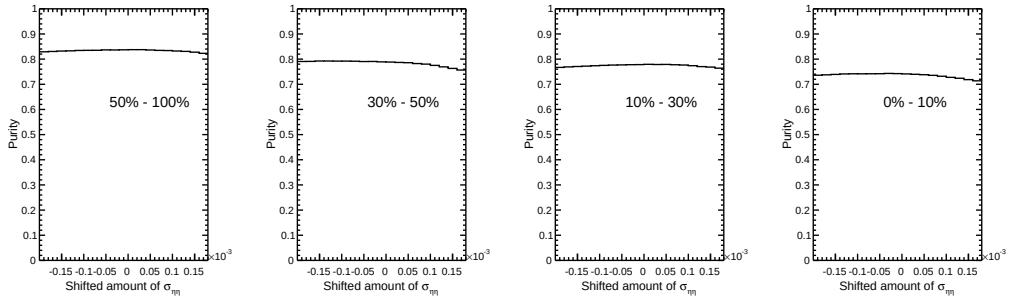

Figure 6.9: (Middle) The dependence of purity on the shifted amount of signal template.

fluctuation was 12%.

In addition, we were convinced that the sideband background template can reproduce the template of background candidates in the signal region (SumISO < 1 GeV) by comparing the MC background templates in both regime. As shown in Fig 6.15, MC background templates in signal region and sideband region overlaps within statistical uncertainty.

The systematic uncertainty of photon purity was set 12% which is the root of quadrature sum of uncertainties in (1), (2).

Fig. 6.16 shows the p_{T} dependence of the efficiency of the isolation cut. Figure 6.17 shows the dependence of the photon isolation efficiency on the momentum imbalance of the photon–jet pair, and on the $|\Delta\phi|$ between the γ and jet. Figure 6.18 shows the number of inclusive isolated photons above 60 GeV, measured by counting the signals from fitting and then corrected by isolation efficiency. The yields were compared with

different isolation cut; 0GeV (the tightest) though 9GeV (the loosest), and the maximum deviation of the final yield was 13%.

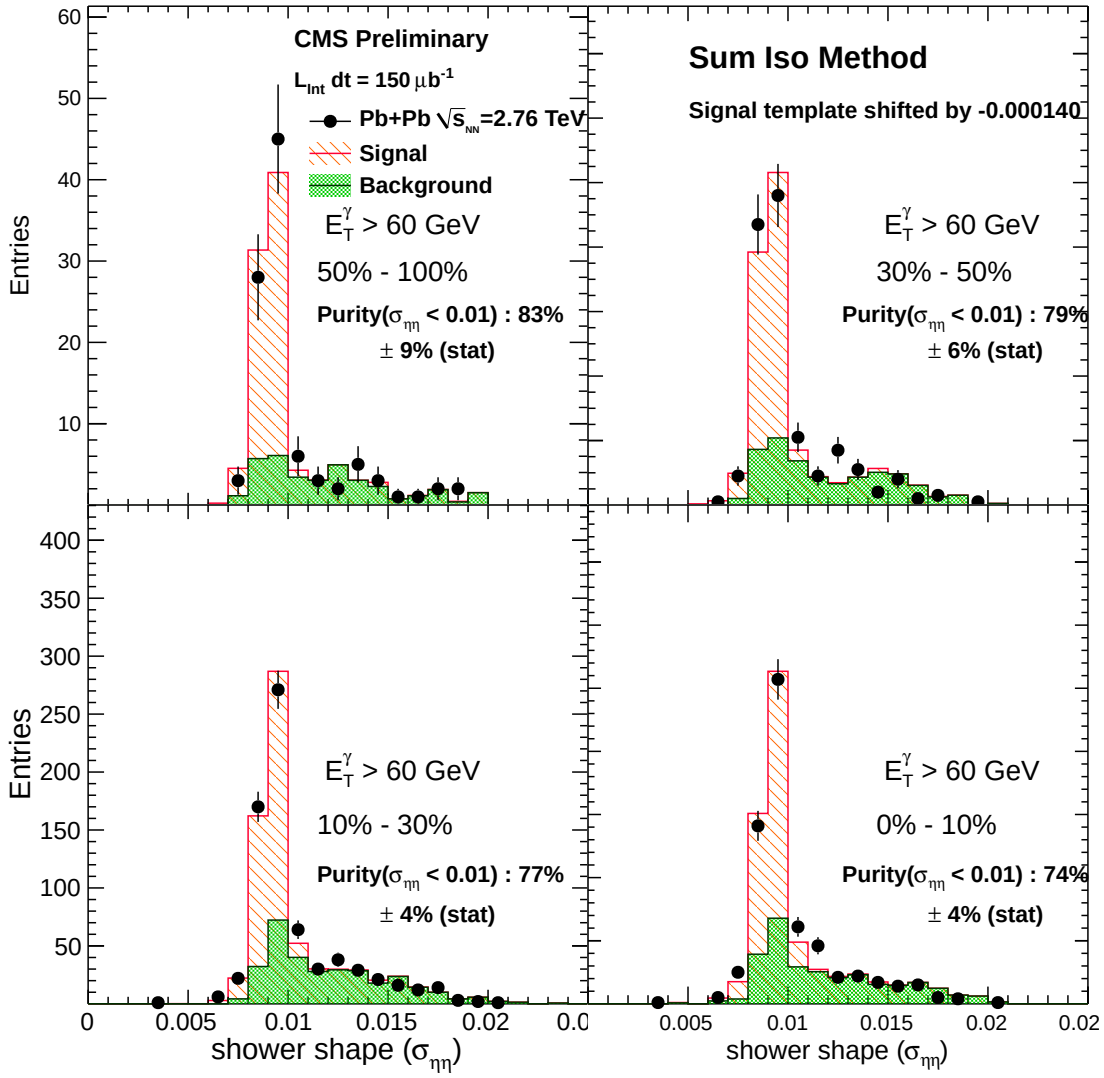

Figure 6.10: Fitting performance of photons in all p_T ranges after shifting signal template by -0.00014

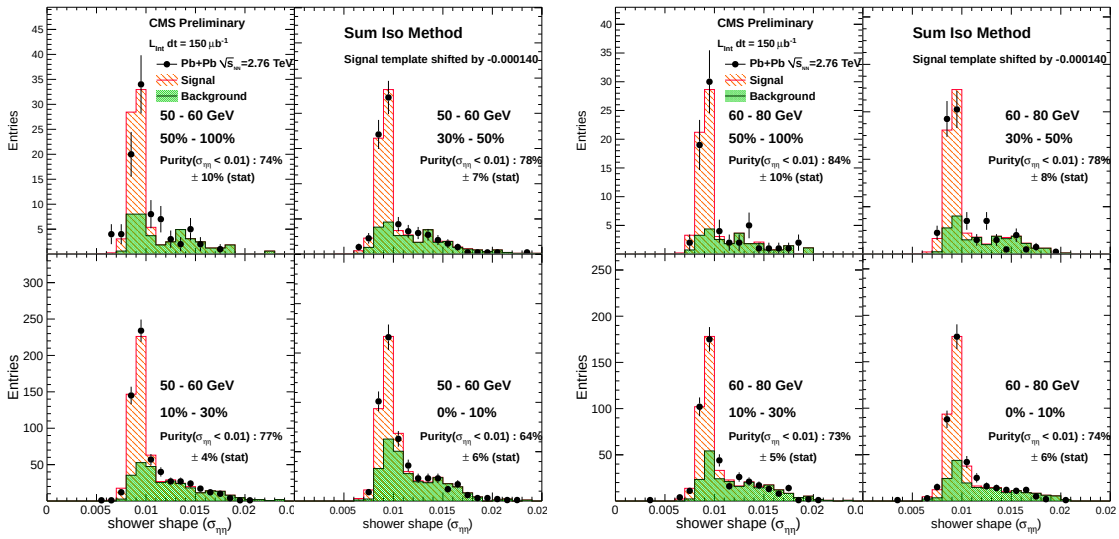

Figure 6.11: Fitting performance of the first and second p_T interval after shifting signal template by -0.00014

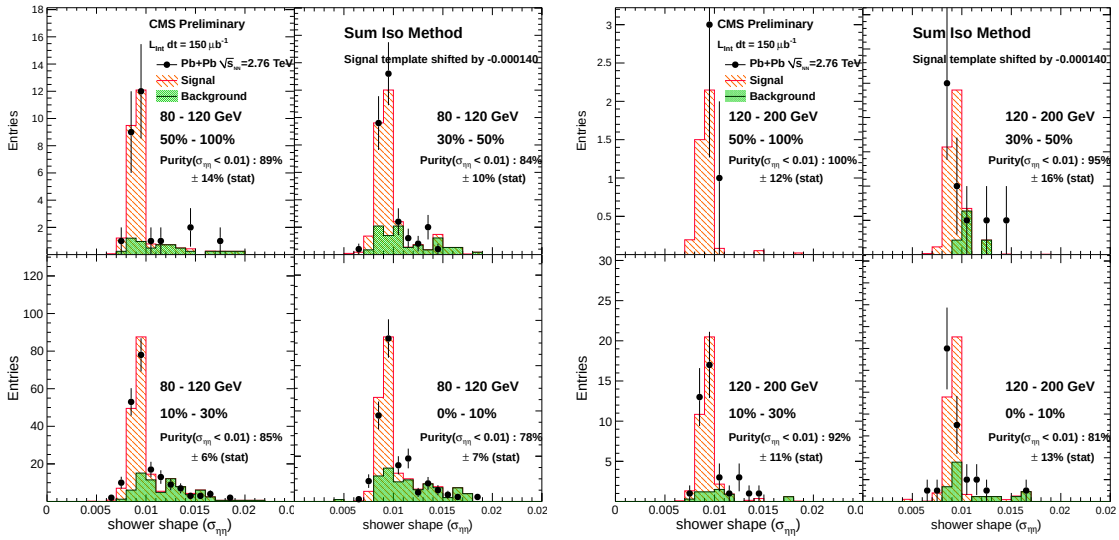

Figure 6.12: Fitting performance of the third and fourth p_T interval after shifting signal template by -0.00014

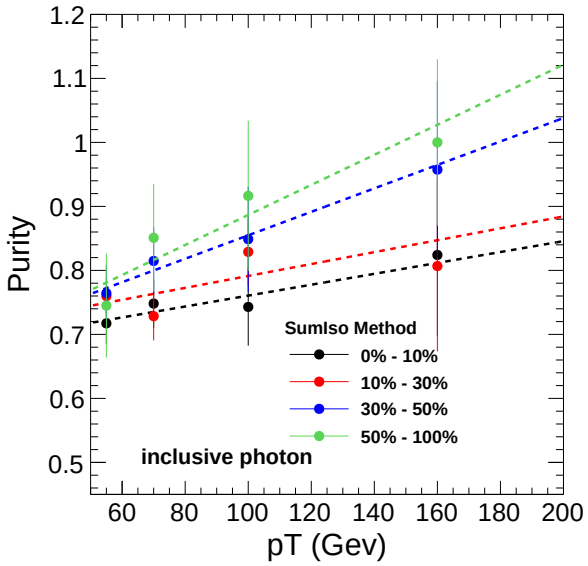

Figure 6.13: Dependence of purity on photon p_T and centrality. The points were fit by a linear function (only for illustration).

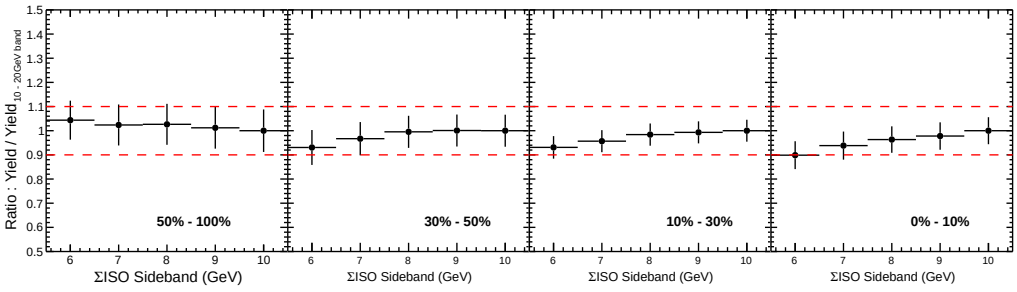

Figure 6.14: Similar study as in the previous Figure 6.18 but now the sideband selection choice was varied. X GeV on the x-axis label means that the sideband was chosen as SumIso of between X GeV and $(X+10)$ GeV.

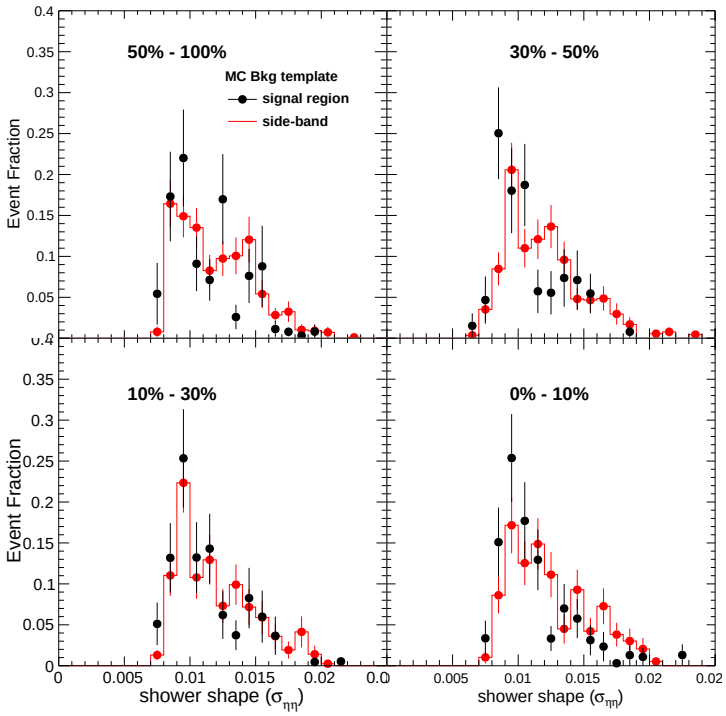

Figure 6.15: Background template comparison in signal region (SumISO < 1 GeV) and sideband region (ISO 10–20 GeV). Em-enriched di-jets events embedded in HYDJET samples were used.

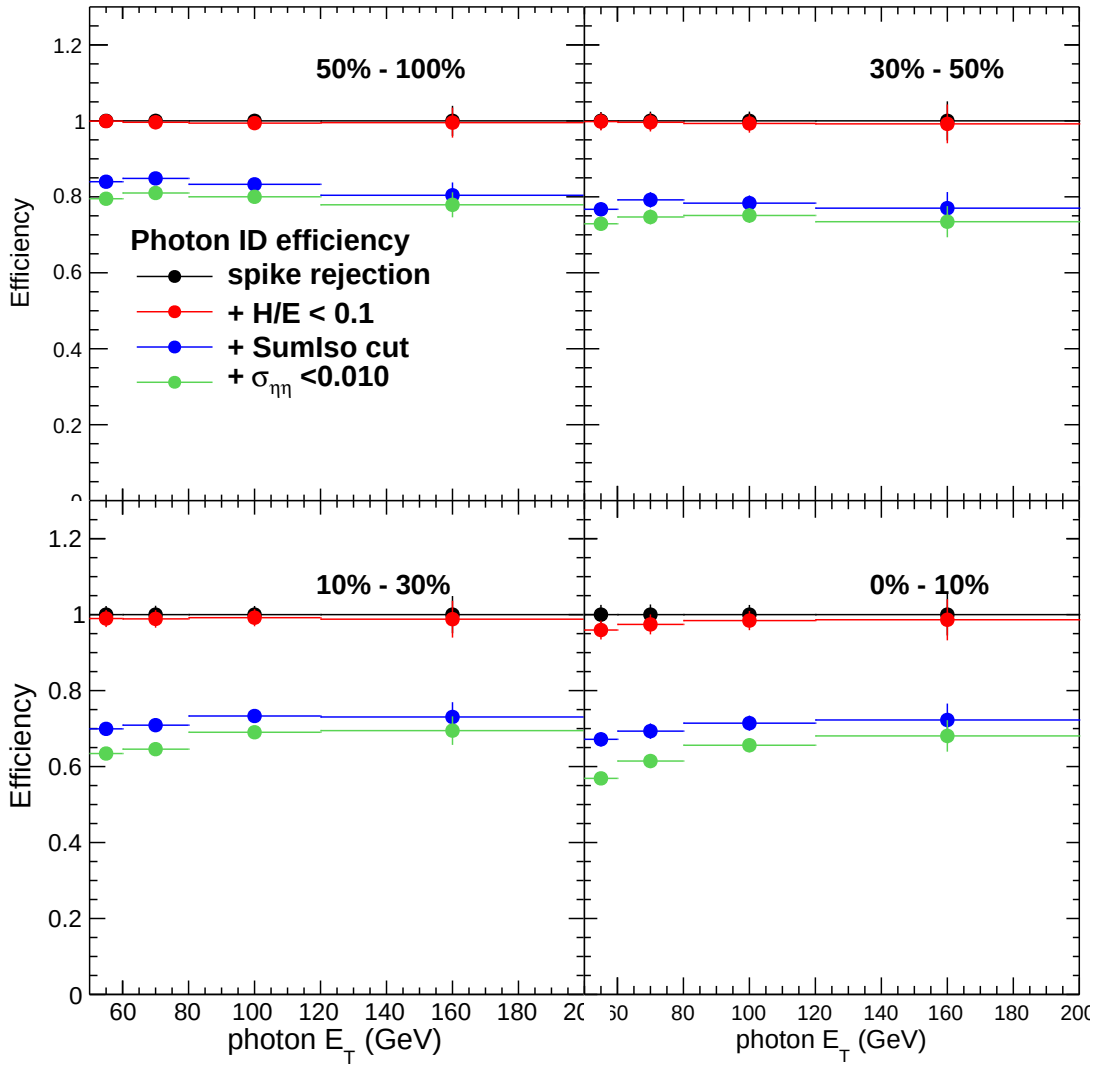

Figure 6.16: Photon identification efficiency using sum isolation method (ISO < 1 GeV)

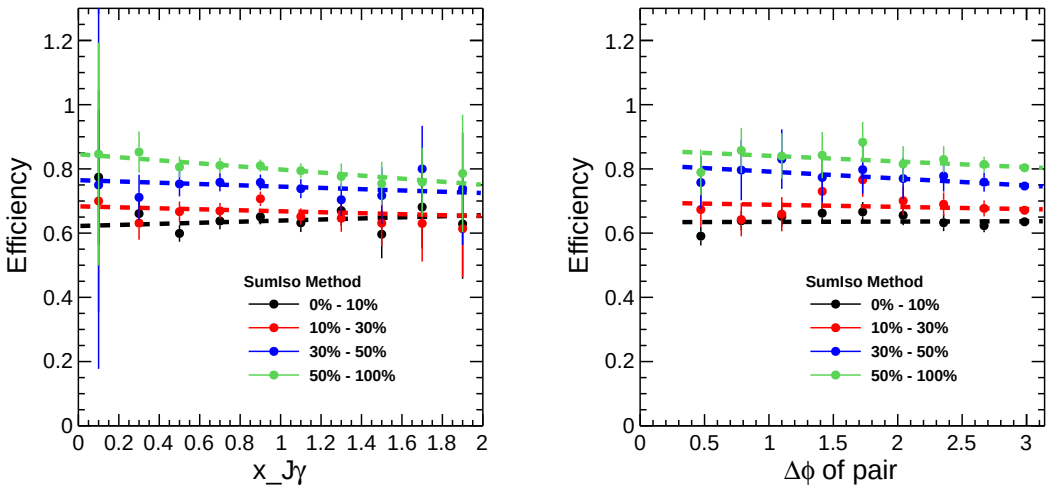

Figure 6.17: Dependence of photon identification efficiency on momentum imbalance and $|\Delta\phi|$ of photon and jet pair.

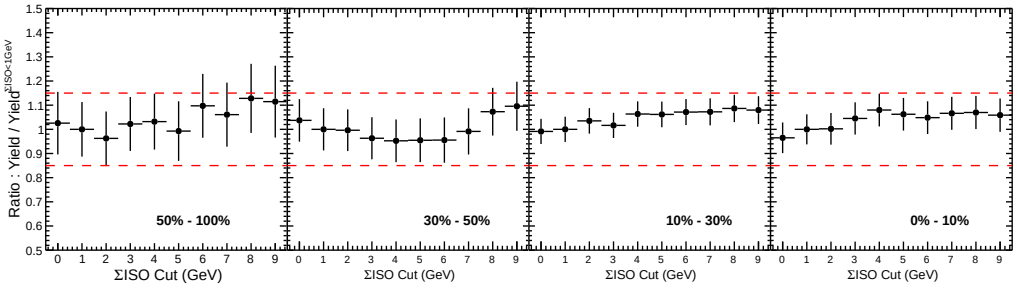

Figure 6.18: Number of inclusive isolated photons above 60 GeV were measured by counting the signals from fitting and then corrected by isolation efficiency. The yields were compared with different isolation cut; 0 GeV (the tightest) though 9 GeV (the loosest), and the maximum deviation of the final yield was 13%.

7 Background Subtraction

Given the collection of photon and jet pairs acquired by the process explained in Sec. 5, one can do various physical measurements such as momentum ratio and angular correlation etc. This is not the end of the story yet. As we called the photon and jet objects as candidates, not signals, there are certain contamination of backgrounds which occupies up to 20% of total candidates, which depends on the centrality. In order to make a genuine measurement, these must be subtracted. There are two kinds of background in this analysis. One is the background jet and the other is background photon. In this section, the source of backgrounds and subtraction techniques will be discussed for jets (in Sec. 7.2) and photons (in Sec. 7.3). First of all, why and how we use a correlation function - statistical description of jet quenching - will be explained in Sec. 7.1.

7.1 Usage of Correlation Function

The relation of the jet and photon in the $\gamma-$jet pairs can not be measured directly event by event for various reasons. In other words, we can not expect a meaningful result from a single $\gamma-$jet event because because there are many kinds of fluctuation affects the result. Instead, the physical message can be extracted from a distribution function of the physics observable. For example, although $\gamma-$jet events are produced in back-to-back manner, they are not exactly 180 degree away each other. Due to the disturbance by soft underlying events which happens in the same nucleon-nucleon collision, their directions are distracted by varying amount. So, it is hard to make a serious conclusion from a single event. Instead, once we make a distribution histogram of the $\Delta\phi$ distribution as shown in Fig. 7.1, we can see the clear trend that photon and jet are LIKELY to be back-to-back. The physics observable in this analysis will be shown in form of distribution function as the example. The probability distribution function of a physics observables like this will be called **correlation function** in this thesis.

A benefit of using correlation function is that the background subtraction is done in linear algebra. Once we have the raw correlation function of an arbitrary variable A of

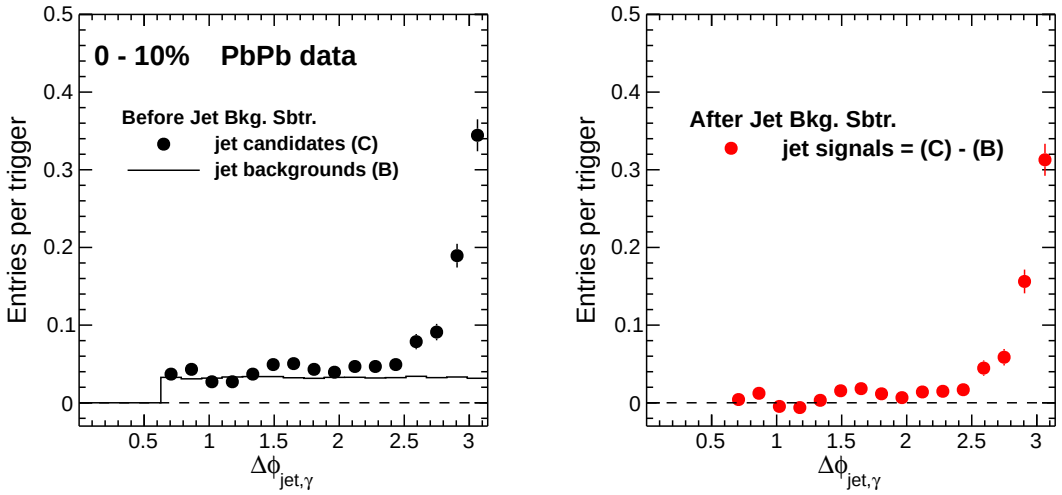

Figure 7.1: Example of background jet subtraction for angular correlation function in PbPb real data. 0-10% central collision events where the background is the biggest were used in this plot. (Left) The raw correlation $\mathrm{Corr}(\Delta\phi)^{\gamma\ \mathrm{cand}}_{\mathrm{jet\ cand}}$ and the estimated background using event mixing $\mathrm{Corr}(\Delta\phi)^{\gamma\ \mathrm{cand}}_{\mathrm{jet\ bkg}}$ were shown. (Right) Correlation functionafter background subtraction. $\mathrm{Corr}(\Delta\phi)^{\gamma\ \mathrm{cand}}_{\mathrm{jet\ sig}}$

$\gamma-$jet candidates, we can discompose it into 4 separate correlation functions.

$$\mathrm{Corr(A)}^{\gamma\ \mathrm{cand}}_{\mathrm{jet\ cand}} = \mathrm{Corr(A)}^{\gamma\ \mathrm{sig}}_{\mathrm{jet\ sig}} + \mathrm{Corr(A)}^{\gamma\ \mathrm{sig}}_{\mathrm{jet\ bkg}} + \mathrm{Corr(A)}^{\gamma\ \mathrm{bkg}}_{\mathrm{jet\ sig}} + \mathrm{Corr(A)}^{\gamma\ \mathrm{bkg}}_{\mathrm{jet\ bkg}} \tag{7.1}$$

,where **bkg** and **sig** stands for background and signal each.

Here we want to extract $\mathrm{Corr(A)}^{\gamma\ \mathrm{sig}}_{\mathrm{jet\ sig}}$ out of $\mathrm{Corr(A)}^{\gamma\ \mathrm{cand}}_{\mathrm{jet\ cand}}$ by subtracting the background terms. Using the background estimation techniques which will be explained in the following sections, the last term$\mathrm{Corr(A)}^{\gamma\ \mathrm{bkg}}_{\mathrm{jet\ bkg}}$ can be obtained directly from data. Other two background terms must be computed from $\mathrm{Corr(A)}^{\gamma\ \mathrm{cand}}_{\mathrm{jet\ bkg}}$ and $\mathrm{Corr(A)}^{\gamma\ \mathrm{bkg}}_{\mathrm{jet\ cand}}$, from the equivalence below.

$$\begin{aligned} \mathrm{Corr(A)}^{\gamma\ \mathrm{cand}}_{\mathrm{jet\ bkg}} &= \mathrm{Corr(A)}^{\gamma\ \mathrm{sig}}_{\mathrm{jet\ bkg}} + \mathrm{Corr(A)}^{\gamma\ \mathrm{bkg}}_{\mathrm{jet\ bkg}}, \\ \mathrm{Corr(A)}^{\gamma\ \mathrm{bkg}}_{\mathrm{jet\ cand}} &= \mathrm{Corr(A)}^{\gamma\ \mathrm{bkg}}_{\mathrm{jet\ sig}} + \mathrm{Corr(A)}^{\gamma\ \mathrm{bkg}}_{\mathrm{jet\ bkg}} \end{aligned} \tag{7.2}$$

By combining Eq. 7.1 and 7.2, we can finally arrive to the correlation of pure signal.

$$\mathrm{Corr(A)}^{\gamma\ \mathrm{sig}}_{\mathrm{jet\ sig}} = \mathrm{Corr(A)}^{\gamma\ \mathrm{cand}}_{\mathrm{jet\ cand}} - \mathrm{Corr(A)}^{\gamma\ \mathrm{cand}}_{\mathrm{jet\ bkg}} - \mathrm{Corr(A)}^{\gamma\ \mathrm{bkg}}_{\mathrm{jet\ cand}} + \mathrm{Corr(A)}^{\gamma\ \mathrm{bkg}}_{\mathrm{jet\ bkg}} \tag{7.3}$$

For the rest of this section, the background subtraction steps will be described in detail using the angular correlation of $\gamma-$jet as an example.

7.2 Subtraction of Background Jets

The background jets come from two different sources. First group are fake jets made by bunches of particles which are accidentally assembled and caught by the jet reconstruction algorithm (See Sec. 5.3.1) . The average multiplicity of charged particles in central PbPb collision is 1600 per pseudo-rapidity unit [87, 88]. This means that if you select a random direction and draw a cone with radius of 0.3 in $\eta \times \phi$ plane then about 100 particles will fall in there in average. In our CMS data, almost every central collision event had at least one fake jet with $p_{\mathrm{T}} > 30$GeV/c in the detector acceptance.

The second group are real jets but their seed partons are not from the same nucleon-nucleon sub-event where the $\gamma-$jet pair that we want to measure. According to the Glauber model [, Miller:2007ri] N_{coll} in central Pb+Pb collision reaches up to 1500. This means that the jet production rate in those events is 1500 times as much as that in pp collision at the same energy.

Typical contamination level by background jets is 10% once after selection of back-to-back $\gamma-$jet pair in central collision events This is not large amount. however, those jets incline toward low p_{T} range because they are made independently from $\gamma-$jet pair. It makes the background jets to be seen as enormously quenched jets when they are paired to high p_{T} photon. Therefore they must be carefully subtracted rather than simply covered by systematic uncertainty.

7.2.1 MinBias Event Mixing Technology

While two kinds of background jets are caused from different origins, they are indistinguishable from the experimental point of view. And, they can be subtracted simultaneously by **MinBias event mixing** technique. In the Glauber model, we assume that the sub-collisions of nucleons in PbPb collision are independent each other and do not exchange information. So, gamma-jet jet scattering by a sub-collision does not affect the production rate of the jets in other sub-collisions in the same event. In other words, if we choose a MinBias event which has same centrality with the one containing the $\gamma-$jet event , then the production rate of fake jets and underlying event jets will be also same. So, once a gamma-jet event is found, a MinBias event with the same event condition -

including vertex and centrality - are searched. Then the number of jets in the matched MinBias events are counted and used as the background estimation. In order to reduce the statistical uncertainty, 20 MinBias events were searched per one $\gamma-$jet containing event and the average number of jets was used for subtraction. Below is the list of criteria used for event matching.

- **Centrality** : Centrality characterize the event size and the impact parameter. 40 centrality bins, which is relatively refined binning, using the sum of energy deposited in HF of forward and backward. Centrality is the most crucial factor which determines the fake jet rates because the particle multiplicity and number of binary collision is strongly correlated to this parameter.

- **Primary vertex position** : There is no correlation between the background jet production with the primary vertex position. However, we need to keep in mind that the detector is not perfect and does not cover 4π angle, so the jet reconstruction is biased by the detector geometry. For example, the jet is not reconstructed if part of particles pass though the gap on the borderline of Barrel and Endcap calorimeter (around $\eta = 1.48$). To avoid this bias, event are classified in 15 vertex bins, in which the bins width is 2cm.

7.2.2 Estimation and Subtraction of Backgrounds

The correlation function of azimuthal angular difference of $\gamma-$jetpair $\Delta\phi_{\gamma,jet}$) will be used as an example for illustration of background jet subtraction. First, we measure the $\Delta\phi$ distribution of $\gamma-$jetc̃andidates, which is $\mathrm{Corr}(\Delta\phi)^{\gamma\ \mathrm{cand}}_{\mathrm{jet\ cand}}$

For each photon triggered event 20 MinBias events which satisfies the matching criteria 7.2.1 are looked for and the jets in those events are searched. Then the $\Delta\phi$ between the photon in photon triggered event and the jets collected from MinBias events are calculated. The correlation function of those mixed events are normalized back by the number of mixing (20) then it essentially represents the background contamination per photon. It becomes statistically equivalent to $\mathrm{Corr}(\Delta\phi)^{\gamma\ \mathrm{cand}}_{\mathrm{jet\ bkg}}$. Now, if this is subtracted from the jet candidate correlation function, we can have

$$\mathrm{Corr}(\Delta\phi)^{\gamma\ \mathrm{cand}}_{\mathrm{jet\ sig}} = \mathrm{Corr}(\Delta\phi)^{\gamma\ \mathrm{cand}}_{\mathrm{jet\ cand}} - \mathrm{Corr}(\Delta\phi)^{\gamma\ \mathrm{cand}}_{\mathrm{jet\ bkg}} \tag{7.4}$$

,where background jets are cleaned off. The jet background component of $\Delta\phi$ correlation function is shown as the green points in the example Fig. 7.1. It is flat function because

the jet background does not have any correlation to the photon in the matched event. The red points are the signal distribution after the background subtraction. As we expected, the correlation function peaks at $\Delta\phi=\pi$ and asymptotically disappears around $\Delta\phi=\frac{\pi}{2}$, which means that the back-to-back nature of $\gamma-$jetpair is restored by successful background subtraction.

The same process is done to subtract the background jets paired to *background* photons in order to obtain

$$\mathrm{Corr}(\Delta\phi)^{\gamma\ \mathrm{bkg}}_{\mathrm{jet\ sig}} = \mathrm{Corr}(\Delta\phi)^{\gamma\ \mathrm{bkg}}_{\mathrm{jet\ cand}} - \mathrm{Corr}(\Delta\phi)^{\gamma\ \mathrm{cand}}_{\mathrm{jet\ bkg}} \tag{7.5}$$

Discussions about background photon will continue in Sec. 7.3.

7.2.3 Inclusive Jet Better than leading Jet

One ambiguous situation is that the signal and background jet are found in the same event. If two jets are found in the away-side of photon direction, which one should be paired to the trigger photon? We do not know which one is signal or background. Perhaps, both of them may be background jets. Someone may prefer to select the high p_{T} jet, which is called **leading jet analysis**. But, for this analysis, both of them are paired to the photon and goes into the correlation function calculation. In other words, the photon is re-used in multiple jet event. This is called **inclusive jet analysis**.

By using the inclusive jet method, we can statistically subtract the background jets while keeping the signal jets whose energy is accidentally smaller than the accompanying background jets. Although sometimes there are two signal jets recoiled by photon, similar to the three-jet events, but this is more tolerable in terms of theory comparison. Comparison of the leading jet method and inclusive jet method is summarized in Table. 7.1.

	Inclusive jet analysis	leading jet analysis
Method	Correlate leading photon with leading jet on the away-side	Correlate leading photon with all the jets found away side
Background subtraction	Model dependent	Easy
γ - double jet event	Only higher p_{T}jet selected	Both jets are selected and contribute correlation twice

Table 7.1: Coefficients for the Fisher discriminant.

7.3 Subtraction of Background Photons

7.3.1 Finding Pure Background Photons from Sideband

After isolation cut and shower shape cut, the purity of photon candidates is 75% - 90% (Sec. 6.3) depending on the centrality. This means that the direct photon occupies 75%-90% of candidate collection and the rest 10% - 25% comes from background. The main source of background is high p_{T} π^0 which is very hardly radiated from parton. This parton becomes a jet, but most of its energy is concentrated into a single π^0, so it pretends to be an isolated photon.

The background photon distribution can be estimated using **shower shape sideband** method. The sideband designates the photon super-clusters in the range of $0.011 < \sigma_{\eta\eta} < 0.018$ where the background photon is predominant. In Fig. 6.2, the sideband area is full of green components (background) for all centrality events. Hence, $\mathrm{Corr}(\Delta\phi)^{\gamma\ \mathrm{bkg}}_{\mathrm{jetcand}}$ can be obtained by pairing the sideband photons to jets. Before moving to the actual subtraction step, the (background jet) $\times$ (background photon) pair is subtracted as mentioned in Eq. 7.5.

7.3.2 Signal Extraction

From the purity calculated in Sec. 6, we know that the raw correlation function is a linear composition of signal and background by ratio of purity.

$$\mathrm{Corr}_{\mathrm{candidate}} = \mathrm{purity} \times \mathrm{Corr}_{\mathrm{signal}} + (1 - \mathrm{purity}) \times \mathrm{Corr}_{\mathrm{background}} \tag{7.6}$$

It is not hard to modify this equation into

$$\mathrm{Corr}_{\mathrm{signal}} = \frac{\mathrm{Corr}_{\mathrm{candidate}} - (1 - \mathrm{purity}) \times \mathrm{Corr}_{\mathrm{background}}}{\mathrm{purity}} \tag{7.7}$$

So, we can get the final signal correlation function based on the two terms on the RHS which was obtained in the previous sections.

For ease of understanding, 7.2 is an example step for measuring the transverse momentum correlation of photon-jet. Using this method the correlation of momentum ratio and angular correlation between photon and jets were analyzed.

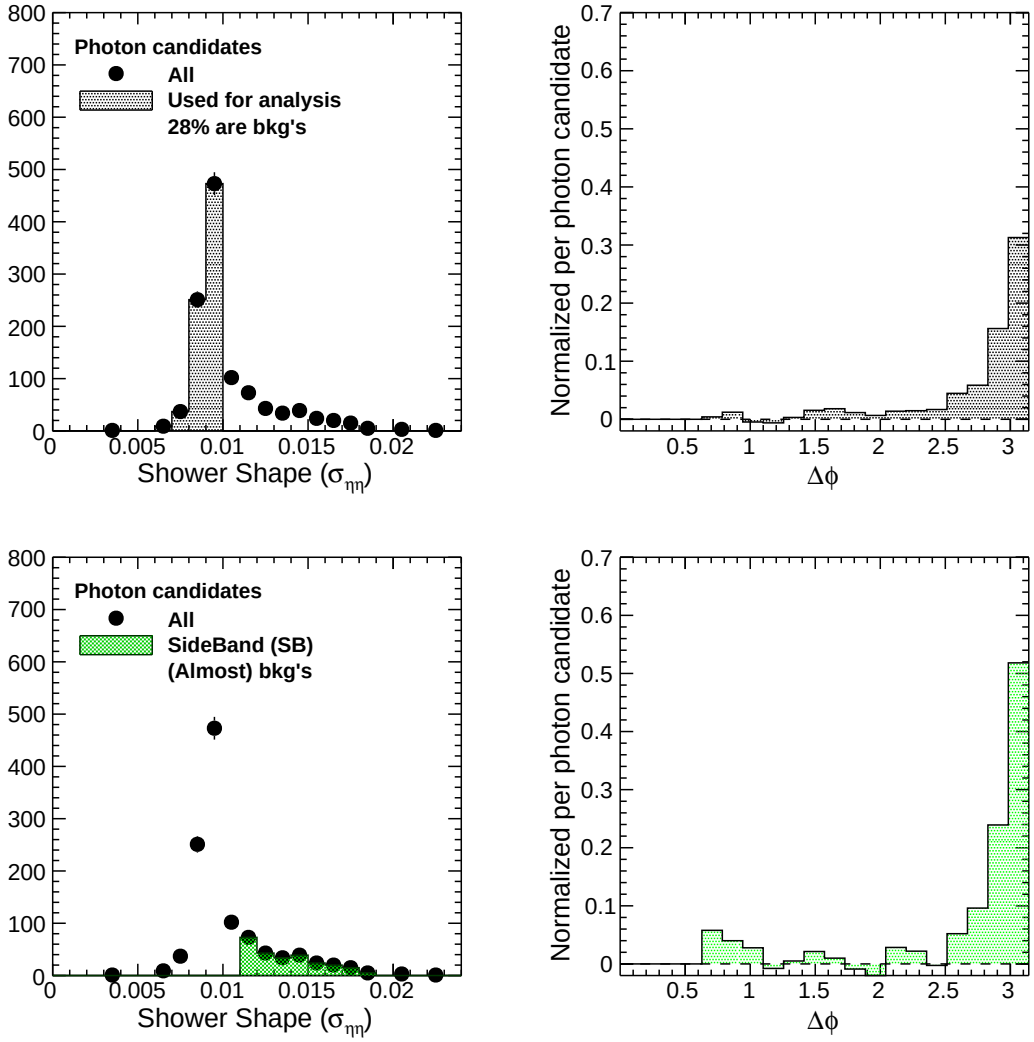

Figure 7.2: Illustration of photon background subtraction. This is continued by the following figure, Fig. 7.3

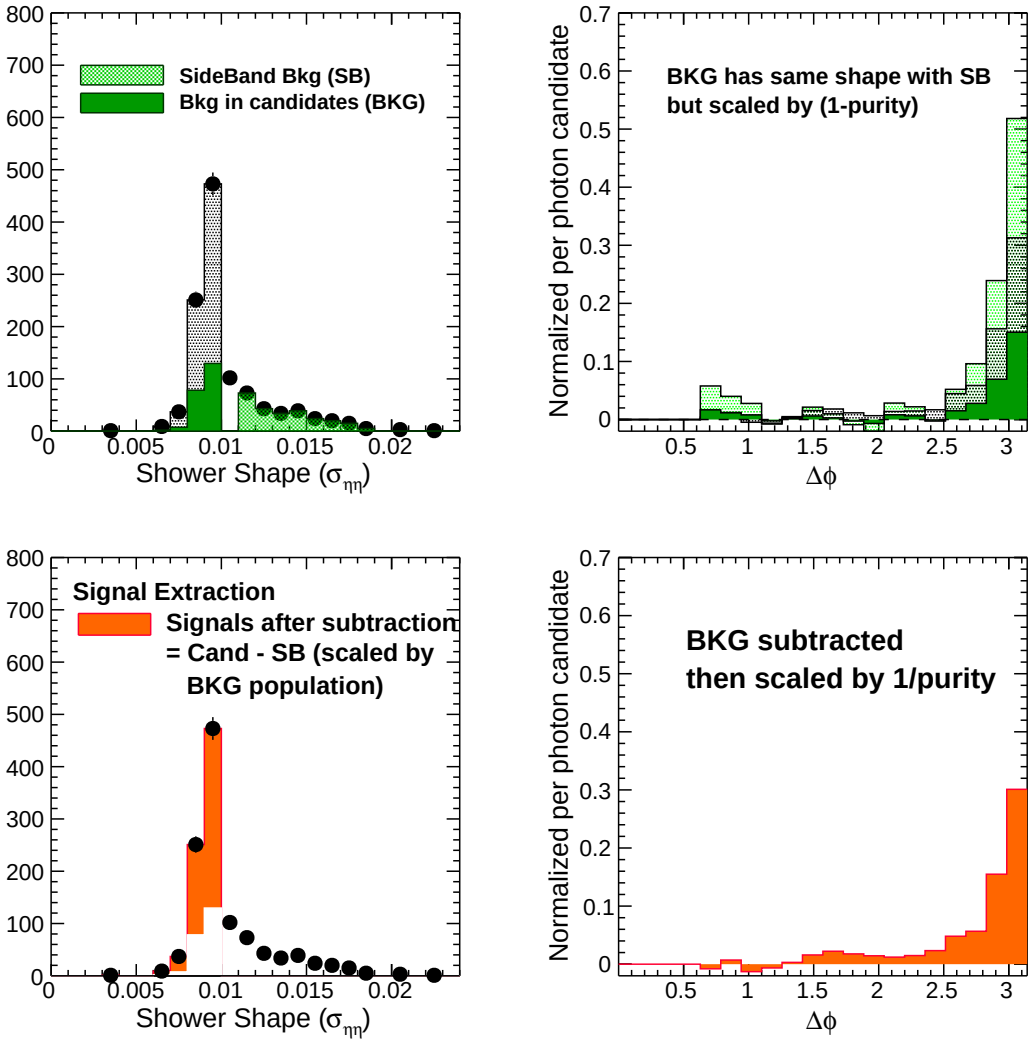

Figure 7.3: Illustration of photon background subtraction.

8 Observation of Jet Quenching

The ideal way to measure the jet quenching phenomena would be to tag a single quark and videotape the motion during its propagation though QGP. However, that is prohibited bythe uncertainty principle. In technical point of view another difficulty is that we can not distinguish the signals form fake photons and jets event-by-event. This situation inspired the statistical background subtraction algorithm(Sec. 6.3). Therefore, the final results will be shown by the probability distribution of kinematic relations between photon and jet, which is called **correlation functions**.

The pp collision data was also analyzed to study the phenomenology of $\gamma-$jet scatterings produced in vacuum. The results were used as the reference to be compared with PbPb data in order to highlight the jet quenching effects. Originally, the MC simulated events using PYTHIA+HYDJET played the role of reference because we had not had enough statistics of pp collisions ($L = 231 nb^{-1}$). However, in the middle of writing this dissertation on March, the LHC delivered 20 times more pp collisions which contains similar number of $\gamma-$jet pairs in PbPb data. Therefore, the pp data replaced the MC reference, and this chapter was updated accordingly. Yet, the MC simulation results are still useful in many aspects, such as validation of the background subtraction algorithm. In Sec. 8.1, the results of pp collisions and MC simulation will be shown together. Although the MC sample was simulated in PbPb underlying events, the $\gamma-$jet signals in this sample were not quenched. Therefore, the signals' kinematic nature is closer to pp collisions. Also, we will see that the results of MC analysis do not depend on the centrality, which means that the background subtraction tool is robust against the background fluctuation in overal centrality intervals. In Sec. 8.2, the PbPb data and pp data will be directly compared.

Three observables were developed to appraise the jet quenching effects. One is the angular correlation ($\Delta\phi_{J\gamma}$) and characterizes the back-to-back nature of $\gamma-$jetpairs. The others are $x_{J\gamma}$ and $R_{J\gamma}$, which directly measure the energy loss of jets and jet disappearance rate respectively.

8.1 Study of $\gamma-$jet Produced in Vacuum Using pp Data and MC Closure Test

In general, the energy of a jet is smaller than the original parton energy because a non-negligible amount of the parton energy leaks out of the cone. Therefore, even if we select the $\gamma-$jetpair without any ISR (initial state radiation) or FSR (final state radiation), their momenta would not be completely balanced. This can result in the similar effect with jet quenching, which we can not distinguish event-by-event. In order to separate the jet quenching effect (signal) from the jet cone bias (background), we must measure the same $\gamma-$jetevents produced in vacuum in which the jet quenching effect is missing. This is the reason of using the pp collisions as the reference to be compared with the PbPb data.

In the meanwhile, the analysis of MC simulation was carried out for validation of the background subtraction algorithms, particularly the background jets which is the first category in Sec. 7. The PYTHIA+HYDJET simulation provides the $\gamma-$jet events overlaid on the PbPb underlying events while leaving the jets unmodified (Sec. 4.3). Therefore, if the background jets were properly subtracted by the subtraction methods described in Sec. 7, the results of MC analysis must be consistent regardless of the multiplicity of background particles. This sort of validation process is called *MC closure test*.

In order to make the $\gamma-$jet kinematics in MC simulation close to the real data, a specially tuned PYTHIA (Z2 tune) was used [72]. PYTHIA was adjusted to agree with various QCD results in pp collisions at 7TeV measured by LHC experiments. By going through the MC results in this section, we will check if our background subtraction sequences are robust enough so it is not biased by the fluctuation of background energy.

8.1.1 N_{part} and Centrality

The analysis were done in 4 collisional centrality bins - 0-10%, 10-30%, 30-50% and 50-100%. As discussed in Sec. 5.1.1, the centrality relates to the energy density and the size of the medium produced by the collisions. So the centrality dependence of a physics observable can be an evidence that it is related to the path length though the medium. For some of the figures (Fig 8.2 - Fig. 8.12), the N_{part} was used instead of the percentile numbers because N_{part} is more intuitive parameter to characterize the medium size. According to the Glauber calculation [48, 89], the average N_{part} values of PbPb collisions are 43.7 (50-100%), 116.4 (30-50%), 235.8 (10-30%) and 359.2 (0-10%). Obviously, the

$N_{\rm part}$ of pp collisions is 2.

8.1.2 Angular Correlation : $\Delta\phi_{J\gamma}$

Angular correlation between photon and jet is one of the major observables to directly measure the jet quenching parameter that was described in Sec. 2.2. QCD calculation predicts that the medium-induced gluon radiation is not collinear as much as the case of fragmentation in vacuum [30]. So, the direction of jet may be distracted by recoiling of radiated gluons and then the back-to-back nature of $\gamma-$jet pairs may be blunt. The spatial angle between the jet axis and photon in the reference frame of lab can not give the best information because we do not know the pre-scattering momenta of partons. In other words, we do not know how much the center of mass was boosted in z-axis. Instead, the azimuthal angle $\Delta\phi_{J\gamma}$was used by virtue of its Lorentz invariance.

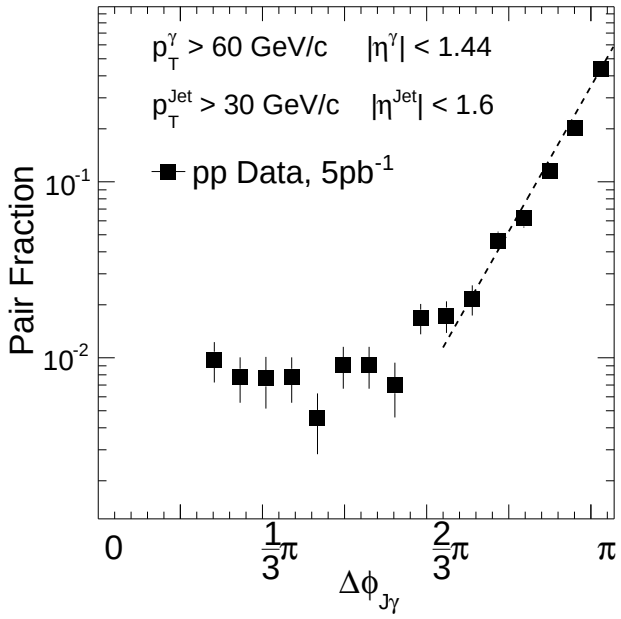

Figure 8.1: $\Delta\phi_{J\gamma}$ distribution of $\gamma-$jet pairs of pp collisions. The tail part, $\Delta\phi_{J\gamma} > 2\pi/3$, was fitted by Eq.8.1 to quantify the back-to-back nature (dashed lines). The histogram was normalized by the total number of $\gamma-$jetpairs.

The result of pp data is shown in Fig 8.1. The sharp peak around $\Delta\phi = \pi$ means that the $\gamma-$jetpairs tend to be produced in back-to-back for the sake of momentum conservation. Since the incoming beams are along z-axis, the total transverse momentum must be zero. Yet, some fraction of $\gamma-$jetpairs are scattered not exactly back-to-back

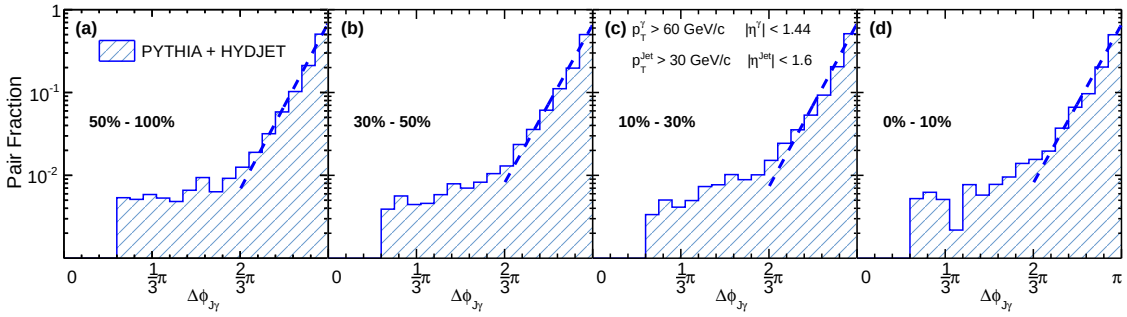

Figure 8.2: $\Delta\phi_{J\gamma}$ distribution of $\gamma-$jet pairs of PYTHIA+HYDJET simulation. The events were divided into 4 centrality intervals in order to inspect possible bias by background subtraction algorithm. The tail parts, $\Delta\phi_{J\gamma} > 2\pi/3$, were fitted by Eq.8.1 to quantify the back-to-back nature (dashed lines). The histograms were normalized by the total number of $\gamma-$jetpairs.

because there is finite possibility that gluons or photons can be radiated at the initial state (ISR) or after the scattering (FSR). This feature is common for pp and PbPb collisions. Shown in logarithmic scale, the tail part of this histogram seems to be increasing linearly. So, that range was fitted by a simple exponential function,

$$f(\Delta\phi) = Ae^{\frac{(\pi-\phi)}{\sigma}}, \quad (\frac{2\pi}{3} < \Delta\phi < \pi) \tag{8.1}$$

in order to extract the width(σ). The dashed line in the same figure (Fig. 8.1) shows the performance of fitting. The σ of pp collisions was calculated to be 0.26.

Fig. 8.2 shows the distribution of $\Delta\phi_{J\gamma}$ of PbPb MC samples and their fitting with 8.1 (dashed lines). The results were overlaid by the real pp data results. All the histograms are consistent with the pp data within uncertainty.

For more quantitative comparison, the widths of fitting curves were compared. In Fig 8.3, the σ value of simulated events is slightly smaller than the real pp data. However, it does not necessarily mean that the simulation is useless for this analysis. The important point is that the results of PYTHIA+HYDJET is flat for all centrality and consistent with PYTHIA (σ around 0.23). This convinces us that the background subtraction was done properly and $\Delta\phi_{J\gamma}$ is a robust observable against the fluctuation of background energy by underlying events.

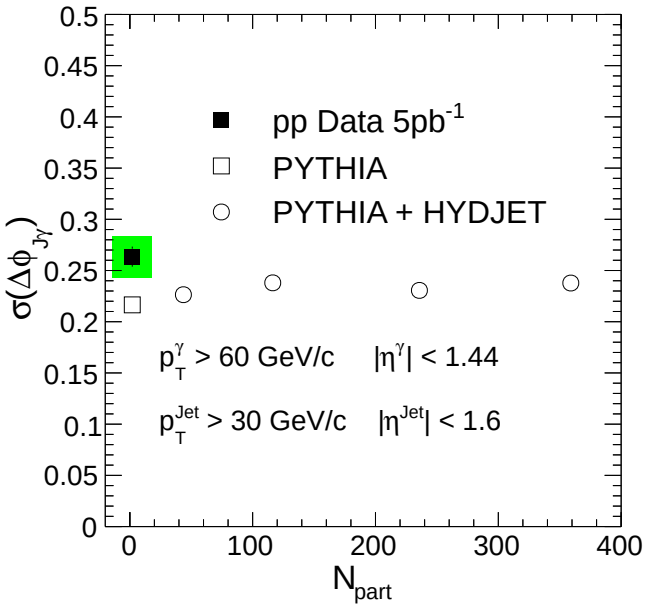

Figure 8.3: The widths of $\Delta\phi_{J\gamma}$ distributions of real pp collisions (Fig. 8.1) at $N_{\rm part}$= 2, and those of MC simulated events using PYTHIA+HYDJET (8.2) at higher $N_{\rm part}$ bins. The width of pp data deviates from MC expectation. But, important fact is that PYTHIA+HYDJET values are consistent each other for all centrality bins. This implies that this observable is not biased by fluctuation of underlying events.

8.1.3 Jet Finding Rate : $R_{J\gamma}$

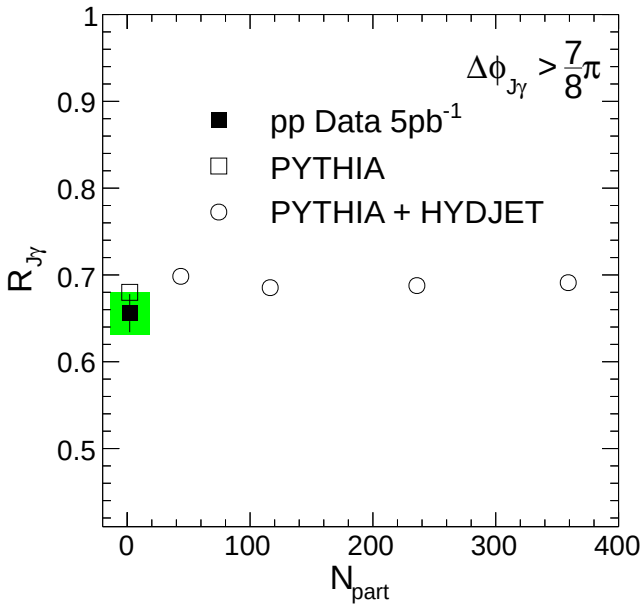

Figure 8.4: $R_{J\gamma}$ represents the probability to find the jet partners in away side ($\Delta\phi > \frac{7\pi}{8}$) per triggered photon. The plot shows the results of real pp collisions, simulated pp events by PYTHIA ($N_{\rm part} = 2$) and simulated PbPb events by PYTHIA+HYDJET (higher $N_{\rm part}$bins). $R_{J\gamma}$ of PYTHIA is consistent with data within uncertainty. The PYTHIA+HYDJET results are all consistent with PYTHIA, which implies that the background jet subtraction was done correctly.

The second physics observable we expect to find is the enhancement of mono-photon events, in which the associated jet partners are disappeared. Since we reconstructed only the jets with $p_{\rm T}$ above 30GeV/c for this analysis (See Sec. 5.3 for the reason), we are blind of jets below this threshold. So, the mono-photon events does not necessarily mean that the jet has been completely disappeared. More precise explanation is that the jets were submerged below the examination range due to the jet quenching.

In order to suppress the background jet rates below 10 % level, a narrow angular range $\Delta\phi_{J\gamma} > \frac{7\pi}{8}$ was used for the $\gamma-$jet event selection. Although all the background jets are subtracted in the final results, higher signal purity assures less systematic uncertainty.

The probability of finding a jet partner was quantified as

$$\mathsf{R}_{J\gamma} = \frac{\text{Number of associated jets}}{\text{Number of triggering } \gamma\text{'s}} \tag{8.2}$$

As shown in Fig. 8.4, the $\mathsf{R}_{J\gamma}$ of pp data was 0.66. This means that the jet partners were not reconstructed for 34% of the total photon events. The plot also shows the results of PYTHIA events which have consistent $\mathsf{R}_{J\gamma}$ with pp data.

At the beginning of this analysis, there was a concern for this measurement because of the possible bias by the centrality dependent jet energy resolution. In higher central events, the background energy fluctuation is larger, so the jet energy resolution becomes worse. We can expect that a jet having (real)p_{T} below the threshold (30GeV/c) can possibly be reconstructed with help of background fluctuation. Or, in the other way around, the jets having (real) p_{T} slightly above 30GeV/c may cross below the threshold and then may not be reconstructed.

But, the simulation using PYTHIA+HYDJET proved that such bias is negligible by showing that the $\mathsf{R}_{J\gamma}$ values for all centrality bins are consistent with PYTHIA events as demonstrated in Fig. 8.4. This implies that the subtraction of background jets was correctly and the $\mathsf{R}_{J\gamma}$ measurement is robust to the energy fluctuation by underlying events.

8.1.4 Transverse Momentum Ratio : $\mathsf{x}_{J\gamma}$

The last physics observable to be introduced is the momentum ratio of jet to photon, which is defined as below.

$$\mathsf{x}_{J\gamma} \equiv \frac{p_T^{jet}}{p_T^{\gamma}}. \tag{8.3}$$

$\mathsf{x}_{J\gamma}$ provides the intuitive measurement of the energy loss via medium because the denominator (photon p_{T}) supplies the initial state energy of the parton and the numerator (jet p_{T}) designates the final state energy after jet quenching. The same $\Delta\phi$requirement and centrality binning used in Sec. 8.1.3 were applied again.

The distribution of $\mathsf{x}_{J\gamma}$ of pp collisions and simulated PbPb events are shown in Figure 8.5. The same pp histograms were repeatedly overlaid on PYTHIA+HYDJET results for comparison. As mentioned at the beginning of this section. a $\gamma-$jet partner does not have exactly same transverse momentum. If it were true, the $\mathsf{x}_{J\gamma}$ distribution must be a delta function with a sharp peak at 1. In reality, the $\mathsf{x}_{J\gamma}$ distribution has a peak around 0.8 which means that only 80% of the total parton energy was reconstructed by the jet

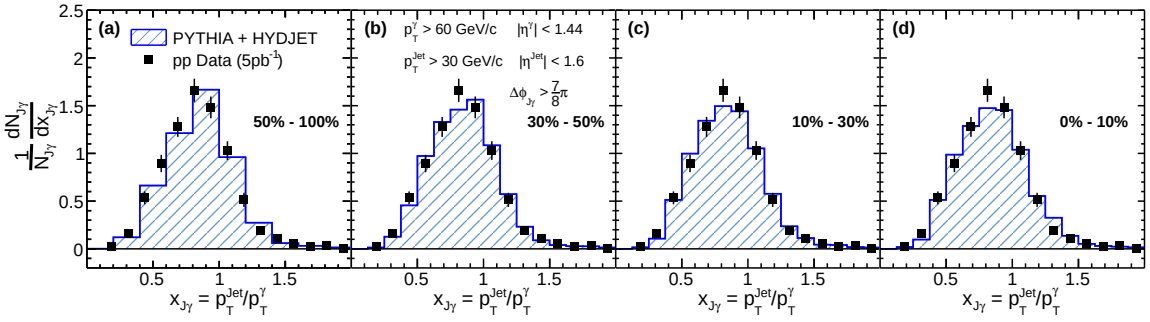

Figure 8.5: The distributions of momentum ratio, $x_{J\gamma}$ ($= \frac{p_T^{jet}}{p_T^{\gamma}}$), of pp real data and PbPb MC events simulated by PYTHIA+HYDJET. In this figure, the pp histogram was overlaid on top of MC PbPb results in 4 centrality bins for comparison. MC and data are consistent within uncertainty.

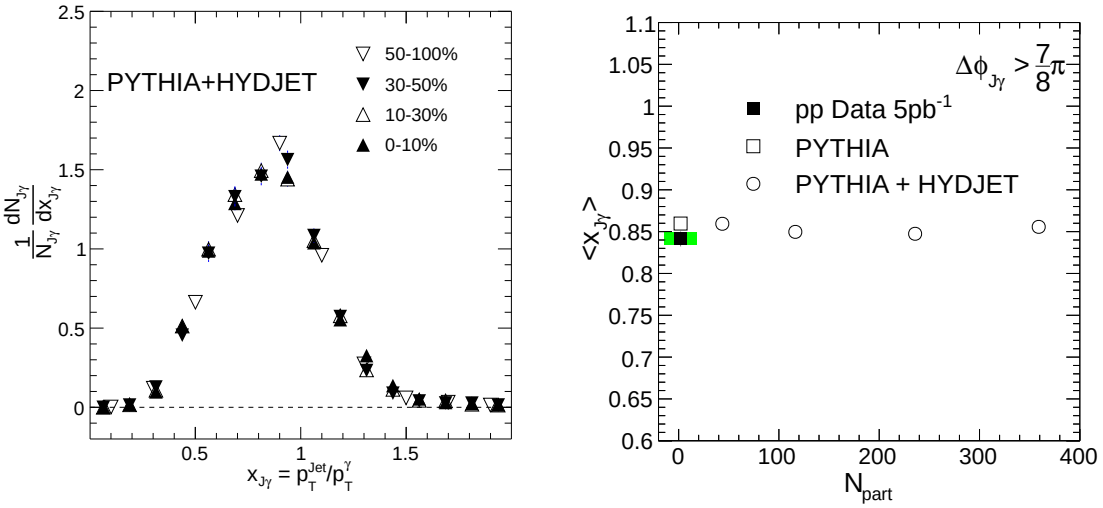

Figure 8.6: (Left) Four $x_{J\gamma}$ distributions in Fig. 8.5 are overlapped for comparison. No significant discrepancy appears. (Right) average value of $x_{J\gamma}$ in pp data and PbPb MC simulation. They are all consistent with each other having falt vale at 0.85. It means that 85% of the initial parton energy is fragmented into the jet cone was caught by the jet clustering algorithm. Note that the jet resolution parameter (or jet cone radius) was R = 0.3.

reconstruction algorithm. Also, the distribution is broad and the tails span from 0.3 to 2. The small $x_{J\gamma}$ tail is thought to be made by the occasional gluon radiation at large angle. And the large $x_{J\gamma}$ tail can be though to be made by the events in which the isolated photons were originated from the parton fragmentation, so its momentum is largely smaller than the recoiled jet up to by factor of 2. In the Fig. 8.5, the $x_{J\gamma}$ distributions of PYTHIA+HYDJET are consistent with pp reference for all centrality intervals. They were also overlaid each other on the left-hand side of Fig. 8.6 and they overlap well. This means that $x_{J\gamma}$ is another good measurement of jet quenching which is not biased by the energy fluctuation of the underlying events.

In addition, the mean value of $x_{J\gamma}$, $<x_{J\gamma}>$ was computed and summarized on the right-hand side of Fig. 8.6. The $<x_{J\gamma}>$ of pp data was slightly lower than PYTHIA simulation, but more importantly the HYDJET+PYTHIA results have consistent $<x_{J\gamma}>$ with PYTHIA.

8.2 $\gamma-$jet Phenomenology Observed in PbPb Collisions

The same three $\gamma-$jet correlation observables - $\Delta\phi_{J\gamma}$, $x_{J\gamma}$ and $R_{J\gamma}$ were measured for the PbPb collisions and compared to the pp reference. If the hot and dense medium made by the PbPb collision modified the jets in $\gamma-$jet scatterings, the correlation results will be deviated from the pp reference. If the magnitude of jet quenching relies on the parton' path length though the hot and dense medium, it will be manifested by the centrality dependence of the results.

8.2.1 Angular Correlation : $\Delta\phi_{J\gamma}$

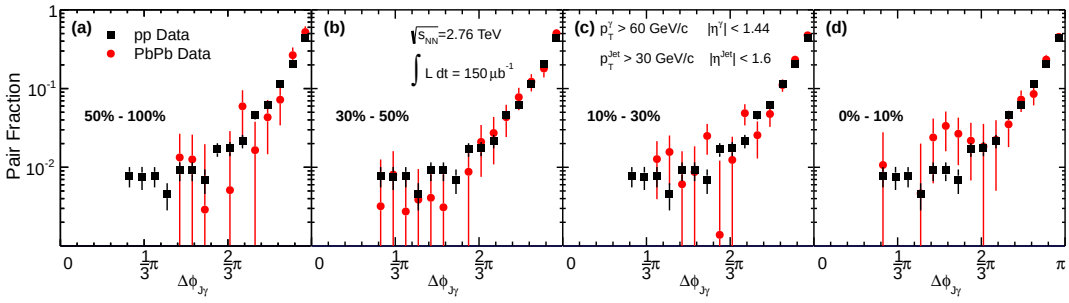

Figure 8.7: The distributions of $\Delta\phi_{J\gamma}$õf PbPb data in the 4 centrality intervals were compared to pp reference which has been shown in Fig. 8.2. No remarkable difference was observed for all centrality bins.

In Fig. 8.7, the $\Delta\phi_{J\gamma}$ distribution of PbPb collisions was measured in 4 centrality intervals and overlaid on the pp result which was shown in Fig. 8.1. All 4 histograms are well overlapped with the pp result within statistical uncertainty. For the better quantitative comparison, the tail parts were fitted by the Eq. 8.1 to extract the width σ (Fig 8.8). The widths of the PbPb data in all centrality bins are summarized in Fig. 8.9. As shown in this figure, PbPb results are consistent with pp within uncertainty. This outcome indicates that there was no significant diversion of the parton's direction.

8.2.2 Jet Finding Rate : $R_{J\gamma}$

$R_{J\gamma}$, which is the probability of finding jet partner for an isolated photon, was measured for PbPb data. In Fig. 8.10, the results were summarized and plotted on top of the pp reference (Fig. 8.4). With the naked eyes, we can tell that the result of PbPb collisions is clearly different from the pp reference. The $R_{J\gamma}$ in the most central PbPb collisions

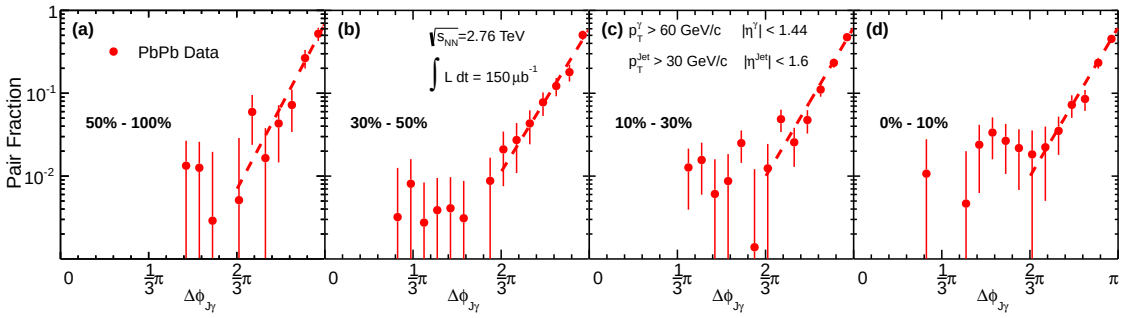

Figure 8.8: The tail parts, $\Delta\phi_{J\gamma} > 2\pi/3$, were fitted by Eq.8.1 to quantify the back-to-back nature (dashed lines).

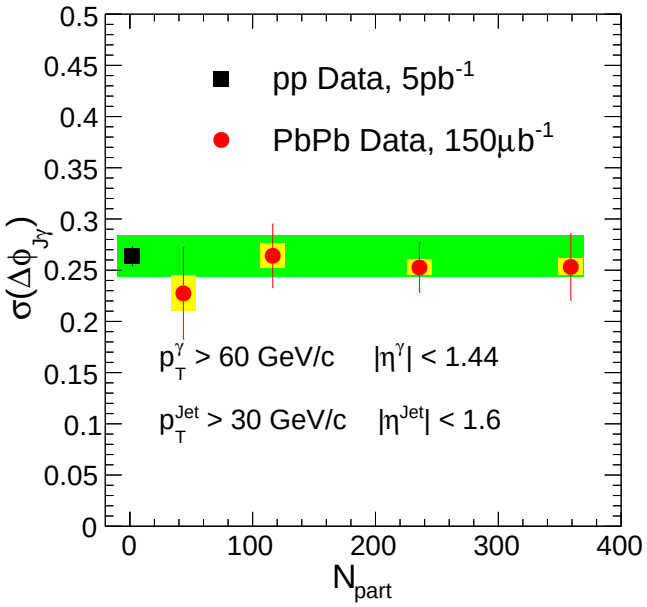

Figure 8.9: The widths of $\Delta\phi_{J\gamma}$ fit functions in Fig. 8.8 were summarized and compared with the pp collision reference which was already shown in Fig. 8.3. The widths are consistent with each other and flat 0.25 within uncertainty. The green band around the pp result means the systematic uncertainty which will be mentioned in Sec. 8.2.4. This phenomenon implies that the direction of high p_T parton was not significantly distracted by the hot and dense medium.

is smaller by 0.17 than that of pp collisions. This means that the production rate of mono-photon events was increased by 17% as the associated jets lost their energy and submerged below 30GeV/c cut-off. More interesting is that the discrepancy gradually increases along the N_{part} value (or centrality). This is a very direct evidence of the jet quenching phenomenon.

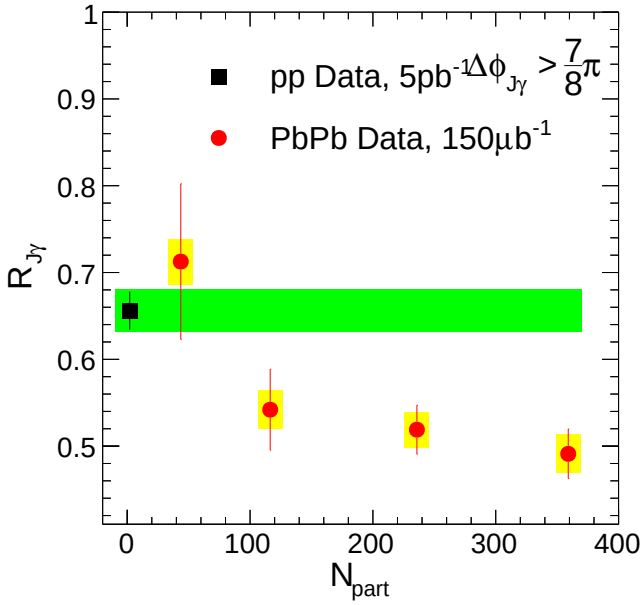

Figure 8.10: $R_{J\gamma}$ of the PbPb collisions was calculated and compared with pp reference which was shown in Fig. 8.4. The green band around the pp result means the systematic uncertainty which will be mentioned in Sec. 8.2.4. One can see that the $R_{J\gamma}$ gradually decreases for we moves to higher N_{part}bins. In the most central collision interval, or high N_{part} , the mono-photon events were increased by 17% which indicates that the energy loss pulled down the p_{T} of those jets below the 30GeV threshold.

8.2.3 Transverse Momentum Ratio : $x_{J\gamma}$

$x_{J\gamma}$, the ratio of jet p_{T} to photon p_{T} was measured in 4 centrality intervals. The Fig. 8.11 shows the distributions of $x_{J\gamma}$ overlaid on the pp reference which has been shown in Fig. 8.5. The results exhibits the gradual shift of the distribution shape towards lower $x_{J\gamma}$ value for higher centrality collisions. In order to quantitatively analyze this phenomenon, the average of $x_{J\gamma}$, $<x_{J\gamma}>$, was again computed as we have done for pp reference in the previous section (See Fig. 8.6). The results are summarized in Fig 8.12. For

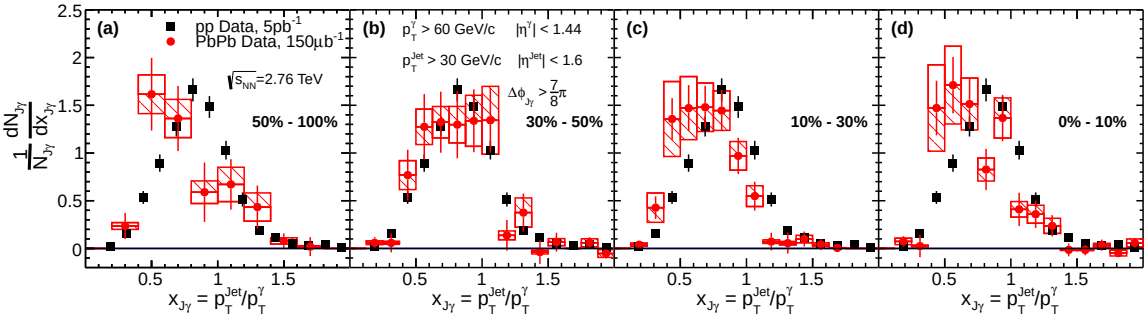

Figure 8.11: The distribution of $x_{J\gamma}$, the p_T ratio of jet to photon, in four centrality bins. The results of PbPb data were compared to the pp reference which was already shown in Fig. 8.5. All histograms were normalized by their areas. We can see that the distribution in data is shifted to left compared to the pp reference and the discrepancy gradually increases by collision centrality.

the two highest centrality bins (0-10% and 10%-30%), the PbPb data have significantly lower $<x_{J\gamma}>$ than the pp reference. In the most central collisions, $<x_{J\gamma}>$ is 0.14 lower than the pp reference, which means that the hot and dense medium took 14% of the initial parton energy from the jet.

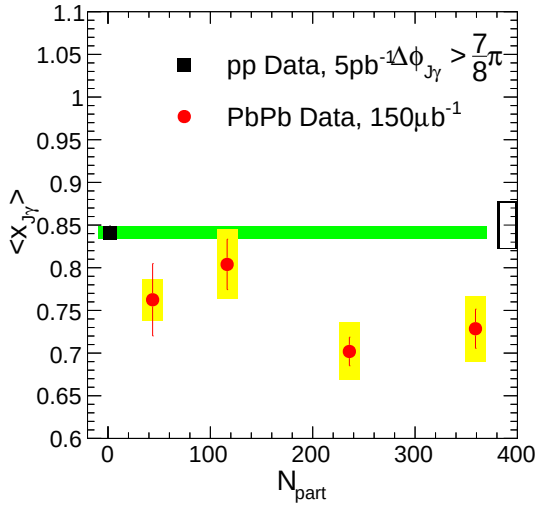

Figure 8.12: The mean values of $x_{J\gamma}$'s in Fig. 8.11. The PbPb data points were compared to the pp reference (Fig. 8.6). The green band around the pp result represents the systematic uncertainty (Sec. 8.2.4). We can clearly see the drop of $x_{J\gamma}$ in the highest two N_{part} bins, which correspond to 0-10% and 10-30% centrality intervals.

8.2.4 Systematic Uncertainty Estimation

There are several sources of the systematic uncertainty in this analysis. Photon purity, isolation criteria and electron contamination are made by photon measurement. In addition, the uncertainty by fake jets, jet energy scale and resolution are attributed to the jet measurement.

The uncertainty in the energy scale consists of four main contributions. The first one comes from the 2% relative uncertainty of the jet energy scale [**?**]. The second contribution is the data-to-MC energy scale difference observed in 7TeV pp collisions which is another 2%. Thirdly, the additional uncertainty for the jet energy scale in the presence of the underlying events is estimated to be 3% for the 30–100% and 4% for the 0–30% centrality range, using the PYTHIA+HYDJET events. The last contribution is the effect of heavy ion background on the ECAL energy scale, which is determined from $Z \rightarrow e^+e^-$ mass reconstruction. This results in a relative uncertainty of 1.5%, comparable to the pp uncertainty (obtained via π^0 and $\eta \rightarrow \gamma+\gamma$).

The uncertainty of the photon purity was estimated to be 18% as described in Sec. 6.4. Systematic effects due to photon reconstruction efficiency are estimated by correcting the data using the efficiency derived from the MC simulation, and comparing the result with the uncorrected distribution. The contribution of non-isolated photons (mostly from jet fragmentation) that are mistakenly determined to be isolated in the detector due to underlying event energy fluctuations or detector resolution effects is estimated using PYTHIA+HYDJET simulation. The difference of $\gamma-$jetobservables obtained from MC truth and reconstructed pairs is taken to be the systematic uncertainty resulting from the experimental criterion for an isolated photon.

The effect of inefficiencies in the jet finding, especially in low p_{T} range, is estimated by repeating the analysis after re-weighting each jet with the inverse of the jet finding efficiency as a function of the jet p_{T} which was determined from PYTHIA+HYDJET simulation.

The uncertainties quoted to the three observables ($\Delta\phi_{J\gamma}$, $\mathsf{x}_{J\gamma}$, $\mathsf{R}_{J\gamma}$) are summarized in Tables 8.1, 8.2 and 8.3 respectively.

Table 8.1: Relative systematic uncertainties for $\sigma(\Delta\phi_{J\gamma})$ for pp data and each of the PbPb centrality bins.

Source	pp	PbPb 50–100%	PbPb 30–50%	PbPb 10–30%	PbPb 0–10%
γ p_{T} threshold	3.0%	3.0%	3.0%	2.0%	1.2%
Jet p_{T} threshold	1.3%	1.3%	0.2%	0.5%	2.4%
γ efficiency	0.8%	0.8%	0.3%	0.3%	0.3%
Jet efficiency	0.6%	0.6%	0.7%	0.4%	0.3%
Isolated γ definition	0.7%	0.7%	1.6%	2.0%	0.5%
γ purity	6.8%	6.8%	2.7%	0.5%	0.9%
Electon contamination	0.5%	0.5%	0.5%	0.5%	0.5%
Fake jet contamination	0.3%	0.3%	0.1%	0.2%	1.2%
Jet ϕ resolution	0.5%	0.5%	0.5%	0.5%	0.5%
σ fitting	0.3%	0.3%	0.1%	0.1%	0.1%
Total	7.7%	7.7%	4.5%	3.0%	3.2%

Table 8.2: Relative systematic uncertainties for $\langle x_{J\gamma}\rangle$ for pp data and each of the PbPb centrality bins. The uncertainties due to the pp $\gamma-$jetrelative energy scale and γ purity are common to all of the measurements and are quoted as a correlated uncertainty.

Source	pp	PbPb 50–100%	PbPb 30–50%	PbPb 10–30%	PbPb 0–10%
$\gamma-$jetrel. energy scale	2.8%	4.1%	5.4%	5.0%	4.9%
γ p_{T} threshold	0.6%	0.6%	0.6%	0.6%	1.3%
Jet p_{T} threshold	0.7%	0.7%	1.9%	1.9%	2.0%
γ efficiency	$<0.1\%$	$<0.1\%$	$<0.1\%$	0.1%	0.2%
Jet efficiency	0.5%	0.5%	0.6%	0.6%	0.5%
Isolated γ definition	0.1%	0.1%	0.7%	0.4%	2.0%
γ purity	2.2%	2.2%	1.9%	2.4%	2.7%
Electron contamination	0.5%	0.5%	0.5%	0.5%	0.5%
Fake jet contamination	0.1%	0.1%	0.1%	0.2%	0.1%
Total	3.7%	4.8%	6.2%	6.0%	6.4%
Correlated (abs., rel.)	3.6%	3.6%	3.6%	3.6%	3.6%
Point-to-point	0.9%	3.2%	5.1%	4.8%	5.3%

Table 8.3: Relative systematic uncertainties for the fraction of photons matched with jets, $\mathsf{R}_{J\gamma}$, for pp data and each of the PbPb centrality bins.

Source	pp	PbPb 50–100%	PbPb 30–50%	PbPb 10–30%	PbPb 0–10%
γ p_{T} threshold	2.0%	2.0%	1.9%	1.3%	2.1%
Jet p_{T} threshold	1.4%	1.4%	2.3%	2.6%	2.7%
γ efficiency	0.2%	0.2%	0.2%	0.5%	0.5%
Jet efficiency	1.5%	1.5%	1.7%	1.8%	2.1%
Isolated γ definition	0.2%	0.2%	0.6%	1.3%	0.8%
γ purity	2.3%	2.3%	1.9%	0.2%	0.9%
Electron contamination	0.5%	0.5%	0.5%	0.5%	0.5%
Fake jet contamination	0.4%	0.4%	0.8%	1.0%	1.4%
Total	3.7%	3.7%	4.1%	3.9%	4.5%

8.3 Discussion

This thesis was motivated by this question "How does a high energy quark interacts with hot and dense medium?". Based on the observations in Sec. 8.2, it is clear that the jet produced inside medium is remarkably different from that in vacuum. Can we extract more hints about the dynamics which underlies this phenomenon?

From the preservation of $\Delta\phi_{J\gamma}$ distribution (Fig. 8.7 , 8.9), we can infer that the energy loss is made by radiation of multiple soft gluons rather than by a few hard radiation. If the latter were true, the direction of jet axis must have been fluctuated and manifest in the remarkable erosion of back-to-back polarity of $\gamma-$jet pairs.

One of the analogy can be made by a speedy baseball thrown into a room which is full of small styrofoam beads. The baseball will undergo a series of soft collisions with hundreds of beads and lose its energy gradually. In this case, the final direction will not be notably distracted from the initial direction. Another example is that a fast bullet shot in water is stopped by the friction without changing orientation.

Now, image that we replaced the styrofoam balls by (hard) golf balls. We can reduce the density of balls to tune the final energy loss of traversing baseball to be same with the previous experiment with styrofoam ball. The number of interactions is now only a few. Each collision will make a huge disturbance and the baseball will be scattered by larger angle. Observation from the $\Delta\phi_{J\gamma}$ results in Fig. 8.9 is closer to the case of baseball in the styrofoam bid pool rather than in the golf ball pool.

Then, how big was the energy loss? Fig. 8.12 says that the average energy loss of a jet is 14% of the partner photon energy (0-10% central events). But, this is not the end of story because the mean value was evaluated by jets above the reconstruction threshold which is $p_{\mathrm{T}} > 30$ GeV/c. The jets in the central heavy ion events have been slowed down below 30GeV/c for 17% more events compared to pp collisions (Fig 8.10). So, if we count those missing jets, the $<x_{J\gamma}>$ will be even lowered. We can calculate the lower limit of this value by setting the p_{T} of missing jets as 30GeV/c.

The average p_{T} of the selected photons in PbPb events was 75GeV/c and this can be thought of as the energy of the recoiled quark at the initial state. Also, we can reasonably assume that the photon spectrum is consistent for pp and PbPb collisions. In pp, $<x_{J\gamma}>$ was 0.84, therefore the average jet energy is 75GeV $\times$ 0.84 $=$ 63GeV. In 0-10% central PbPb collisions, $<x_{J\gamma}>$ was 0.73, so the average jet energy is 75GeV $\times$ 0.73 $=$ 55GeV. But its $R_{J\gamma}$ was 0.49 which is 0.17 smaller than that of pp. So, the average energy of jets including the missing 17% is

$$< p_T^{Jet} > \; < \; \frac{(55\text{GeV/c} \times 0.49) + (30\text{GeV/c} \times 0.17)}{0.66} = 48\text{GeV/c} \tag{8.4}$$

Hence, the average energy loss of jets was 63 - 48 = 15GeV/c. This is 20% of the initial energy of the quark.

Then, how strong was the stopping force? If we assume the traversing distance is 5.5 fm which is the radius of lead ion, the average force is 2.7 GeV/fm. In SI unit, it is 500,000 newton which is 3 times of the confinement force between quarks predicted in the Cornell-potential.

8.4 Toy Model Study

Simple toy models were used to quantitatively examine the jet quenching observed in the experiments. The simulation takes the momenta of $\gamma-$jet pairs in pp data which was taken in 2013 pp run at 2.76TeV. The integrated luminosity is 5fb^{-1} so we have enough statistics for this study. Energy of jets are deducted by the amount designed in the jet quenching model, and then the physics observables such as $R_{J\gamma}$ and $x_{J\gamma}$ were calculated. These *artificially* quenched pp results were compared to PbPb data in order to get quantitative and qualitative hints for understanding jet quenching phenomena.

8.4.1 Perturbative QCD Inspired Model

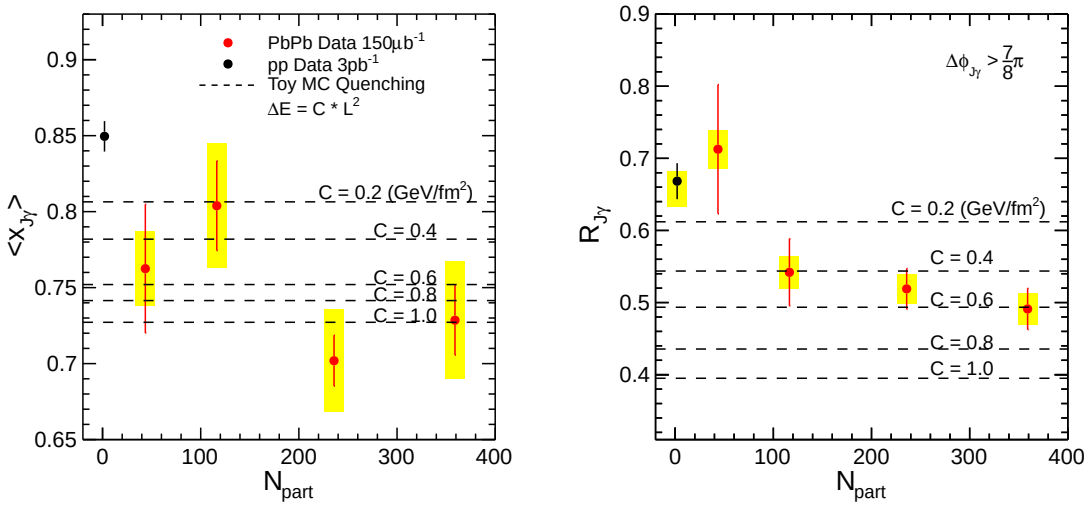

Figure 8.13: $<x_{J\gamma}>$ (Left) and $R_{J\gamma}$ (Right) of the toy MC simulation with various choice of parameter C were expressed as dashed lines. The PbPb data points are same to those in Fig. 8.10 and Fig. 8.12. The pp data were obtained from 2013 pp run at 2.76TeV. The $<x_{J\gamma}>$ values in toy model agree with 0-10% PbPb data when C is 0.6, 0.8 or 1.0 GeV/fm^{-2} . However, C is strictly constrained to be around 0.6 GeV/fm^{-2} in order to make $R_{J\gamma}$ in the model consistent with 0-10% collision data.

Perturbative QCD calculation predicts that the energy loss of a high p_{T} quark scales by square of the propagation length in homogeneous medium. (Sec. 2.2).

$$\Delta \mathrm{E} \simeq C \times \mathrm{L}^2 \tag{8.5}$$

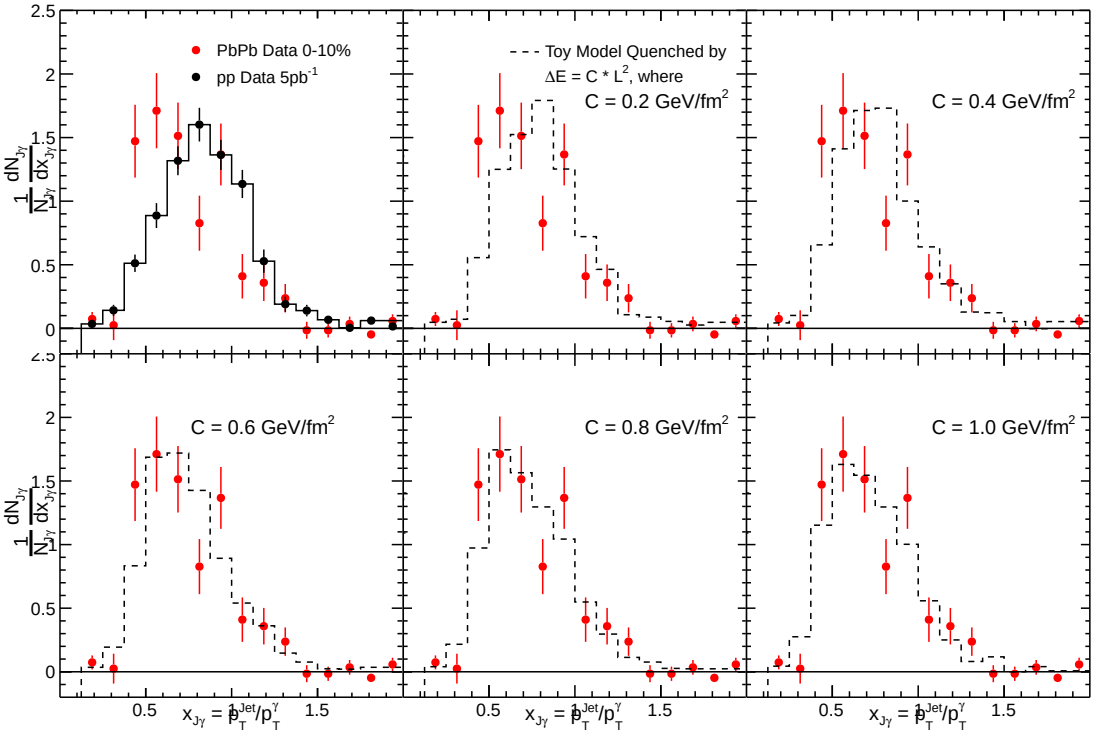

Figure 8.14: Distribution of $x_{J\gamma}$ when the pp data was artificially quenched by toy MC test.The PbPb data in this plot is same to that in Fig 8.11 Data and model agree well for C's betwwen 0.6 and 1.

, where C is a constant determined by the thermodynamic variables of the medium. In our toy model, we will treat this as a parameter. In order to determine the path lengths of quarks, a crude shape of QGP was created on top of following assumptions.

1. Pb nuclei is a perfect sphere with radius of 5.5fm in its rest frame. It is composed of uniformly distributed protons and neutrons.

2. The QGP produced by the collision is a tube whose transverse shape is the overlapping plane of two colliding lead nuclei. Therefore, the head-on collisions will make a cylinder shape of QGP with the same radius of the lead nuclei.

3. The probability of producing $\gamma-$jet scattering at a certain location on the transverse plane is proportional to the multiplication of local thickness of two lead nuclei.

4. The expansion in the transverse direction is ignored. In other words, the path length of a quark is determined by the location of production and direction of momentum.

5. The temperature of the medium is uniform and do not change while jets passes though.

Various values for the constant C in Eq. 8.5 have been tested in the range [0, 1 GeV/fm^2]. The results of modified $R_{J\gamma}$ and $<x_{J\gamma}>$ are summarized in Fig 8.13. The $<x_{J\gamma}>$ values in toy model agrees with 0-10% PbPb data when C is between 0.6 and 1.0 GeV/fm^{-2} . However, in order to make $R_{J\gamma}$ in the model consistent with 0-10% data, C must be strictly constrained at 0.6 GeV/fm^{-2}

In Fig. 8.14, the distributions of $x_{J\gamma}$ were also compared with the 0-10$ PbPb data. The real PbPb data and toy MC are consistent within uncertainty when C is between 0.8 and 1 GeV/fm^{-2} .

The results indicate that this toy MC was too naive to provide a comprehensive picture of jet quenching. But, roughly we can constrain C to be between 0.6fm^{-2} and 0.8fm^{-2} , if the energy loss scales by square of path length.

8.4.2 Constant Energy Loss Model

The second toy model is *constant energy loss model* in which jets lose constant amount energy regardless of path length. Although this is a fairly unrealistic picture for jet

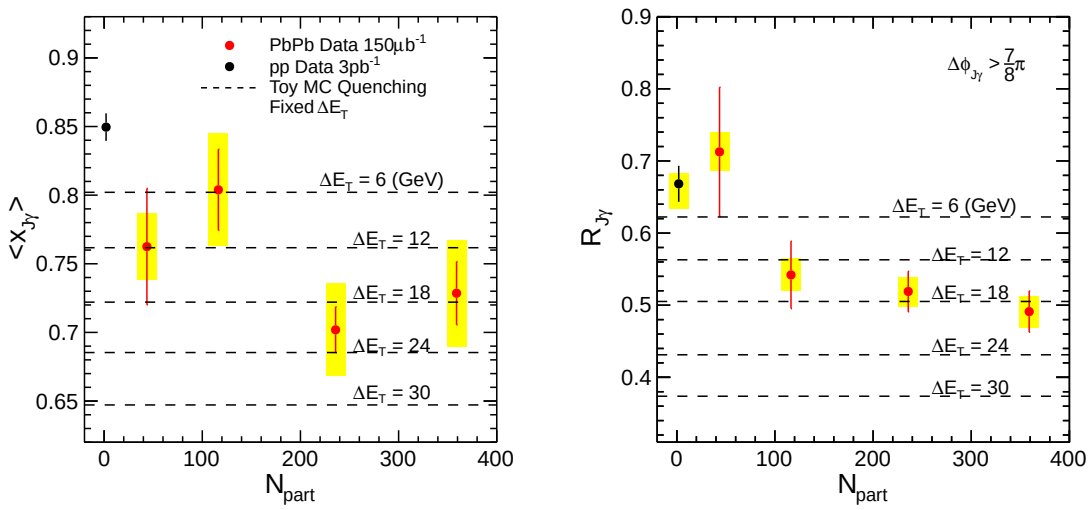

Figure 8.15: $<x_{J\gamma}>$ (Left) and $R_{J\gamma}$ (Right) of the toy MC simulation of *constant energy loss model* were expressed as dashed lines. The PbPb data points are same to those in Fig. 8.10 and Fig. 8.12. $<x_{J\gamma}>$ and $x_{J\gamma}$ values in toy model agree well with 0-10% PbPb data when ΔE_T is 18GeV.

quenching phenomena, it was tried to examine the calculation in Eq. 8.4 which gave us $<\Delta E_T> = 16$GeV.

Various ΔE_T values from 6 to 30 GeV were tested. The modified $R_{J\gamma}$ and $<x_{J\gamma}>$ can be found in Fig 8.15. The both values in toy model agree with 0-10% PbPb data when ΔE_T is 18GeV. In Fig. 8.16, the distributions of $x_{J\gamma}$ of this model were also compared with the 0-10$ PbPb data. The real PbPb data and toy MC agree well when when ΔE_T is 18GeV again.

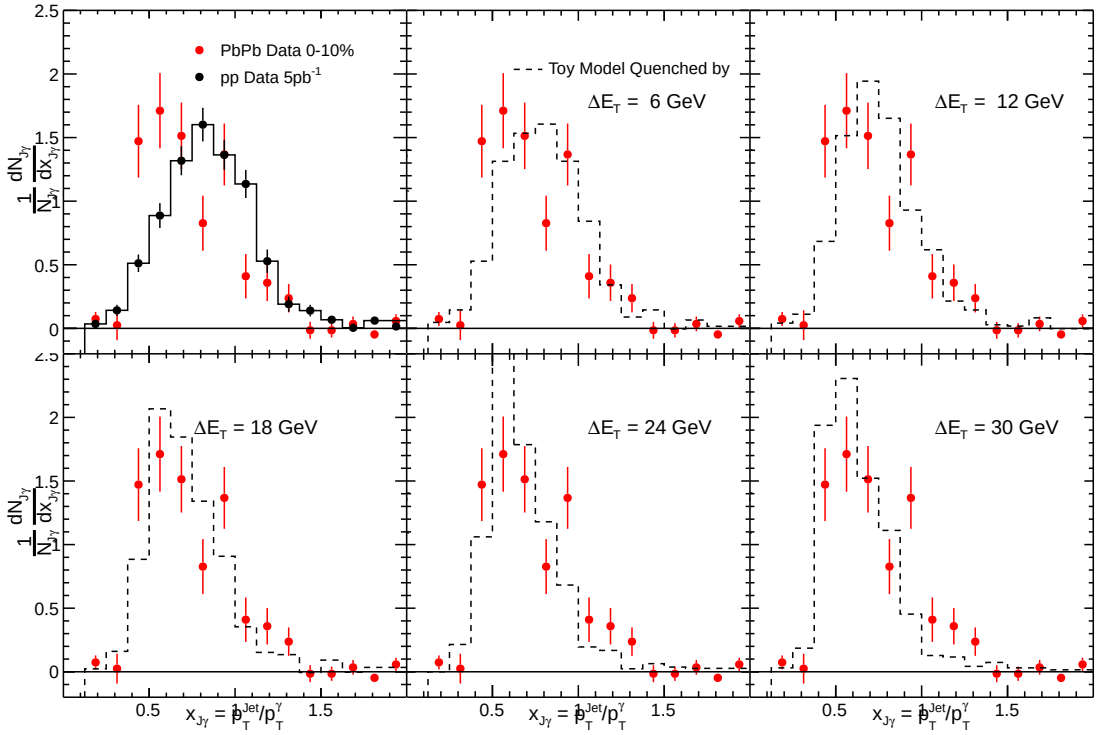

Figure 8.16: Distribution of $x_{J\gamma}$ when the pp data was artificially quenched by *constant energy loss model*. The PbPb data in this plot is same to that in Fig 8.11. The data and models agree well when ΔE_T is between 12GeV and 18GeV.

9 Conclusion

The study of this dissertation was inspired by the interest in the strong interaction in extremely hot and dense medium, Quark Gluon Plasma. The $\gamma-$jet scattering produced inside the medium by the heavy ion collision was used as the probe to investigate this mysterious QCD matter. Being color neutral, photons (γ) pass though the medium without any strong interaction and delivered the information of initial state of the $\gamma-$jet production. And, the jets recoiled by photons in the opposite direction provided the final energy of the quarks after the medium-induced energy loss by the QGP. The main discovery of this analysis was that a high energy quark loses significant amount of energy by unusually powerful stopping force by the medium. In addition, we were able to infer that the interaction was made by the radiation of multiple soft gluons based on the observation that angular correlation between a photon and the partner jet is preserved.

The lessons from this analysis provide quantitative hint for the comprehensive understanding of the jet quenching phenomenon and general QCD in finite temperature. At the same time, the results open more curiosities. Where did the lost energy move? How has the virtuality of energy-lost quark been changed? Would the similar effects also happen for the dense and cold medium? Can we pin down the amount of energy loss more accurately? These questions may be answered by follow-up analyses in the heavy ion program at LHC, such as the modification of the jet fragmentation function, photon-hadron correlation, momentum dependence of the $\gamma-$jet correlation and the jet energy loss in proton-nucleus experiments.

Bibliography

[1] Edward V. Shuryak. Quantum chromodynamics and the theory of superdense matter. *Physics Reports*, 61(2):71 – 158, 1980.

[2] Helmut Satz. The SPS heavy ion programme. *Phys.Rept.*, 403-404:33–50, 2004.

[3] Brookhaven National Laboratory. AGS Dept. *AGS Experiments ...* AGS Department, Experimental Planning and Support Division, Brookhaven National Laboratory, Brookhaven Science Associates, 1999.

[4] B.B. Back et al. The phobos perspective on discoveries at rhic. *Nuclear Physics A*, 757(1âĂŞ2):28 – 101, 2005.

[5] K. Adcox et al. Formation of dense partonic matter in relativistic nucleusâĂŞnucleus collisions at rhic: Experimental evaluation by the phenix collaboration. *Nuclear Physics A*, 757(1âĂŞ2):184 – 283, 2005.

[6] J. Adams et al. Experimental and theoretical challenges in the search for the quarkâĂŞgluon plasma: The star collaboration's critical assessment of the evidence from rhic collisions. *Nuclear Physics A*, 757(1âĂŞ2):102 – 183, 2005.

[7] I. Arsene et al. QuarkâĂŞgluon plasma and color glass condensate at rhic? the perspective from the brahms experiment. *Nuclear Physics A*, 757(1âĂŞ2):1 – 27, 2005.

[8] H. Geiger and E. Marsden. On a Diffuse Reflection of the α -Particles. *Royal Society of London Proceedings Series A*, 82:495–500, July 1909.

[9] E. Rutherford. Lxxix. the scattering of Îś and Îš particles by matter and the structure of the atom. *Philosophical Magazine Series 6*, 21(125):669–688, 1911.

[10] E. D. Bloom, D. H. Coward, H. Destaebler, J. Drees, G. Miller, L. W. Mo, R. E. Taylor, M. Breidenbach, J. I. Friedman, G. C. Hartmann, and H. W. Kendall. High-Energy

Inelastic e-p Scattering at 6deg and 10deg. *Physical Review Letters*, 23:930–934, October 1969.

[11] M. Gyulassy and M. Plumer. Jet quenching in lepton nucleus scattering. *Nucl.Phys.*, B346:1–16, 1990.

[12] Xin-Nian Wang and Miklos Gyulassy. Gluon shadowing and jet quenching in A + A collisions at s**(1/2) = 200-GeV. *Phys.Rev.Lett.*, 68:1480–1483, 1992.

[13] Xin-Nian Wang, Miklos Gyulassy, and Michael Plumer. The LPM effect in QCD and radiative energy loss in a quark gluon plasma. *Phys.Rev.*, D51:3436–3446, 1995.

[14] C. Adler et al. Disappearance of back-to-back high p_T hadron correlations in central Au+Au collisions at $\sqrt{s_{NN}} = 200$-GeV. *Phys.Rev.Lett.*, 90:082302, 2003.

[15] C. N. Yang and R. L. Mills. Conservation of isotopic spin and isotopic gauge invariance. *Phys. Rev.*, 96:191–195, Oct 1954.

[16] M. E. Peskin and D. V. Schroeder. *An Introduction to Quantum Field Theory*. Addison-Wesley Pub. Co., Reading, Massachusetts, USA, 1995.

[17] David J. Gross and Frank Wilczek. Ultraviolet behavior of non-abelian gauge theories. *Phys. Rev. Lett.*, 30:1343–1346, Jun 1973.

[18] Larry McLerran. The Phase Diagram of QCD and Some Issues of Large N(c). *Nucl.Phys.Proc.Suppl.*, 195:275–280, 2009.

[19] Frithjof Karsch. News from lattice QCD on heavy quark potentials and spectral functions of heavy quark states. *J.Phys.*, G30:S887–S894, 2004.

[20] A. Abulencia et al. Measurement of the inclusive jet cross section in $p\bar{p}$ interactions at $\sqrt{s} = 1.96$-TeV using a cone-based j*et al*gorithm. *Phys.Rev.*, D74:071103, 2006.

[21] Matteo Cacciari, Gavin P. Salam, and Gregory Soyez. The Anti-k(t) jet clustering algorithm. *JHEP*, 0804:063, 2008.

[22] J.E. Huth *et al.* Research Directions for the Decade, Proceedings of the Summer Study on High Energy Physics. Snowmass, Colorado, 1990, p. 134.

[23] R. Baier, Yuri L. Dokshitzer, Alfred H. Mueller, S. Peigne, and D. Schiff. Radiative energy loss of high-energy quarks and gluons in a finite volume quark - gluon plasma. *Nucl.Phys.*, B483:291–320, 1997.

[24] R. Baier, Yuri L. Dokshitzer, Alfred H. Mueller, S. Peigne, and D. Schiff. Radiative energy loss and p(T) broadening of high-energy partons in nuclei. *Nucl.Phys.*, B484:265–282, 1997.

[25] B.G. Zakharov. Radiative energy loss of high-energy quarks in finite size nuclear matter and quark - gluon plasma. *JETP Lett.*, 65:615–620, 1997.

[26] B.G. Zakharov. Fully quantum treatment of the Landau-Pomeranchuk-Migdal effect in QED and QCD. *JETP Lett.*, 63:952–957, 1996.

[27] Miklos Gyulassy and Xin-nian Wang. Multiple collisions and induced gluon Bremsstrahlung in QCD. *Nucl.Phys.*, B420:583–614, 1994.

[28] S.-J. Sin and I. Zahed. Holography of radiation and jet quenching. *Physics Letters B*, 608:265–273, February 2005.

[29] H. Liu, K. Rajagopal, and U. A. Wiedemann. Calculating the Jet Quenching Parameter. *Physical Review Letters*, 97(18):182301, November 2006.

[30] Edmond Iancu. QCD in heavy ion collisions. 2012.

[31] Konrad Tywoniuk. Advancing QCD-based calculations of energy loss. 2012.

[32] Abhijit Majumder. Calculating the Jet Quenching Parameter $\hat{q}$ in Lattice Gauge Theory. 2012.

[33] F. Abe et al. A Prompt photon cross-section measurement in $\bar{p}p$ collisions at $\sqrt{s} =$ 1.8 TeV. *Phys.Rev.*, D48:2998–3025, 1993.

[34] F. Abe et al. Measurement of the isolated prompt photon cross-sections in $\bar{p}p$ collisions at $\sqrt{s} = 1.8$ TeV. *Phys.Rev.Lett.*, 68:2734–2738, 1992.

[35] F. Abe et al. A Precision measurement of the prompt photon cross-section in $p\bar{p}$ collisions at $\sqrt{s} = 1.8$ TeV. *Phys.Rev.Lett.*, 73:2662–2666, 1994.

[36] H. Baer, J. Ohnemus, and J.F. Owens. A NEXT-TO-LEADING LOGARITHM CALCULATION OF DIRECT PHOTON PRODUCTION. *Phys.Rev.*, D42:61–71, 1990.

[37] Stefano Catani, Michel Fontannaz, Jean-Philippe Guillet, and Eric Pilon. Cross section of isolated prompt photons in hadron-hadron collisions. *Journal of High Energy Physics*, 2002(05):028, 2002.

[38] David d'Enterria and Juan Rojo. Quantitative constraints on the gluon distribution function in the proton from collider isolated-photon data. *Nucl.Phys.*, B860:311–338, 2012.

[39] L.W. Whitlow, Stephen Rock, A. Bodek, E.M. Riordan, and S. Dasu. A Precise extraction of R = sigma-L / sigma-T from a global analysis of the SLAC deep inelastic e p and e d scattering cross-sections. *Phys.Lett.*, B250:193–198, 1990.

[40] M. Derrick et al. Measurement of the proton structure function F2 in e p scattering at HERA. *Phys.Lett.*, B316:412–426, 1993.

[41] Vardan Khachatryan et al. Measurement of the Isolated Prompt Photon Production Cross Section in pp Collisions at $\sqrt{s} = 7$ TeV. *Phys.Rev.Lett.*, 106:082001, 2011.

[42] F. Arleo, K. J. Eskola, H. Paukkunen, and C. A. Salgado. Inclusive prompt photon production in nuclear collisions at RHIC and LHC. *Journal of High Energy Physics*, 4:55, April 2011.

[43] K. J. Eskola, H. Paukkunen, and C. A. Salgado. EPS09 − A new generation of NLO and LO nuclear parton distribution functions. *Journal of High Energy Physics*, 4:65, April 2009.

[44] M. Hirai, S. Kumano, and T.-H. Nagai. Determination of nuclear parton distribution functions and their uncertainties at next-to-leading order. *PRC*, 76(6):065207, December 2007.

[45] D. de Florian and R. Sassot. Nuclear parton distributions at next to leading order. *PRD*, 69(7):074028, April 2004.

[46] Serguei Chatrchyan et al. Measurement of isolated photon production in pp and PbPb collisions at $\sqrt{s_{NN}} = 2.76$ TeV. *Phys.Lett.*, B710:256–277, 2012.

[47] Yong-Sun Kim. Isolated photon production in $\sqrt{s_{NN}} = 2.76$ TeV PbPb collisions as a function of transverse energy and reaction centrality. *J.Phys.*, G38:124179, 2011.

[48] Michael L. Miller, Klaus Reygers, Stephen J. Sanders, and Peter Steinberg. Glauber modeling in high energy nuclear collisions. *Ann. Rev. Nucl. Part. Sci.*, 57:205, 2007.

[49] Serguei Chatrchyan et al. Study of Z boson production in PbPb collisions at nucleon-nucleon centre of mass energy = 2.76 TeV. *Phys.Rev.Lett.*, 106:212301, 2011.

[50] Serguei Chatrchyan et al. Study of W boson production in PbPb and pp collisions at $\sqrt{s_{NN}} = 2.76$ TeV. *Phys.Lett.*, B715:66–87, 2012.

[51] A. Adare et al. Medium modification of jet fragmentation in Au+Au collisions at $\sqrt{s_{NN}} = 200$ GeV measured in direct photon-hadron correlations. 2012.

[52] A.M. Hamed. Azimuthal correlations between charged hadrons and direct photons at high-p(t) in p+p and Au+Au collisions at s(NN)**(1/2) = 200-GeV. 2008.

[53] A. Adare et al. Identified charged hadron production in $p+p$ collisions at $\sqrt{s} = 200$ and 62.4 GeV. *Phys.Rev.*, C83:064903, 2011.

[54] S.S. Adler et al. Suppressed π^0 production at large transverse momentum in central Au+ Au collisions at $sqrt s_{NN} = 200$ GeV. *Phys.Rev.Lett.*, 91:072301, 2003.

[55] K. Adcox et al. Suppression of hadrons with large transverse momentum in central Au+Au collisions at $\sqrt{s_{NN}} = 130$-GeV. *Phys.Rev.Lett.*, 88:022301, 2002.

[56] B.B. Back et al. Centrality dependence of charged hadron transverse momentum spectra in Au + Au collisions from s(NN)**(1/2) = 62.4-GeV to 200-GeV. *Phys.Rev.Lett.*, 94:082304, 2005.

[57] B. Alver et al. System size and centrality dependence of charged hadron transverse momentum spectra in Au + Au and Cu + Cu collisions at s(NN)**(1/2) = 62.4-GeV and 200-GeV. *Phys.Rev.Lett.*, 96:212301, 2006.

[58] G. Agakishiev et al. Identified hadron compositions in p+p and Au+Au collisions at high transverse momenta at $\sqrt{s_{NN}} = 200$ GeV. *Phys.Rev.Lett.*, 108:072302, 2012.

[59] Serguei Chatrchyan et al. Study of high-pT charged particle suppression in PbPb compared to pp collisions at $\sqrt{s_{NN}} = 2.76$ TeV. *Eur.Phys.J.*, C72:1945, 2012.

[60] K. Aamodt et al. Suppression of Charged Particle Production at Large Transverse Momentum in Central Pb–Pb Collisions at $\sqrt{s_{NN}} = 2.76$ TeV. *Phys.Lett.*, B696:30–39, 2011.

[61] Serguei Chatrchyan et al. Observation and studies of jet quenching in PbPb collisions at nucleon-nucleon center-of-mass energy = 2.76 TeV. *Phys.Rev.*, C84:024906, 2011.

[62] Serguei Chatrchyan et al. Jet momentum dependence of jet quenching in PbPb collisions at $\sqrt{s_{NN}} = 2.76$ TeV. *Phys.Lett.*, B712:176–197, 2012.

[63] Lyndon Evans and Philip Bryant. Lhc machine. *Journal of Instrumentation*, 3(08):S08001, 2008.

[64] S. Chatrchyan et al. The CMS experiment at the CERN LHC. *JINST*, 03:S08004, 2008.

[65] V. Khachatryan, A. M. Sirunyan, A. Tumasyan, W. Adam, T. Bergauer, M. Dragicevic, J. Erö, C. Fabjan, M. Friedl, R. Frühwirth, and *et al.* CMS tracking performance results from early LHC operation. *European Physical Journal C*, 70:1165–1192, December 2010.

[66] F. Nessi Tedaldi and for the CMS Collaboration. Response evolution of the CMS ECAL and R/D studies for electromagnetic calorimetry at the High-Luminosity LHC. *ArXiv e-prints*, November 2012.

[67] CMS Collaboration. Performance of the CMS hadron calorimeter with cosmic ray muons and LHC beam data. *Journal of Instrumentation*, 5:3012, March 2010.

[68] S. Chatrchyan et al. The CMS experiment at the CERN LHC. *JINST*, 03:S08004, 2008.

[69] David A. Petyt. Anomalous apd signals in the cms electromagnetic calorimeter. *Nuclear Instruments and Methods in Physics Research Section A: Accelerators, Spectrometers, Detectors and Associated Equipment*, 695(0):293 – 295, 2012.

[70] Artur Apresyan and on behalf of the CMS Collaboration). Identification and mitigation of anomalous signals in cms hadronic calorimeter. *Journal of Physics: Conference Series*, 404(1):012044, 2012.

[71] Serguei Chatrchyan et al. Measurement of the Differential Cross Section for Isolated Prompt Photon Production in pp Collisions at 7 TeV. *Phys.Rev.*, D84:052011, 2011.

[72] Torbjorn Sjostrand, Stephen Mrenna, and Peter Skands. PYTHIA 6.4 physics and manual. *JHEP*, 05:026, 2006.

[73] I.P. Lokhtin, L.V. Malinina, S.V. Petrushanko, A.M. Snigirev, I. Arsene, et al. HYDJET++ heavy ion event generator and its applications for RHIC and LHC. 2009.

[74] S. Piperov. Geant4 validation with CMS calorimeters test-beam data. *ArXiv e-prints*, August 2008.

[75] Francois Arleo, David d'Enterria, and Andre S. Yoon. Single-inclusive production of large-pT charged particles in hadronic collisions at TeV energies and perturbative QCD predictions. *JHEP*, 1006:035, 2010.

[76] Serguei Chatrchyan et al. Dependence on pseudorapidity and centrality of charged hadron production in PbPb collisions at a nucleon-nucleon centre-of-mass energy of 2.76 TeV. *JHEP*, 1108:141, 2011.

[77] Serguei Chatrchyan et al. Centrality dependence of dihadron correlations and azimuthal anisotropy harmonics in PbPb collisions at $\sqrt{s_{NN}} = 2.76$ TeV. *Eur.Phys.J.*, C72:2012, 2012.

[78] I.P Lokhtin and *et al.* Hydjet webpage.

[79] Roger D. Woods and David S. Saxon. Diffuse surface optical model for nucleon-nuclei scattering. *Phys. Rev.*, 95:577–578, Jul 1954.

[80] W. Busza et al. Charged-particle multiplicity in p - nucleus interactions at 100 and 175 GeV/c. *Phys.Rev.Lett.*, 34:836, 1975.

[81] B. Alver et al. Phobos results on charged particle multiplicity and pseudorapidity distributions in Au+Au, Cu+Cu, d+Au, and p+p collisions at ultra-relativistic energies. *Phys.Rev.*, C83:024913, 2011.

[82] B. Alver, M. Baker, C. Loizides, and P. Steinberg. The PHOBOS Glauber Monte Carlo. 2008.

[83] Electron reconstruction and identification at sqrt(s) = 7 TeV. 2010.

[84] Commissioning of the Particle-Flow reconstruction in Minimum-Bias and Jet Events from pp Collisions at 7 TeV. 2010.

[85] Olga Kodolova, I. Vardanian, A. Nikitenko, and A. Oulianov. The performance of the jet identification and reconstruction in heavy ions collisions with CMS detector. *Eur.Phys.J.*, C50:117–123, 2007.

[86] Measuring Electron Efficiencies at CMS with Early Data. 2008.

[87] Serguei Chatrchyan et al. Dependence on pseudorapidity and centrality of charged hadron production in PbPb collisions at a nucleon-nucleon centre-of-mass energy of 2.76 TeV. *JHEP*, 1108:141, 2011.

[88] Kenneth Aamodt et al. Centrality dependence of the charged-particle multiplicity density at mid-rapidity in Pb-Pb collisions at $\sqrt{s_{NN}} = 2.76$ TeV. *Phys.Rev.Lett.*, 106:032301, 2011.

[89] Zi-Wei Lin, Che Ming Ko, Bao-An Li, Bin Zhang, and Subrata Pal. A multi-phase transport model for relativistic heavy ion collisions. *Phys. Rev.*, C72:064901, 2005.

10 Acknowledgments

This dissertation would not have been possible without the guidance and the help of several individuals who contributed and extended their valuable assistance in the preparation and completion of this study.

First and foremost, I would like to express my deepest gratitude to my advisor, Professor Wit Busza for sincerity and encouragement that I will never forget in my life. Wit has been the best inspiration as I hurdle all the obstacles in the completion of this work. When I first arrived to MIT, I once worked in a biophysics group and shortly later I lost my interest and left the field. I knocked doors of many professors in physics department and asked for counselling about what I have to work on. Among them, it was Wit who first arose my curiosity about the Quark Gluon Plasma and finally convinced me to join the heavy ion group and CMS collaboration. Not only was he a good thesis advisor but the most importantly he became a great mentor by sharing his deep wisdoms that I learned by my heart. He always urged me to regularly go to the library to THINK and REFLECT on physics rather than to become a computer coding machine. He also emphasized that the success in research necessitates a strong body and mind, which turned out to be absolutely true. For his cordial encouragement and valuable discussions, meetings with him brought great happiness to my life in Geneva. Personally, it is my great honor to be his last PhD student as he is being retired from MIT after his admirable career.

I was also very lucky to work with two great physicists, Professor Gunther Roland and Professor Bolek Wyslouch. As the leader of MIT heavy ion group for the last 3 years, Gunther taught me enormous knowledges of heavy ion physics and many practical lessons about how to tackle complicated problems. By watching his untiring driving force, I learned that the enthusiasm and hard working are always rewarded. Bolek gave me precious lessons about the attitude for being a good researcher in an experimental physics collaboration which enabled my settlement in the CMS group. Also, he played an amazing leadership for the first heavy ion data taking at LHC, which became the main ingredients of this dissertation.

I also would like to thank to very talented post-doctoral fellows and research scientists at MIT, George Stephans, Christof Roland, Wei Li, Edward Wenger, Ivan Cali, Constantin Loizides, Yue Shi Lai and Victoria Zhukova for their unsparing helps.

I had the great privilege of having the opportunity to work with my senior fellow students, Yen-Jie Lee, Andre Yoon, Frank Ma and Yetkin Yilmaz. They were my colleagues as well as great friends who spent amazing time in Geneva with me. Yen-Jie handed over his broad knowledge and various computing techniques to me. His passion toward research was always impressive and helped me to keep my initial motivation. Andre, who was my senior at University of Illinois at Urbana Champaign as well, thankfully became an attentive mentor in all aspects. Yetkin also gave me tons of lessons in my research. He also helped me to have fun time in Geneva by inviting me to many non-CERN places in Geneva, including a Tango class. Frank was my fantastic analysis partner and worked on many projects together. We not only shared useful knowledges but had spiritual discussion about how we have to make our lives more spiritual as Christians. In particular, I will never forget the discussion that we had while walking along the tram track on a snowy night of January in 2010.

It was my big pleasure to study with younger fellows, Dragos Velicanu, Doga Gulhan, Alex Barbieri, Aleksey Strelnikov and Mukund Varma for making my life after coming back from CERN more joyful. The weekly physics journal club (The Wit's lunch) with these guys was always exciting. In the end, I would like to thank to Anna Maria Convertino, our secretary, for organizing all the administrative works for the group.

Plus, I would like extend thanks to my colleagues in the CMS collaboration including Shin-Shan Eiko Yu, Yun-Ju Lu, Chia-Ming Kuo and Rong-Shyang Lu. Their expertise on photon reconstruction enormously helped my analysis.

I would like to express my special thanks to my Korean colleagues at CERN, Prof. Kwang-Souk Sim, Prof. Byungsik Hong, Prof. Inkyu Park, Prof. In-Kwon Yoo, Prof. Sangyong Jeon, Dongho Moon, Ji Hyun Kim, Hyunchul Kim, JunGyu Yi, Mihee Jo, Minjung Kweon and Woojin Park. In particular, the frequent lunch with Dongho, Ji Hyun, Hyunchul, JunGyu and Mihee at the CERN Restaurant 1 always recharged my batteries.

My life in Boston would have been very boring without many awesome friends I met here, Donghyun Kim, Seung Ki Kwak, Jaehoon Lee, Jee Woo Park, Changmin Lee, Junghyun Lee, Junho Kang, who provided me helps and made living here great fun.

Finally, I owe everything to my beloved family. I can not imagine to make any work at MIT without the education, supports and love of my parents, Kapseok Kim and Sungim Kim. Also, I would like to appreciate the infinite mental aids from my brother Yongil

Kim.